Semiconductor nanowire based coherent light sources: Temporal dynamics and tunability

Dissertation

zur Erlangung des akademischen Grades
doctor rerum naturalium (Dr. rer. nat.)

vorgelegt dem Rat der Physikalisch-Astronomischen Fakultät der
Friedrich-Schiller-Universität Jena

von M.Sc. Robert Röder
geboren am 03.10.1986 in Zeitz

1. Gutachter: Prof. Dr. Carsten Ronning, Friedrich-Schiller-Universität Jena

2. Gutachter: Prof. Dr. Martin Eickhoff, Justus-Liebig-Universität Gießen

3. Gutachter: Prof. Dr. Anna Fontcuberta i Morral, EPFL Lausanne

Tag der Abgabe: 01.06.2016

Tag der Disputation: 19.09.2016

Zeitliche Dynamik und Modifizierung von Nanodraht basierten kohärenten Lichtquellen

Der technologische Fortschritt der vergangenen $50 - 60$ Jahre war wesentlich geprägt von den Entwicklungen in der Halbleiterelektronik und Optoelektronik. Exemplarisch dafür steht die fortschreitende Miniaturisierung der Transistoren in integrierten Schaltkreisen. Diese Entwicklungsgeschwindigkeit in der Halbleitertechnologie beizubehalten ist eine der großen Herausforderungen des nächsten Jahrzehnts. Daher werden neben dem bekannten Konzept der fortschreitenden Miniaturisierung dringend neue, alternative Ansätze benötigt. Hier könnte Halbleiter-Nanodrähten eine Schlüsselrolle zukommen, da sie funktionale, elektronische und optische Eigenschaften auf nanoskaligen Dimensionen verbinden und mit hoher Kristallqualität günstig hergestellt werden können.
Halbleiter-Nanodrähte zeigen exzellente optische Eigenschaften, wie effiziente Wellenleitung bei einem Durchmesser unterhalb der Wellenlänge des geführten Lichts sowie lokale Lichtemission. Darüber hinaus ermöglicht die Lichtverstärkung im Halbleitermaterial in Kombination mit der Morphologie eines optischen Resonators intensive Laseremission von einzelnen Nanodrähten. Somit können diese Nanodrähte zukünftig als effiziente, nanoskalige kohärente Lichtquellen eingesetzt werden.
Optisch stimulierte Laseremission von Nanodrähten konnte bereits für viele Halbleitermaterialien im Spektralbereich von UV bis NIR nachgewiesen werden. Allerdings war stets eine gepulste Anregungsquelle notwendig, da das Halbleitermaterial sonst durch den enormen, kontinuierlichen Wärmeeintrag zerstört wird. Diese Herausforderung wird bewältigt, indem Halbleiter-Nanodrähte mit einer herausragenden optischen Verstärkung und exzellenter Resonatorstruktur verwendet werden. CdS-Nanodrähte erfüllen diese Anforderungen und werden mittels Gasphasenabscheidung unter Verwendung von Zinn als Katalysator synthetisiert. Da Zinn bei der Synthese in das Kristallgitter der CdS-Nanodrähte eingebaut wird, entsteht durch die Dotierung eine hohe Dichte flacher Störstellen, die durch optische Spektroskopie nachgewiesen werden können. Unter hohen, kontinuierlichen Pumpleistungen und bei Temperaturen unterhalb von $\sim 120\,\mathrm{K}$ zeigen diese CdS:Sn-Nanodrähte (und undotierte CdS-Nanodrähte) den Übergang von spontaner zu Laseremission. Die hohe optische Verstärkung, die für die kontinuierliche Laseremission einzelner Nanodrähte notwendig ist, wird in einem Elektron-Loch-Plasma erzeugt.
Das vollständige technologische Potential von Nanodrahtlasern kann nur dann ausgenutzt werden, wenn die grundlegenden zeitlichen Dynamiken des Laserprozesses verstanden sind. Die entsprechenden Zeitskalen für Anschaltzeit und Pulsdauer liegen zwischen einigen hundert Femtosekunden und wenigen Picosekunden und werden mit einer neu entwickelten 'Doppel-Pump'-Technik sogar für einzelne Nanodrahtlaser gemessen. Sobald ein Halbleiter-Nanodraht mit einem kurzen Pumppuls angeregt wird, emittiert er bereits wenige ($\ll 10$) Picosekunden danach intensives Laserlicht. Die exakte Zeitspanne (Anschaltzeit) ist dabei abhängig vom Halbleitermaterial und der Pumpenergie. Je stärker die optisch stimulierten Ladungsträger mit den Gitterschwingungen im Nanodrahtmaterial wechselwirken, desto schneller emittiert der Nanodrahtlaser nach der Photoanregung. Daher zeigen ZnO-Nanodrahtlaser wohl die kürzesten Anschaltzeiten von etwa $1\,\mathrm{ps}$ bei einer Pumpenergie von $\sim 3.49\,\mathrm{eV}$.
Dünne ZnO-Nanodrahtlaser mit einem Durchmesser unterhalb von $\sim 200\,\mathrm{nm}$ emittieren sehr kurze Laserpulse von $\sim 5\,\mathrm{ps}$. Diese Pulsdauer lässt sich allerdings durch den Purcell-Effekt signifikant verkürzen bis in den Sub-Picosekunden-Bereich, wenn das Lichtfeld im ZnO-Nanodrahtlaser mit dem Oberflächenplasmon eines Silberfilms wechselwirkt.

ZnO-Nanodrähte sind ein hervorragendes Modellsystem um in Halbleiter-Nanodrahtlasern den Zusammenhang von Transversalmoden mit den Emissionseigenschaften und der zeitlichen Dynamik zu studieren. Dünne Halbleiter-Nanodrähte mit Durchmessern unterhalb der Schwelle zur multimodalen Wellenleitung zeigen eindeutig Laseremission der fundamentalen Transversalmode mit kurzen Pulsdauern (von $\sim 5\,\mathrm{ps}$ für ZnO-Nanodrähte). Im Gegensatz dazu zeigen dicke Halbleiter-Nanodrähte oberhalb dieser Durchmesserschwelle multimodale Laseroszillationen (bezogen auf die Transversalmoden) und eine verlangsamte zeitliche Dynamik mit deutlich längeren Laserpulsen.

Contents

1 Introduction

Semiconductor electronics and optoelectronics contributed tremendously to the technological progress in the last $50 - 60$ years. One well known example is the semiconductor learning curve that demonstrates the doubling of the number of transistors as digital switches per chip about every two years. This special case is referred to as Moore's Law [1], but it forms just a temporal section of the generalized learning curve of "costs per switch versus total accumulated volume of switches" [2], that started already when mechanical switches were replaced by vacuum tubes and thus before the era of electronic integrated circuits. Extending this learning curve into the future therefore requires both the optimization of the predominant technology combined with a seeking for fundamentally new operation principles. The principles of such a combination can be generalized to most of the technological relevant learning curves. The current "International Technology Roadmap for Semiconductors - ITRS 2.0" follows exactly this approach by combining the schemes "More Moore" and "More-than-Moore". The first one aims for a continued shrinking of the physical dimensions in order to reduce cost and increase performance, while the second scheme wants to incorporate (non-digital) functionalities into devices and systems providing additional value in different ways [3]. Thus, the "More-than-Moore" scheme considers also (nano)photonic components to play a key role either as optical interconnects or integrated as lasers, waveguides and photodetectors into a system on a chip (SoC). Such an SoC might obviously benefit from optical devices/coherent light sources with a small or even nanoscaled footprint available by low cost fabrication methods.
After the demonstration of the first laser [4], the use of lasers has been extended into many ares of scientific, industrial and public life such as spectroscopy, material modification/analysis, optics, medicine etc. [5]. Besides these innovations, there has always been the interest in the miniaturization of laser devices [6]. The successive miniaturization contributed to technologies like optical fiber communication and recently led to vertical cavity surface emitting lasers (VCSEL) [7], microdisk [8] and photonic crystal lasers [9]. However, research in the past decade focused on exploring and developing even smaller nanoscaled coherent light sources that can be integrated in SoCs, as envisaged by "More-than-Moore". Here, semiconductor nanowire based lasers are one of the investigated model systems, as they provide a small footprint and can be synthesized cheaply. The scope of this thesis is thus the investigation of individual semiconductor nanowires (NWs) as potential nanoscaled coherent light sources.
The NW morphology can be approximated as a cylinder with arbitrary footprint shape and cross sectional dimensions in the range of $1 \ldots 1000$ nm, while NW lengths usually vary between few micrometer and hundreds of micrometers. Nanowires are fabricated either top-down by several processing steps from the bulk or self-organized by bottom-up synthesis starting from atomic species. A good control over the final NW morphology and the arrangement of NW arrays can be achieved by both approaches. However, us-

ing the bottom-up approach nanostructures can be grown by low material consumption with high structural and optical quality on different kinds of substrates, including silicon and flexible substrates. Due to their high aspect ratio, NWs are well suited in order to apply electrical contacts and drive currents through them raising their potential for integrated electronic components such as NW field-effect transistors (FET) or NW based gas/bio/chemical sensors [10, 11]. Furthermore, optoelectronic (nano)devices based on NW arrays or individual NWs have been demonstrated in the past years: e.g. NW based solar cells benefit from an optimized morphology leading to enhanced absorption by light management [12, 13], while NW LEDs and photodetectors can already be integrated in photonic platforms [14]. These diverse functionalities of NW based devices offer large potential in the scope of "More-than-Moore".

In addition to these recent achievements, semiconductor NWs offer exceptional optical properties related to their morphology and the material used. Thus, a new field of research/science has developed over the past decade referred to as "nanowire photonics", investigating light emission, propagation, detection, modulation and amplification in NWs [15]. Consequently, diverse macroscopically well known optical applications/concepts such as high harmonic generation [16], optical switches [17], optical correlators [18], beam splitters [19], efficient waveguides [20] etc. were already brought to the nanoscale using NWs, to name but a few. An important part of "nanowire photonics" concentrates on investigating and developing nanoscaled semiconductor lasers as one of the smallest coherent light sources available for various on-chip applications [6]. Semiconductor NWs inherently provide all basic components of a laser system. The semiconductor material itself acts as active gain medium under optical (and possibly electrical) carrier injection. Additionally, the large difference of the refractive indices at the NW end facets causes an effective reflectivity for the light that is generated within the semiconductor. The light can therefore bounce back and forth as in a resonator. Individual semiconductor NWs act therefore as both optical gain medium and optical cavity enabling NW lasing.

The period of semiconductor NW laser research started 15 years ago unfortunately with some arguable publications on the observation of NW lasing. The following $5 - 10$ years consequently aimed for consistent proofs of lasing in NW structures and finding suitable NW materials for room temperature lasers, which cover nowadays a huge spectral range from the UV down to the N/MIR depending on the gain material band gap [21–24]. In addition, the fundamental lower size limitations for photonic NW lasers were investigated [22,23] and first steps were taken towards the modification/optimization of the NW laser devices. Typical modification methods rely mostly on the variation of material compositions in order to tune the emission wavelength [25,26] or on certain treatments of the NW cavity for an efficient adjustment of the longitudinal resonator modes [27–29]. Furthermore, it was possible to modify the field distribution within the NW by placing them in the vicinity of metallic surfaces or particles [30–32]. Although important fundamentals of NW lasers such as emission wavelength, polarization properties [33] and resonator mod-

ifications have been studied thoroughly within the past decade, further underlying physics remain relatively unstudied. This currently hinders a successful and efficient integration of NW lasers into real world applications. Thus, three key challenges were figured out and addressed within the scope of this thesis in order to push the technological relevance of nanoscaled coherent light sources:

(i) Laser oscillations in semiconductor NWs have only been achieved in a pulsed operation mode so far, as the optical carrier injection requires high pump intensities introducing a lot of heat to the NW device. This thermal budget has to dissipate during sufficiently long off times in order to avoid a heat induced material degradation. A significant performance increase could be achieved by establishing a **continuous wave (cw) emission mode for NW lasers**. This challenge requires an identification and investigation of the most limiting factor(s) such as the thermal budget. Subsequently, approaches/concepts in overcoming these limitations need to be developed and examined in order to prove cw NW laser emission. Gaining insights into the underlying physics could potentially help to extend the successful approach to a broad range of NW laser devices and into optoelectronic applications.

(ii) The full potential of NW based coherent light sources can only be accessed when their laser dynamics are known and understood. **These ultrafast NW laser dynamics**, which are at the opposite side of the dynamic range compared to the infinitely long cw emission, remain also relatively unstudied, as they are difficult to measure for individual NW devices. They are expected to work in the ultrafast regime between hundreds of femtoseconds and a few picoseconds. Unfortunately, typical lasing investigations are carried out using time-integrated spectral measurements, which hide essential information on the operation speed of NW laser devices. As conventional ultrafast pulse characterization techniques, e.g. measuring the autocorrelation, fail due to the rather weak NW emission intensities, measuring the NW laser dynamics such as laser onset time and pulse width requires the usage of new suitable measurement techniques. Such a novel ultrafast measurement technique could by used in order to investigate the NW laser dynamics and how they depend on the semiconductor material and the optical properties of the device. This new fundamental understanding could subsequently be applied in order to study approaches to tune/adjust the temporal laser dynamics.

(iii) Although a few studies investigated the correlation of NW morphology and NW emission properties, they usually suffer from an insufficient sample/measurement geometry: The NW laser is lying on a low refractive index substrate, while its laser emission is typically collected perpendicular to the NW axis. Both substrate and collection direction obscure the angular emission distribution and the polarization of the lasing mode, which is an important feature of a coherent light source. In addition, static simulations were usually performed in literature in order to investigate

the transverse lasing mode(s) within the NWs as a function of the diameter. However, they disregard dynamical aspects of gain/absorption, carrier density dynamics etc. on the emission properties and transverse mode propagation. Thus, a desired new measurement setup needs to be developed for the investigation of the transverse NW laser modes, overcoming the limitations of the conventional measurement setup by directly imaging the angular emission distribution and polarization out of the NW laser end. The transverse lasing mode(s) could be directly determined as a function of the NW diameter using such a setup without any static simulations. Furthermore, the **transverse modes and the laser dynamics of individual NW lasers** could be correlated to the NW morphology by a combinatory study using this novel imaging technique and the ultrafast measurement technique. Finally, this study will show how optimal coupling of the NW laser emission into adjacent nanophotonic components and waveguides could be achieved. This will be an important step towards the integration of NW lasers on a chip following "More-than-Moore".

Following this **introduction**, this thesis begins with an overview of fundamental optical and luminescence properties of semiconductor NWs with a special focus on the effects in the high excitation regime. **Chapter 2 - Fundamentals** also addresses the basics of nanowire photonics and single NW lasing. This is followed by a brief introduction into the field of plasmonics explaining also the approach of coupling semiconductor NWs with metal films. **Chapter 3 - Methods** describes briefly the methods used for the experiments and simulations. The recently developed double-pump measurement technique for the investigation of the ultrafast NW laser dynamics is introduced here as well as the head-on measurement setup for the imaging of the transverse mode emission, which was realized and established within the scope of this thesis. The following chapters focus on the three challenges, as identified before.

Chapter 4 - Continuous wave lasing of tin doped CdS NWs discusses the use of high quality and high gain semiconductor NWs made of CdS for the realization of cw NW lasers. As the used NWs are synthesized by a novel growth route using Sn as catalyst, their structural and optical properties are characterized in order to evaluate whether they are suitable for the subsequent high excitation measurements under cw pumping. The occurrence of cw NW lasing is proven and its temperature dependence is investigated. The chapter is completed with the discussion of the gain mechanism and an outlook on how room temperature cw NW lasers could be realized. Parts of the results were published in references [34, 35] and the master's thesis of Marcel Wille [36].

The underlying physics of the double-pump technique are initially explained in **Chapter 5 - Ultrafast temporal dynamics**. This technique is used to measure the laser onset time for three different gain materials and different optical configurations in order to gain qualitative insights into the underlying ultrafast processes within in the gain material after photoexcitation, as published in reference [37]. Subsequently, the NW laser pulse width

is determined for photonic NW lasers on low refractive index substrates. These results are compared to the respective values for plasmonic NW lasers, which consist of a semiconductor NW on metallic film, as these plasmonic NW lasers are predicted to enhance the mode confinement and the spontaneous and stimulated emission rates in comparison to their photonic counterpart. These investigations are published in reference [38].
In **Chapter 6 - Mode switching in ZnO nanowire lasers**, the head-on measurement approach, as introduced in reference [39], is used in order to investigate the transverse mode properties of individual, thin ZnO NW lasers below the multimode cutoff in comparison to thick multimode ZnO NWs. Furthermore, this chapter highlights the influence of the NW diameter and hence the transverse mode on the laser dynamics. These results are compared to a novel dynamical simulation method, which is subsequently used in order to tailor an optimized NW laser morphology. Parts of this chapter are published in reference [40] and the master's thesis of Max Riediger [41].
Chapter 7 summarizes the main results of this thesis in respect to the three challenges. Fundamental conclusions are drawn presenting a major step on the route to unravel the fundamental operation principles of NW based laser systems in general.

2 Fundamentals

The scope of this thesis requires a splitting of the fundamentals into two parts: the first part deals with the fundamental background of semiconductors especially with their optical properties. Furthermore, it highlights their specific features related to the nanowire morphology. The second part includes a brief introduction into the field of plasmonics and envisages the potential of coupling plasmonics with high optical gain materials.

2.1 Semiconductor nanowires

2.1.1 Material systems

Cadmium sulfide. Cadmium sulfide (CdS) is a direct II-VI semiconductor with a wide band gap of $E_g = 2.58$ eV at $T = 1.6\,K$ [42]. Under ambient conditions, CdS crystallizes in the wurtzite structure [43], in which every Cd atom is surrounded by four sulphur atoms and vice versa, as schematically shown in figure 2.1a. The lattice parameters of the stable wurtzite crystal are $a = b = 4.14\,Å$ and $c = 6.72\,Å$ [43]. Thus, CdS is an optically anisotropic material with an ordinary (extraordinary) refractive index of $n_o = 2.83$ ($n_e = 2.77$) at a wavelength of $\lambda = 510\,nm$, which refers to a photon energy close to the band gap at room temperature (RT) [44, 45]. The dispersion at this wavelength has been determined to be $dn_o/d\lambda = -11.97\,\mu m^{-1}$ ($dn_e/d\lambda = -8.60\,\mu m^{-1}$) [45]. The band structure, schematically depicted in figure 2.1b, is determined by the tetrahedral coordinate bonding formed by the sp^3-hybrid orbitals. Considering CdS as an ionic crystal (the electronegativity difference between Cd and S is ≈ 1) the empty 5s-orbitals of Cd^{2+} form the conduction band (CB), while the completely occupied 3p-orbitals of S^{2-} form the valence band (compare figure 2.1b). The triple degeneracy of the p-like valence bands (VB) at the Γ point into sub-bands labelled A, B, C is lifted by the interaction of the spin-orbit coupling in combination with the hexagonal crystal field [42]. The energetic splitting between the sub-bands is $\Delta E_{AB} = 16\,meV$ and $\Delta E_{BC} = 57\,meV$, respectively. The transitions from the CB to the VB_A are only active for light with an electric field vector $\mathbf{E}$ perpendicular to the c axis ($\mathbf{E} \perp c$), whereas both other transitions are allowed for both polarization directions ($\mathbf{E} \perp c$ and $\mathbf{E} \parallel c$). Note that the dipole selection rules are not rigorous, thus even weak transitions from CB to VB_A with $\mathbf{E} \perp c$ can be observed in experiments [42].

Zinc oxide. Zinc oxide (ZnO) is also a II-VI semiconductor. It has a direct band gap of $E_g = 3.44\,eV$ at $T = 4.2\,K$ [46]. As in CdS, the wurtzite crystal phase is the most stable one at ambient conditions. The lattice parameters of ZnO are $a = b = 3.296\,Å$ and $c = 5.207\,Å$ [47]. Both materials, ZnO and CdS, have many properties in common, e.g. the optical anisotropy and the band structure (see figure 2.1b). In ZnO the splitting of the sub-

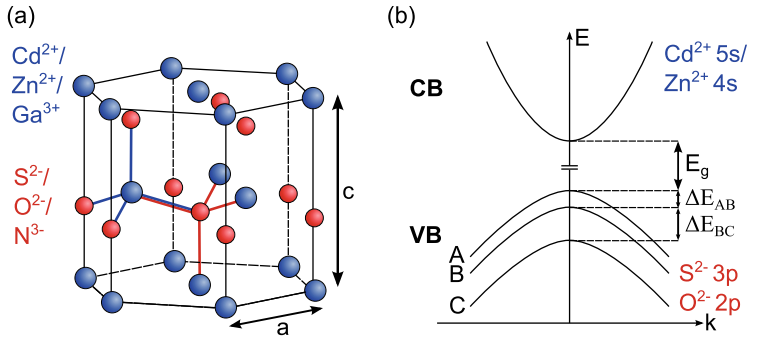

Figure 2.1: (a) Schematic drawing of the wurtzite unit cell of CdS, ZnO and GaN. The position of the cations (Cd^{2+}, Zn^{2+}, Ga^{3+}) and anions (S^{2-}, O^{2-}, N^{3-}) are marked in blue and red, respectively. The lattice constants a, c are labelled. (b) Sketch of the band extrema in CdS and ZnO showing the conduction band (CB) and the splitting of the valence band (VB) into three sub-bands A, B, C around the Γ point.

bands exhibits values of $\Delta E_{AB} = 4.9\,\text{meV}$ and $\Delta E_{BC} = 43.7\,\text{meV}$, respectively [48]. The refractive index is slightly lower than in CdS with an ordinary (extraordinary) refractive index of $n_o = 2.38$ ($n_e = 2.35$) at a wavelength of $\lambda = 385\,\text{nm}$ [49]. Reviews on ZnO with extensive information on structural, electrical and optical properties, as well as on the growth process for ZnO were published a decade ago [46, 50, 51].

Gallium nitride. Gallium nitride (GaN) is in contrast to the other two material systems a III-V compound semiconductor, which can form both the zinc blende and wurtzite phase [52]. However, only nanowires of the wurtzite polytype were used in this thesis, compare figure 2.1a. It exhibits a direct band gap of $E_g = 3.50\,\text{eV}$ at $T = 1.6\,\text{K}$ [53]. The lattice constants of wurtzite GaN are $a = b = 3.189\,\text{Å}$ and $c = 5.185\,\text{Å}$ [54]. The ordinary (extraordinary) refractive index of GaN is $n_o = 2.66$ ($n_e = 2.31$) at a wavelength of $\lambda = 365\,\text{nm}$, a photon energy similar to the optical band gap at room temperature [55]. The dispersion reveals values of $dn_o/d\lambda = -3.51\,\mu\text{m}^{-1}$ and $dn_e/d\lambda = -0.0023\,\mu\text{m}^{-1}$ at this wavelength [55]. Further information on structural, electrical and optical properties of GaN can be found in the reviews [56, 57].

2.1.2 Low excitation luminescence in semiconductors

The excitation of a semiconductor material by an energetic electron or a photon with an energy larger than the semiconductor band gap lifts an electron from the valence band into an excited state in the conduction band leaving a positively charged 'hole' back in the valence band. The charge carriers, electrons (e^-) and holes (h^+), convert their excess energy $\Delta E_{e(h)}$ into other forms of energy when they relax to the bottom of the conduction band and the top of the valence band, respectively [58]. This relaxation takes place very fast in the order of femto- to picoseconds after the excitation. Direct recombination of the carriers (band to band) is unlikely for the investigated semiconductor materials because of their large exciton binding energies.

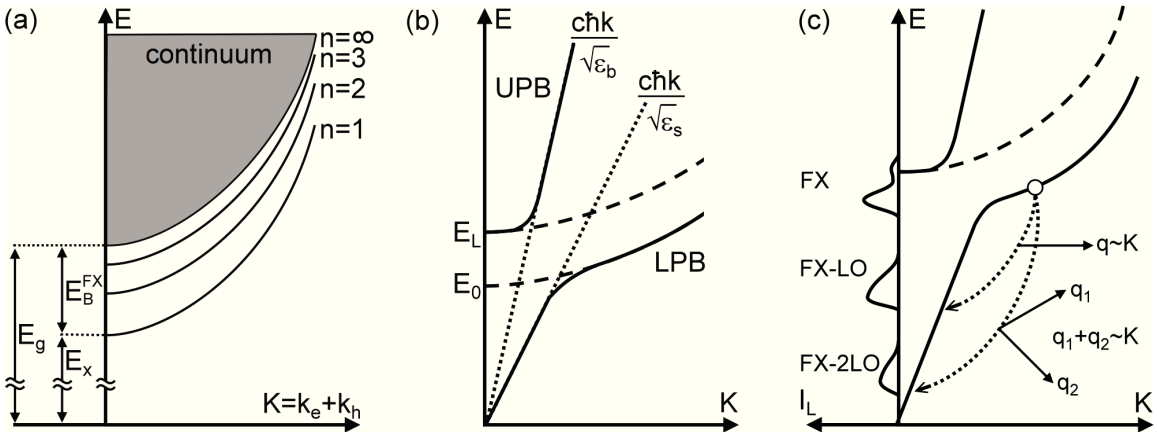

Figure 2.2: (a) Schematic drawing of the exciton dispersion relation depicting the ground (n = 1) as well as higher excited states (n ≥ 1). (b) Sketch of the exciton-polariton dispersion relation (black line) incorporating also the dispersion relation of photons (pointed line) and free excitons (dashed line). (c) Sketch of the recombination mechanism involving a free exciton (FX) interacting with longitudinal optical phonons (LO). Such a recombination leads to a photoluminescence emission shown on the left. (Drawings according to [50, 51, 58].)

Excitons. Photoexcited electrons and holes attract each other by Coulomb interaction in high purity and high quality semiconductors. This leads to a bound state by formation of a hydrogen-like quasiparticle called '(free) exciton' (FX) [59]. The spacial expansion of the exciton is defined by the exciton Bohr radius a_B, which is 2.8 nm for CdS [60], 1.8 nm for ZnO [61] and $\sim 3.0 - 3.6$ nm for GaN [57, 62]. The Coulomb interaction of an electron hole pair is largely screened in these compound semiconductors by the valence electrons. Therefore, the exciton Bohr radii are larger than the unit cell. Such weakly bound excitons are known as Wannier excitons [59]. The emission energy E_X of a photon due to excitonic recombination is therefore less than E_g by the value of the exciton binding energy of electron and hole E_B^{FX}, which is 28 meV for CdS [42], 60 meV for ZnO [50] and 26 meV for GaN [57] in the ground state n = 1 (see figure 2.2a). The excitons are stable at, or close to, room temperature since their binding energies are comparable to the thermal energy at room temperature of 25 meV. The lifetimes of the excitons depend strongly on the exciton oscillator strength and crystal quality and are typically in the range of tens of picoseconds to few nanoseconds [63–67].

Exciton polariton. Excitonic excitations in semiconductors cannot be treated independently from the electromagnetic light field. Instead, excitons and photons couple, forming quanta of mixed states of electromagnetic radiation and semiconductor excitation. In other words, an incident photon creates an electron-hole pair, which recombines again, emitting a photon, and so on [58]. This process is a representation of the exciton polariton with a dispersion relation, as depicted in figure 2.2b. The linear photon dispersion (dotted line in figure 2.2b), whose slopes are determined by the background (ε_b) and the static dielectric function (ε_s), crosses the parabola shaped dispersion relation

(dashed line) of the longitudinal (transversal) exciton E_L (E_0). According to the quantum-mechanical "non-crossing rule", the exciton-polariton dispersion splits into the lower and the upper polariton branch (LPB and UPB) [58]. Exciton-polaritons in the UPB follow the excitonic dispersion for small momentum (K) values and approach the photon dispersion for high K-values, while exciton-polaritons in the LPB follow the linear photon dispersion for small K-values and approach the excitonic dispersion for high K-values. Excitations of semiconductors by photons with energies much larger than the band gap lead to the creation of excitons in the UPB, which subsequently relax into the LPB by interaction/scattering with phonons. In matter, the excitation of excitons always refers to polaritons, because both cannot be considered separately. Throughout this thesis, the term 'exciton' is used equivalently to 'exciton polariton'.

Bound excitons. At low temperatures the excitons can localize at imperfections in the crystal lattice via van der Waals interaction [59], because of their low kinetic energies. Thus, bound exciton emission is the dominant recombination channel at sufficiently low temperatures [48]. The excitonic emission energy is therefore further lowered by the binding energy of the exciton to the impurity, which can be either intrinsic crystal defects, such as interstitial atoms and vacancies, or extrinsic defects, such as acceptors or donors [48,59]. Typically, the binding energy of an exciton is highest at a neutral acceptor (AX), lower at a neutral donor (DX) and even lower at an ionized donor (D^+X) [58]. The binding of an exciton with an ionized acceptor is usually not observed, since the formation of a free electron and a neutral acceptor is energetically more favorable [58]. The binding of an exciton to a neutral acceptor (donor) is generally less stable than a binding of a hole (electron) to such an impurity and can be estimated to be ~ 0.1 times as strong according to "Haynes rule" [68,69]. Furthermore, excitons may also bind to point defects other than single shallow acceptors and donors, such as deep centers. Both, CdS and ZnO, which are extensively considered within this thesis, exhibit an intrinsic n-type behaviour because their main impurities are shallow donors [42,46]. Thus, low temperature emission spectra of CdS and ZnO are dominated by DX lines. As bound excitons exhibit a lack of kinetic energy compared to FX, their spectral emission lines occur very sharp in contrast to the emission lines of the FX.

Carrier recombinations at impurities. Besides free and bound excitons, recombinations involving separated electrons and holes also need to be considered. Charge carriers 'freeze out' at impurities at sufficiently low temperatures. Hence, transitions of a free carrier and a charge bound to an impurity may become probable at low photoexcitation. Such transitions are known as free-to-bound transitions [59,70]. Free electrons (holes) can

recombine radiatively (sometimes also non-radiatively) with a hole (electron) trapped at an acceptor (donor). The emission energy of this (e,A) or (h,D) transitions is given by:

$$E_{Ph} = E_g - E_{A(,D)}, \tag{2.1}$$

with $E_{A(,D)}$ being the activation energy of the acceptor (donor) state.
If a semiconductor contains both donors and acceptors, donor-acceptor pair (DAP) transitions have to be taken into account as well [48, 57, 71]. Here, a donor bound electron recombines with an acceptor bound hole, emitting a photon with an energy of:

$$E_{Ph} = E_g - E_A - E_D + e^2/\left(4\pi\varepsilon_0 r_{AD}\right). \tag{2.2}$$

The energy is increased by $e^2/\left(4\pi\varepsilon_0 r_{AD}\right)$, since the energy of the final state is decreased by the Coulomb attraction of the ionized donor and acceptor separated by their distance r_{AD}. The charge carriers, electrons and holes, are spatially separated in DAP transitions, thus the radiative recombination probability depends on the overlap of the respective wave functions and therefore on the spatial distance between donor and acceptor r_{AD} [59, 72].

Phonon interaction. Charge carriers and excitons interact with the crystal lattice of the semiconductor, so that a part of their recombination energy can generate one or more phonons. In general, the carriers can couple to several optical and acoustic phonon modes during recombination, which are furthermore divided in longitudinal and transversal phonon modes [58]. The coupling to the longitudinal optical (LO) phonons is strongest, because lattice atoms vibrate antiphase in optical phonon modes [73], creating a dipole moment, which couples efficiently to the electromagnetic field. Atoms oscillate in phase in acoustic phonon modes leading to a low coupling efficiency. The LO phonon reveals an energy of 38 meV for CdS [74, 75], 72 meV for ZnO [76] and 92 meV for GaN [57]. Therefore, the coupling to LO phonons is a possible luminescence channel and the original emission (zero-phonon-line, ZPL) is accompanied by emission lines (phonon replica), which are reduced by the energy of one or multiple phonons: $n \cdot \hbar\omega_{LO}$. This is schematically shown in figure 2.2c for the case of a free exciton.

Deep level recombinations. In the theoretical background given so far, only emission features of excitonic origin or introduced by shallow impurities were considered. These have emission energies around E_g. These emission features are usually referred to as near band edge emission (NBE). However, a mixture of equilibrium imperfections are generally present in crystals creating additional deep level states within the band gap and giving rise to phenomena such as colour centers [77]. Carriers can be trapped at such defect states and subsequently recombine by emission of a photon (deep level emission, DLE). These defects can be of intrinsic nature: Point defects (vacancies, interstitial atoms) as well as anti-sites or defect complexes [46, 57, 72, 78]. Furthermore, extended defects like

stacking faults can also be origins of deep optically active levels [48,79,80]. Unfortunately, the recombination mechanisms/paths, as well as exact energetic levels of the defects are unknown in most cases and therefore still debated in literature [46,81,82]. Some defects can also occur in several charge states [81, 83]. As a rule of thumb, it is thought that recombinations at interstitial atoms occur at higher energies than at vacancy states [57]. Impurity atoms on interstitial or substitutional states are referred to as extrinsic defects. Such extrinsic defects, like e.g. Cu in ZnO [84–86], induce optically active levels within the band gap. Both, intrinsic and extrinsic defects cause distortions of the crystal lattice resulting in a strong interaction with phonons. Hence, the direct carrier recombination at defects is often accompanied by phonon replica. A more quantitative analysis of the carrier-phonon coupling strength is usually made by evaluating the Huang-Rhys factor S [87,88]. If electron (hole)-phonon coupling is weak, the ZPL will dominate and S reveals small values. The ZPL intensity decreases, while the phonon replica intensity increases for enhanced carrier-phonon interaction resulting in large values of $S > 1$.
The interaction of charge carriers with phonons is usually studied at low temperatures. Phonons are bosonic particles and their population increases at elevated temperatures. Thus, e.g. acoustic phonons may cause broadening of the emission with increasing temperature [89]. Strong interaction with phonons may even result in non-radiative recombinations [90].

Non-radiative recombination. Apart from radiative recombinations, excited semiconductors may recover by several alternative processes. These non-radiative transitions redistribute the absorbed energy among electronic excitations or among lattice vibrations [90]. Non-radiative recombinations usually suppress luminescence and reduce carrier lifetimes, thus they are sometimes referred to as "killer centers". Non-radiative recombinations are often thought to arise from surface or defect-related sites [58, 91]. A review on non-radiative recombinations in semiconductors was published elsewhere [90].

2.1.3 High excitation luminscence in semiconductors

All recombination processes discussed in the previous chapter occur in the low excitation regime, where the electron-hole pair concentration n_p is low, so that interactions between carriers could be neglected due to their large spatial separation. Here, the optical properties arise mainly from single electron-hole pairs, either in excitonic states or in the continuum [58] (compare figure 2.2). Also, the emission intensity usually depends linearly on the excitation power, if no saturation effects occur. With increasing electron-hole pair concentration n_p one reaches the intermediate (medium) density regime, in which the Coulomb attraction of electron and hole starts to be screened. Nevertheless, excitons are still treated as quasiparticles, but they start to interact with each other [58]. Elastic and inelastic scattering processes can occur between excitons, and between excitons and free carriers at elevated temperatures, as schematically depicted in figure 2.3a. In-

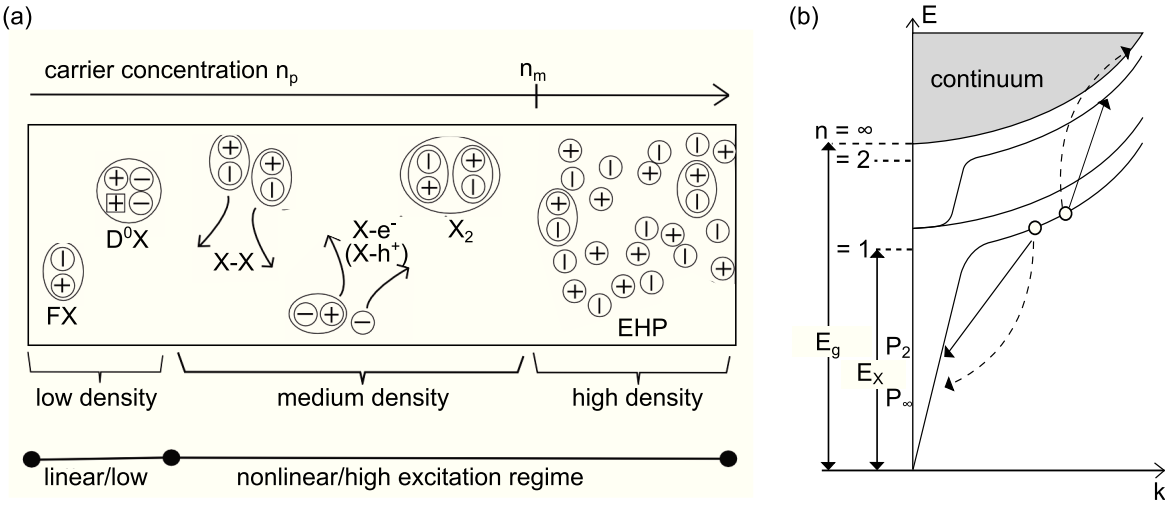

Figure 2.3: (a) Schematic overview over quasiparticles and their interaction in different excitation regimes and for different carrier densities. At low excitation only single electron-hole pairs (FX, D^0X) determine the optical properties, while scattering processes occur at medium carrier densities (X-X, X-e^-, X-h^+), as well as the formation of biexcitons (X_2). Carriers form an electron-hole plasma (EHP) at carrier densities above the Mott density n_m. (b) Schematic drawing of the exciton dispersion relation and inelastic exciton-exciton (X-X) scattering, which causes characteristic emission bands (P_2, $P_3, \ldots, P_\infty$). (Drawings according to [58].)

creasing the excitation further results in enhanced screening of the Coulomb interaction until the excitons dissolve finally into free carriers [51]. Consequently, new luminescence band/recombination channels appear, in the medium and high excitation regimes, which are described below and shown in figure 2.3a.

Scattering processes and biexcitons. Due to high carrier concentrations in the medium density regime, the excitons feel each others Coulomb interaction and excitons scatter with each other via mutual dipole-dipole interaction (while a dipole-monopole interaction characterizes the scattering of excitons with free carriers) [58, 92]. Elastic scattering causes a homogeneous broadening of the exciton resonance and reduced exciton lifetimes [58]. During inelastic scattering, one exciton is lifted to a higher excitonic state, while the other one is scattered to the photonic part of the LPB. The exciton in the LPB then recombines by emitting a photon of the "P_n band" ($n = 2, \ldots, \infty$). Emission energies of the "P_n band" photons are given by:

$$\hbar\omega_P = E_g\,(T) - \left(2 - 1/n^2\right) E_B^{FX} + 3/2 \cdot k_B T, \tag{2.3}$$

where k_B is Boltzmann's constant [51]. The exciton, which was lifted into an excited state, relaxes as usual back to the ground state. This process is schematically shown in figure 2.3b. The probability of exciton scattering increases superlinear with the carrier concentration and the emission of the P band shows a quadratic dependence on the excitation power [93]. At high exciton concentrations, two excitons may form a new

quasiparticle - the so called biexciton or exciton molecule (X_2). Radiative recombination of the X_2 causes the "M band" emission, which is red-shifted compared to the FX emission and exhibits a superlinear slope in the excitation dependence [93–95]. Note, that two electrons and one hole (or vice versa) may also bind resulting into a trion (X_2^- and X_2^+) [58].

Electron-hole plasma. If the carrier density increases even further, the high density regime is achieved, where the excitons lose their quasiparticle nature and a collective phase is formed. The density of electron-hole pairs n_p is now high enough, so that the mean exciton distance approaches and even falls below the exciton Bohr radius a_B. Overcoming the critical concentration n_m with $a_B^3 \cdot n_m \approx 1$ (as a rule of thumb) initiates the dissolution of excitons into free carriers [58]. The critical density n_m is referred to as Mott density. Various effects appear at such high carrier densities $n_p \geq n_m$: The intensified carrier screening effect causes a monotonic shrinking of the band gap $E_g(n_p)$ (band gap renormalization). The second effect is that excitons (for $n_p \leq n_m$) already experience significant screening. Consequently, their binding energy decreases and the exciton state shifts closer to the band gap. Both effects, band gap renormalization and exciton screening, almost compensate each other, thus the emission energy of the FX remains more or less constant at $E_g - E_B^{FX}$ [51]. The Mott density therefore describes the carrier density at which the renormalized band gap falls below the emission energy of the FX: $E_g(n_p \geq n_m) \leq E_X$. The transition into the collective EHP phase is not sharp, especially at elevated temperatures. Mott densities have been determined to be $\sim 2.8 \cdot 10^{17}\mathrm{cm}^{-3}$ for CdS [96], $5 \cdot 10^{17} - 10^{19}\mathrm{cm}^{-3}$ for ZnO [50] and $\sim 1.8 \cdot 10^{18} - 3.8 \cdot 10^{18}\mathrm{cm}^{-3}$ for GaN [97] at low temperatures. The emission of the EHP arises from the recombination of electrons and holes in the conduction and valence band, respectively, which are filled up to the quasi Fermi energy E_F^e and E_F^h (compare figure 2.4a). The energetic distance between the quasi Fermi levels defines the chemical potential $\mu(n_p, T)$. Emission of the EHP occurs, if momentum conservation is fulfilled with a spectral width of $\Delta E = \mu - E_g(n_p)$. An increasing carrier concentration elevates the chemical potential as the bands fill up with carriers, but also band gap renormalization occurs. As both processes appear simultaneously, this leads to spectral broadening at the lower energy side for increasing carrier concentrations [51].

2.1.4 Laser Theory

Optical gain in semiconductors. Light travelling through matter is usually attenuated by absorption and scattering. This process is described by the Lambert-Beer law: $I(E,d) = I_0 \cdot e^{-\alpha(E)\cdot d}$, with I_0 as the initial intensity, $\alpha(E)$ the energy dependent absorption coefficient and d the travelled distance. In excited semiconductors, some of the processes considered in chapter 2.1.3 may cause optical gain $g(E) = -\alpha(E)$, so that light travelling through the material is amplified. Light amplification via stimulated recombination is pronounced in the intermediate and high excitation regime, where multiple processes

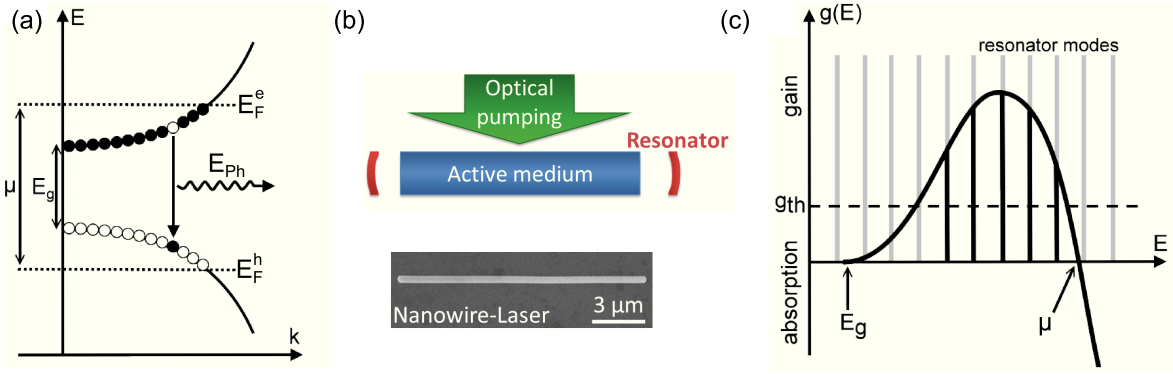

Figure 2.4: (a) Sketch of the emission process within an EHP. The electrons and holes occupy states up to the quasi Fermi energies E_F^e and E_F^h, respectively. (b) Schematic depiction of an optically pumped laser system. Optical pumping (green) of an active medium (blue) may induce optical gain. The laser resonator is defined by the cavity length and the reflectivities (red). A semiconductor NW, as shown in the SEM image, forms the active medium as well as the resonator. (c) Schematic graph of the gain formed in an EHP occurring between E_g and μ. The resonator modes with a gain value above the threshold g_{th} exhibit amplification.

provide gain: X-X scattering (P band) already leads to optical gain at moderate exciton concentrations, while X-LO and X-e^- scattering require higher densities of excitons [98]. At carrier concentrations above the Mott transition light amplification is attributed to the formation of the EHP, which is most likely the origin of laser oscillations in semiconductor NWs, as discussed later. In the EHP, the high k states form the excited states, which allow absorption of photons to pump the system. This initially created distribution of carriers relaxes quickly (∼fs) by various elastic and inelastic scattering processes with other carriers and phonons to lower k states [99]. Finally, the relaxed electrons and holes recombine by emitting a photon, as shown in figure 2.4a. Population inversion can be reached, because the lifetime of relaxed carriers (∼ps) is longer than the relaxation process. Therefore, the recombination process in an EHP can be treated as a laser level system enabling optical gain:

$$g \sim g_0 \sqrt{E - E_0} \left(f_e \left(E, n_p \right) - f_h \left(E, n_p \right) - 1 \right). \tag{2.4}$$

Here, g_0 is the gain coefficient and $f_{e,h}$ the Fermi distribution of electrons and holes, respectively [100]. The gain coefficient of an EHP is a fundamental property of the semiconductor material. Note, that light with an energy below E_g is not amplified, because the material is transparent. The gain spectrum also reveals an upper limit at the so called transparency point μ, where strong absorption occurs [58]. Typical values for the maximum gain are $\sim 2.8 \cdot 10^4$ cm^{-1} for CdS [96], $\sim 7 \cdot 10^3$ cm^{-1} for ZnO [101] and $\sim 1 \cdot 10^4$ cm^{-1} for GaN [102] at low temperatures.

Semiconductor laser. The main components of conventional laser systems are illustrated in figure 2.4b. If the gain (active) medium is embedded in a resonator, standing

electromagnetic waves (cavity modes) are established, which enable further light amplification according to the LASER principle [4]. The so called modal gain ($g_{modal}(E)$) defines the light amplification of the cavity/resonator mode propagating through the active medium:

$$g_{modal}(E) = \Gamma \cdot g(E). \tag{2.5}$$

Accordingly, the confinement factor Γ connects material and modal gain. Its physical quantity is determined by the overlap of the guided resonator mode with the excited active material [103]. Emission amplification in terms of lasing requires that the modal gain overcomes all loss mechanisms during its round trip through the resonator [104]:

$$g_{modal}(E) \geq g_{th} = \alpha(E) + \alpha_W(E) + \alpha_R(E). \tag{2.6}$$

The threshold gain value for lasing g_{th} compensates the loss meachnism due to absorption and scattering $\alpha(E)$, waveguide losses $\alpha_W(E)$, as well as mirror losses $\alpha_R(E)$. Mirror losses are given by:

$$\alpha_R(E) = \frac{1}{2L} \cdot \ln\frac{1}{R_1(E) \cdot R_2(E)}, \tag{2.7}$$

where $R_{1,2}$ are the reflectivities of the resonator with length L. In short, resonator modes exhibiting enough optical gain are amplified, as illustrated in figure 2.4c.

Theoretical multimode laser model. In simple atomic-like laser level models, the rate equations describe the population N_i remaining in i^{th} energy level. Then, the rate equations of a three (or four) level laser system can be solved either analytically (making some assumptions, such as that the highest excited state is always depopulated by fast relaxation) or numerically to describe the laser characteristic. The multimode laser model of Casperson is applied within this thesis to describe the laser characteristic, as it is well suited for semiconductor lasers [105]. If other approaches/models are used, it will be explained explicitly. Casperson developed an analytical model for the power dependence of multiple, simultaneously present laser modes (longitudinal and/or transversal), when the mode spacing is small compared to the width of the gain envelope. If this is the case, the overall intensity of the competing laser modes impinging on the mirror x_t is directly proportional to the output intensity of the laser. The intensity x_t is shown in figure 2.5a as a function of the gain/loss ratio per resonator cycle. The parameter x_0 determines the spontaneous emission input to the laser as fraction of the total spontaneous emission of the material. For small values of $x_0 \ll 1$ the transition from spontaneous emission below threshold (gain/loss = 1) to laser emission becomes more pronounced in terms of a steeper slope around the threshold. With $x_0 \approx 1$ the transition vanishes at all. The transition from spontaneous to laser emission is referred to as the amplified spontaneous emission (ASE) regime. Furthermore, the intensities of spontaneous and laser emission depend linearly on the pumping intensity, as shown in figure 2.5a.

2.1.5 Polarization and Stokes parameters

Light can be characterized by the two electric field components perpendicular to its propagation direction: $\mathbf{E}(t) = \mathbf{E}_x(t) + \mathbf{E}_y(t)$. Therefore, Stokes defined a set of four parameters (S_0 - S_3) to describe the polarization $\mathbf{E}$ of quasi-monochromatic light by means of field intensities [106]:

$$\begin{aligned} S_0 = \left\langle E_{0x}^2 \right\rangle + \left\langle E_{0y}^2 \right\rangle ;\, S_1 = \left\langle E_{0x}^2 \right\rangle - \left\langle E_{0y}^2 \right\rangle ; \\ S_2 = \langle 2E_{0x}E_{0y}\cos\delta \rangle \,;\, S_3 = \langle 2E_{0x}E_{0y}\sin\delta \rangle \,. \end{aligned} \tag{2.8}$$

Here, $\langle\rangle$ depicts the time average of the quadratic field components and $\delta = \delta_y - \delta_x$ the phase difference. Thus, the total intensity is described by the parameter S_0, while $S_{1,2,3}$ define the different polarization states: S_1 distinguishes horizontal ($S_1 > 0$) from vertical polarization ($S_1 < 0$). From S_2 the orientation $\pm 45°$ ($S_2 \gtrless 0$) is obtained, while S_3 specifies the rotation direction (right handed rotation for $S_3 > 0$ and left handed rotation for $S_3 < 0$, respectively) [106]. The Stokes parameter are suited to evaluate completely polarized light but also unpolarized and partially polarized light as well:

$$S_0^2 \geq S_1^2 + S_2^2 + S_3^2. \tag{2.9}$$

The equality applies to completely polarized light, while the inequality represents unpolarized and partially polarized light. So, the degree of polarization P [0:1] is defined as ratio of polarized light to total intensity $P = \sqrt{S_1^2 + S_2^2 + S_3^2}/S_0$ [107].

2.1.6 Nanowire photonics

Waveguiding. Semiconductor NWs exhibit excellent waveguide properties. According to the principle of step-index fibers they can guide light with a vacuum wavelength even larger than the NW diameter with low losses [20,108,109]. For the step-index-like nanowire waveguides the cladding is extended to infinity and formed by air/vacuum and/or a substrate ($n_{clad.} \sim 1 - 1.5$), while the NW itself serves as high index core ($n_{core} \geq 2$). Because of this large index contrast, NW waveguides usually provide stronger confinement of the light field than conventional macroscopic silica fibers. Nanowires with diameters below a critical value d_{min} do not confine the light completely, so that an increasing amount of the electromagnetic wave extends into the surrounding propagating as evanescent wave [20]. In principle, finding all supported modes requires the solution of Maxwell's equation. This can be done analytically for free standing NWs, but due to the asymmetry introduced by the supporting substrate, usually numerical calculations are performed for real NW devices. Figure 2.5b shows a plot of the effective mode index n_{eff} as a function of the nanowire diameter. In this case the substrate has a refractive index of ~ 1.5, while the NW reveals a refractive index of ~ 2.8 and the light wavelength is set to 510 nm. This plot therefore depicts waveguiding in an unexcited CdS NW for a wavelength slightly below the material band gap. The mode indices of the photonic modes lie between the refractive

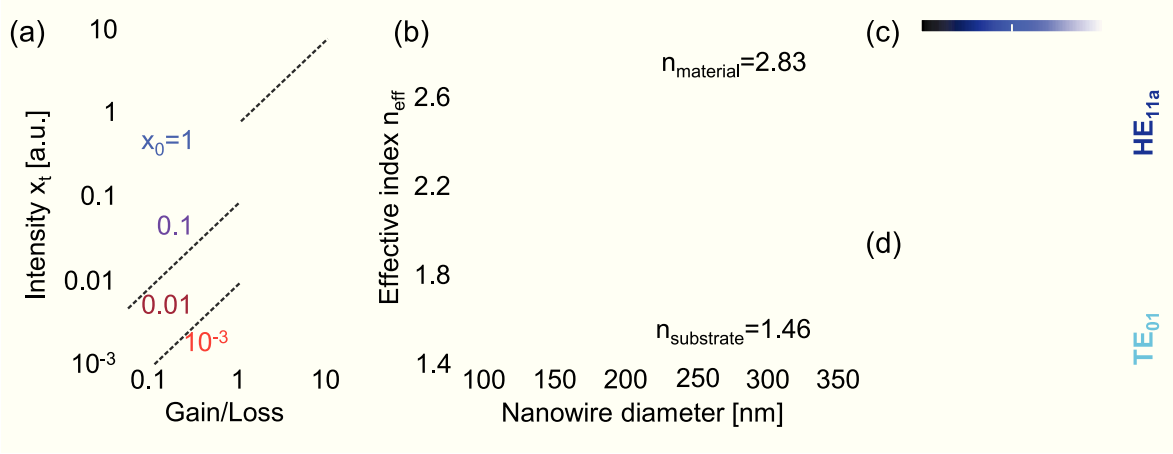

Figure 2.5: (a) The double logarithmic plot shows the laser characteristic/power dependence of a multimode laser system as a function of the gain/loss ratio per resonator cycle for different values of the laser parameter x_0 [105]. The dashed lines indicate a linear dependence. (b) The effective mode index n_{eff} of the waveguide modes calculated using COMSOL for a wavelength of 510 nm as a function of the NW diameter. The cutoff of the fundamental mode occurs at $\sim$ 125 nm. Multimode waveguiding occurs for diameters $\gtrsim$ 175 nm. (c,d) Electric field distribution in a photonic NW (diameter 200 nm) lasing geometry on SiO_2 substrate at 510 nm wavelength. Colour plot (c) shows the HE_{11a} mode and (d) the TE_{01} mode, respectively.

index of the material and the substrate. The mode index increases and approaches the material index in NWs of a large diameter. Note, while photonic modes remain hardly affected by the substrate for large diameters, the modes are pulled into the substrate for small diameters. Indeed, it is apparent from figure 2.5b that the modes lose confinement for decreasing diameter. Below $\sim$ 175 nm only the fundamental mode(s), which are not degenerated because of the substrate, are guided efficiently. The fundamental HE mode exhibits a cutoff for diameters below $\sim$ 125 nm. Figures 2.5c,d show the field distribution of the fundamental HE_{11a} and the higher order TE_{01} mode.

Nanowire resonator. The nanowire morphology inherently provides an effective resonator type cavity. Large differences in refractive index at the NW end facets cause partial reflection of the impinging light. Thus, the guided light bounces back and forth like in a Fabry-Pérot (FP) type resonator (compare figure 2.4b). Since the reflected wave interferes with the incoming wave, standing waves built up in the NW resonator, causing modulations in the emission spectrum [22, 110]. Note, that reflection at the side facets also become possible for large nanowire diameters, leading to whispering-gallery (WG) type resonances [111, 112]. The FP and WG type resonators are distinguished by their mode spacing.

The reflection at the NW end facet is different for each waveguide mode and depends strongly on the refractive index change and the NW diameter. The analysis of the reflection coefficients again requires numerical methods like finite-difference time-domain (FDTD) simulations. A full analysis of the reflection coefficient for each mode, diameter

and material are out of scope of this thesis and the reader is referred to the respective literature [113, 114]. For high refractive index semiconductor NWs (e.g. CdS, ZnO and GaN) it has been shown that the TE_{01} mode exhibits the highest reflection coefficients of around ~ 0.7. In contrast, the fundamental HE_{11} mode has only a reflection coefficient of ~ 0.4 [113, 114]. These are values of the reflection coefficient at the emission wavelength of the NBE.

Modal gain and nanowire lasing. Beside the resonator morphology, the semiconductor material can provide optical gain e.g. due to high optical excitation (see section 2.1.3). Furthermore, NWs benefit from the efficient waveguiding with high optical mode confinement. Thus, the overlap of active medium and guided mode becomes ideal with confinement factors of $\Gamma \approx 1$. The confinement factor Γ can even exceed one, if the modes propagate for a longer distance than the NW length [115]. Consequently, a high modal gain is realized using semiconductor NWs.
Because they provide the resonator morphology, as well as the high optical gain, single semiconductor NWs are suitable laser systems. Furthermore, NWs are possibly the smallest coherent light source based on pure photonic modes. Indeed, laser oscillations in single semiconductor NWs have been reported for a decade now [116], in particular for CdS [23], ZnO [22] and GaN NWs [110].

2.2 Plasmonics

Collective longitudinal oscillations of quasi-free electrons in bulk materials (typically metals) are referred to as volume plasmons. The excitation of such volume plasmons requires energies of $\sim 10\,\mathrm{eV}$ [73]. Collective electron oscillations exist also at the interface of metals. They are called 'surface plasmons' and their electric field extends into the dielectric/vacuum. Surface plasmons exhibit lower energies than their volume counter parts and can be assessed even at optical energies. Surface plasmons are strongly localized at the interface, because their electromagnetic field decays evanescently away from the interface [117].

2.2.1 Permittivity of metals and silver films

Quasi-free electrons in metals are treated as a free electron gas of density n moving against the positively charged background of fixed metal ion cores. In the Drude model [117], the motion of electrons is determined by the equation:

$$\mathrm{m_{eff}} \cdot \ddot{\mathbf{x}} + \mathrm{m_{eff}} \cdot \gamma \cdot \dot{\mathbf{x}} = -\mathrm{e} \cdot \mathbf{E}, \tag{2.10}$$

where $\mathrm{m_{eff}}$ is the effective mass of the electron, e the electron charge and γ the damping of the electron oscillation. Every displaced atom causes a net polarization $\mathbf{P} = \mathrm{ne} \cdot \mathbf{x}\,(\mathrm{t})$.

From the relation for the electric displacement $\mathbf{D} = \varepsilon_0 \varepsilon_\mathrm{b} \mathbf{E} + \mathbf{P}$, the frequency dependent permittivity is determined as

$$\varepsilon(\omega) = \varepsilon_\mathrm{b} - \frac{\omega_\mathrm{p}^2}{\omega^2 + \mathrm{i}\gamma\omega} = \varepsilon' + \mathrm{i}\varepsilon''. \tag{2.11}$$

In equation 2.11, $\omega_\mathrm{p} = \sqrt{\mathrm{ne}/\varepsilon_0 \mathrm{m}_\mathrm{eff}}$ is the plasma frequency, ε_0 is the vacuum permittivity and ε_b the background permittivity, respectively [117].
The Drude model predicts the permittivity of silver films quite well only for low energies ≤ 1.5 eV. Thus, the model has to be extended for correct description of the visible/near-UV spectral range. Sidiropoulos [118] has shown that the model proposed by Rakic et al. [119] improves the description by using the Brendel-Bormann model [120], because it takes the interband parts of the dielectric function correctly into account.

2.2.2 Surface plasmon polaritons

Surface plasmon polaritons (SPP) are electromagnetic surface waves propagating at the interface between dielectric and conducting material. These SPPs are caused by the coupling of the electromagnetic field to the electron plasma of the conducting material/metal [117]. Figure 2.6a schematically shows a SPP on a metal - dielectric interface with permittivities ε_1 and ε_2, respectively. Since its electric field component perpendicular to the interface decays evanescently into both materials, the SPP is strongly confined to the interface. Further physical understanding arises from the dispersion relation of the SPPs. A detailed derivation of the SPP dispersion can be found in the literature [117]. Solving Maxwell's equation and taking continuity conditions across the boundary into account defines the dispersion relation for the propagation constant β of a bound TM polarized wave [117]:

$$\beta = \frac{\omega}{\mathrm{c}} \sqrt{\frac{\varepsilon_1 \varepsilon_2}{\varepsilon_1 + \varepsilon_2}}. \tag{2.12}$$

Note, that no bound waves with TE polarization exist for this geometry and SPPs only exist for TM polarization.
Here, only plasmons strongly bound to the interface are considered, which requires an evanescent component perpendicular to the interface. This condition is fulfilled for $\varepsilon_2 < -\varepsilon_1$ and $\varepsilon_2 < \mid \varepsilon_1 \mid$. Figure 2.6b (blue solid line) schematically depicts the dispersion relation for a metal-air ($\varepsilon_2 = 1$) interface with negligible losses in the metal ($\varepsilon_1'' \approx 0$). For low energies ($\omega \to 0$) the SPP dispersion approaches the light line $\omega = \beta \mathrm{c}$. The SPP momentum increases for higher frequencies and tends to infinity, when frequencies asymptotically converge to the surface plasmon frequency:

$$\omega_\mathrm{sp} = \frac{\omega_\mathrm{p}}{\sqrt{\varepsilon_b + \varepsilon_2}} \tag{2.13}$$

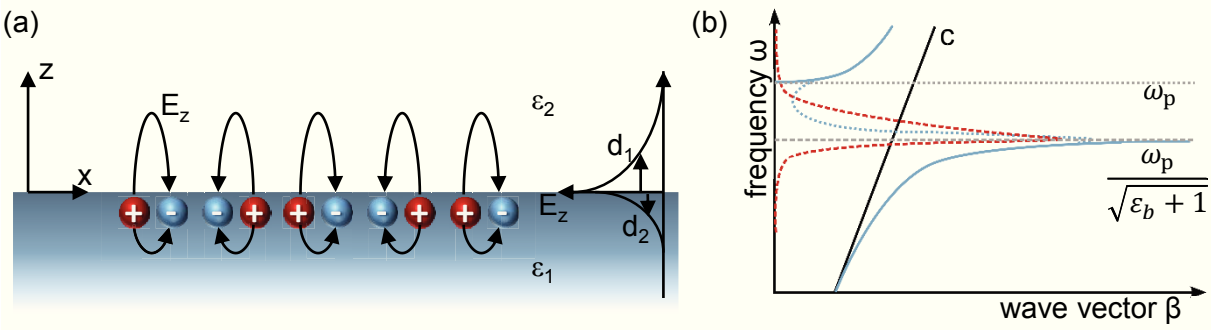

Figure 2.6: (a) Schematic drawing of the surface plasmon oscillations along an interface between metal (ε_1) and dielectric (ε_2). The planar surface extends into the y-direction. The plasmon propagates along the x-axis, while the evanescent electric field (E_z) oscillates perpendicularly to the interface. The field E_z decays exponentially into the metal and dielectric over decay lengths d_1 and d_2, respectively. (b) Sketch of the dispersion relation of surface plasmon polaritons (SPP). The dispersion relation of SPPs assuming negligible metal losses ($\varepsilon_1'' \approx 0$) is depicted as the blue solid line. If the metal losses are taken into account, the propagation constant (blue dotted curve) reaches a finite momentum, while losses (red dashed curve) reach a maximum. The black line shows the dispersion of light.

Thus, both the group velocity ($\partial\omega/\partial\beta$) and the phase velocity (ω/β) tend towards zero for $\omega \to \omega_{sp}$, defining the SPP regime of localized oscillations of the electron density. A frequency gap appears above ω_{sp} until the frequency ω overcomes the plasma frequency ω_p. The upper branch ($\omega > \omega_p$) describes volume plasmons [117].
The dispersion relation for SPPs including the metallic losses ($\varepsilon_1'' < 0$) is shown in figure 2.6b (blue dashed line). Now, the SPP momentum reaches a finite value close to ω_{sp}. Additionally, the losses reach a maximum, see dashed red curve in figure 2.6b. Obviously, the real and imaginary part of the SPP dispersion are $\beta' \approx \beta''$. In other words, the SPP decays in less than one optical cycle inhibiting efficient SPP propagation.

2.2.3 Plasmonic confinement

The SPP dispersion exhibits a photon-like character for small frequencies, while it becomes plasmon-like, when it bends away from the light line for higher SPP momentum. The plasmon-like SPPs reveal a strong confinement to the interface. The confinement is defined by the distance d_i in z-direction, for which the electric field decays by 1/e (see figure 2.6a). This decay depends on the imaginary part of the wave vector k_z by $e^{-z/d_i} = e^{-2k''_{z,i}z}$ and is shown in figure 2.7a. Photon-like SPPs have a large penetration depth into the dielectric ($d_2 \to \infty$), whereas the field nearly doesn't penetrate at all into the metal ($d_1 \to 0$). Instead, plasmon-like SPPs become more confined to the interface with increasing frequency. When the SPP dispersion tends away from the light line at higher momentum, the confinement falls even below the diffraction limit, $d_2 < \lambda/2$. Additionally, the SPP field starts to penetrate into the metal region.

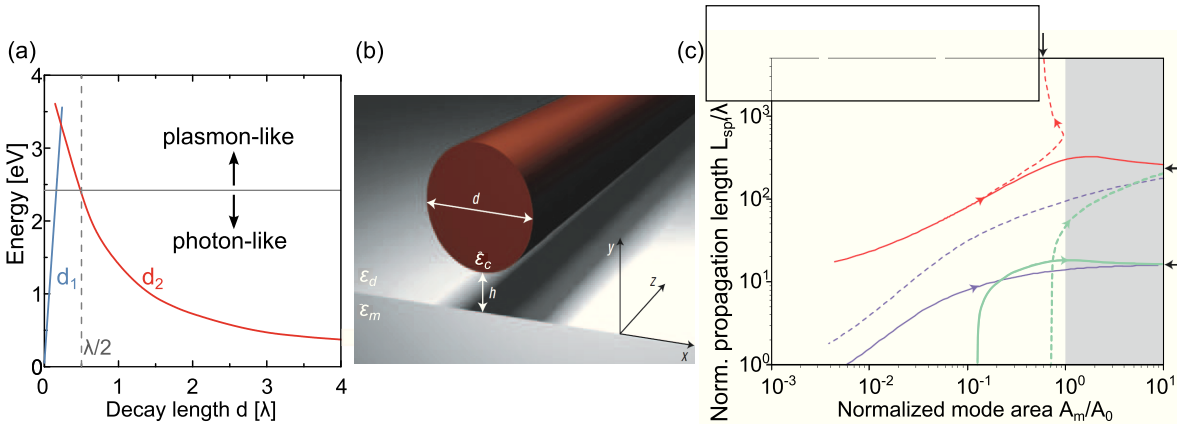

Figure 2.7: (a) The decay length ($\sim \frac{1}{e}$) of the electric field of a surface plasmon polariton in the metal (blue) and the dielectric (red), respectively. The diffraction limit is indicated by the vertical, dashed line. The curve is adopted from [118]. (b) Schematic of a semiconductor nanowire (ε_c) hybrid plasmonic waveguide on metal (ε_m) with spacer layer (dielectric ε_d) [122]. (c) Parametric plot of the normalized mode area vs. normalized propagation length for different plasmonic waveguide configurations: the hybrid plasmonic waveguide (red) is compared to dielectric-clad waveguides (blue lines) and silver-clad waveguides. The trajectories show a range of structural parameters: for the hybrid waveguide, $h = 1 \rightarrow 10^4$ nm for $d_1 = 200$ nm and $d_2 = 215$ nm. (These diameters indicate asymptotic solutions for $h \rightarrow \infty$, which are SPP-like and photon-like modes.) For the other geometries, the diameter is the varying parameter with $d = 10 \rightarrow 10^4$ [122].

The propagation length L_{sp} of a surface plasmon along the interface depends on the imaginary part of the propagation constant:

$$e^{-i\beta x} = e^{-i\beta' x} e^{\beta'' x} = e^{-i\beta' x} e^{x/2L_{sp}}. \tag{2.14}$$

The SPP propagation length is determined by the losses in the conducting material (ε_1'') and by the dielectric material ($L_{sp} \propto \varepsilon_2^{-3/2}$) [121]. From the dispersion relation, it is apparent that as $\omega \rightarrow \omega_{sp}$ the confinement increases and the propagation length decreases. Indeed, the SPP propagation length in the visible spectrum varies between 1 to 100 µm depending on the materials and geometry used. Thus, the trade-off between confinement and propagation distance is a fundamental challenge of plasmonics (and plasmonic waveguides).

2.2.4 Semiconductor nanowire hybrid plasmonic waveguides

Attenuation and loss compensation. Apparently, SPP waveguides are promising candidates for subwavelength optical confinement below the diffraction limit. However, SPP waveguides suffer from high losses and low propagation distances caused by the dissipative metal. Oulton et al. [122] proposed a hybrid optical waveguide consisting of a high refractive index semiconductor NW separated from the metal surface by a nanoscale dielectric gap, see figure 2.7b. The gap is essential in order to circumvent direct

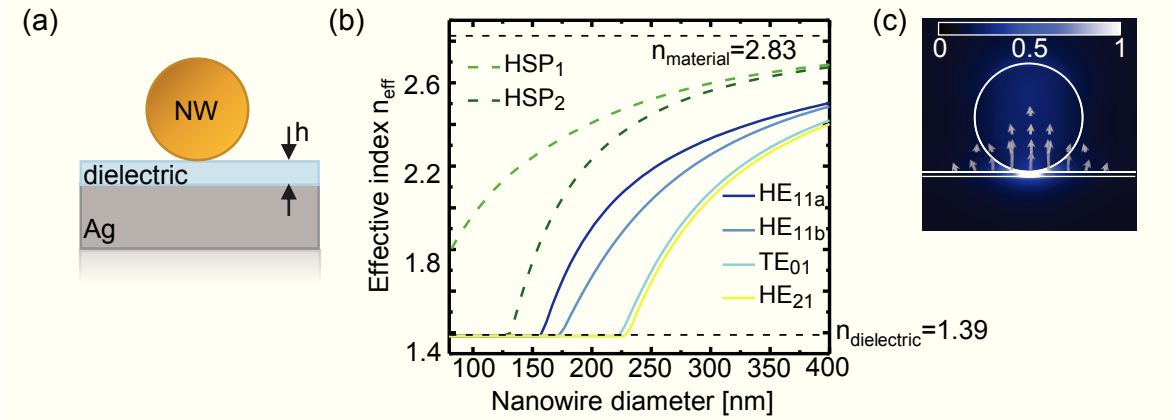

Figure 2.8: (a) Drawing of the nanowire (NW) hybrid plasmonic waveguide. (b) Effective mode index of the guided modes as a function of the nanowire diameter. The simulation parameters are taken for the case of a CdS NW (n = 2.83) on LiF/silver (h_{LiF} = 10 nm) interface. The simulated wavelength is 510 nm. The photonic modes (HE, TE modes) exhibit a cutoff, while the hybrid plasmonic mode (HSP_1) does not experience a cutoff. (c) Calculated electric field distribution of the HSP_1 mode.

contact of the semiconductor with the metal and it ensures a longer propagation length in combination with strong confinement of optical modes. This geometry is suited to support, not only photon-like modes, which was shown in section 2.1.6, but also SPP-like and especially hybrid plasmonic modes (see next paragraph). Control of the confinement and propagation length is gained by a variation of the gap height h. The red solid curve in figure 2.7c shows that for small diameters the mode area can be $\sim$ 100 times smaller than the diffraction limit, but that the mode still propagates more than 10 times the wavelength. Both mode area and propagation length increase for larger gap values as the mode becomes more photon-like. The hybrid waveguide obviously outperforms other comparable SPP waveguide configurations such as oxide and semiconductor clad silver nanowires (blue lines in figure 2.7c), and holes of insulator and semiconductor in silver (green lines) in terms of propagation length for comparable mode areas [122].

Semiconductor nanowire plasmonics. In addition to the long propagation length and strong optical confinement, which are both provided by the hybrid plasmonic waveguide, an optical gain medium, e.g. a semiconductor can be integrated. A semiconductor NW (see section 2.1.4) may provide enough optical gain to overcome the metal losses and even achieve stimulated emission and lasing at subwavelength scales [30, 123]. Similar to pure photonic NW lasers, the semiconductor NW hybrid plasmonic waveguide (through this thesis the term **plasmonic NW laser** is used) forms a Fabry-Pérot cavity [30, 124]. Figure 2.8a depicts the cross section of such a plasmonic NW laser. Besides the already introduced photonic modes (HE, TE, TM modes) two additional modes are supported. These two modes exhibit a hybrid-plasmonic character and they are labelled HSP_1 and HSP_2, respectively. The effective mode indices of several modes are shown in figure

2.8b for the case of a CdS NW plasmonic waveguide. The high index HSP_1 mode may propagate for all NW diameters, while all other modes experience a cutoff. Furthermore, the high mode index of the HSP_1 mode suggests strong mode confinement into the spacer layer between the metal and the nanowire, as shown in figure 2.8c. Mode areas smaller than $\sim$ 30 - 50 times the photonic mode area can be achieved for the hybrid modes using ZnO and CdS NWs [30, 118]. The HSP modes have strong electric field components along the NW axis, because of the transverse magnetic nature of surface plasmons [30]. Note, that the mode indices change depending on the material combination and considered wavelength [118]. However, because of the higher field confinement and high optical gain available in the semiconductor, the HSP modes are expected to be the lasing modes in plasmonic NW lasers [30].

Emission enhancement and Purcell effect. The large optical confinement in plasmonic NW lasers also affects light-matter interactions, which are generally determined by the Einstein coefficients for photon absorption B_{12}, the spontaneous emission rate A_{21} and the stimulated emission rate B_{21}. Taking carrier conservation ($\frac{dN_{total}}{dt} = 0$), thermal equilibrium conditions and a Boltzmann distributed two level system into account the following relation is derived:

$$A = \frac{\hbar\omega^2}{\pi^2 c^3} B, \text{ with } B_{12} = B_{21} = B. \tag{2.15}$$

Thus, the spontaneous emission rate and stimulated emission rate are fundamentally linked. Spontaneous emission, gain spectrum and (spontaneous) emission rates are fundamental properties of the semiconductor, which can hardly be modified. Instead, since both the cavity and the emitter are coupled to each other, a modification of the cavity design also tunes the spontaneous emission properties. This effect was first shown by Purcell by enhancing the spontaneous emission rate of atoms γ placed in a resonant cavity [125]. The enhancement factor (also referred to as Purcell factor) F is given by:

$$F = \frac{\gamma}{\gamma_a} = \frac{3}{4\pi^2} \frac{(\lambda/n)^3}{V_m} Q_{cav}. \tag{2.16}$$

Here, $\gamma_a \equiv A$ is the spontaneous emission rate of the uncoupled emitter, n is the refractive index, V_m is the volume of the cavity mode and Q_{cav} is the cavity quality factor. It is apparent that two approaches are open to enhance the emission rate γ. Either the quality factor Q_{cav} is increased or the mode volume V_m is reduced in size below the volume of the cavity photons $(\lambda/n)^3$. In photonic structures the first approach is applied and quality factors larger than $> 10^3$ are reached [9, 126, 127]. However, photonic structures are still limited by the diffraction limit. Alternatively, in plasmonic and hybrid plasmonic structures the mode volume V_m can be decreased far below the diffraction limit enabling high Purcell enhancements despite low quality factors. In this way, Purcell enhancement

factors of $\sim 6 - 50$ have been demonstrated for hybrid plasmonics using ZnO and CdS NWs on silver [30, 128].

Since the spontaneous emission is fundamentally linked to the stimulated emission (see equation 2.15), the stimulated emission rate is also enhanced, if the spontaneous emission rate exhibits Purcell enhancement. Indeed, this has been shown for photonic crystal cavities [9]. This enhancement of the emission rate is accompanied by an increase of the x_0 parameter, which determines the efficiency of spontaneous emission input into the laser resonator (introduced in section 2.1.4). Typically, hybrid plasmonic lasers reveal x_0 parameters of $\gtrsim 0.1$ [30, 129], while photonic NW lasers exhibit values of $x_0 \lesssim 0.05$ [23, 24, 115].

3 Methods

The methods used within this thesis are briefly summarized in order to mention the used parameters. Additionally to standard optical characterization using (micro) photoluminescence - (µ)PL, a recently developed 'double-pump' measurement technique was applied to investigate ultrafast temporal dynamics of single nanowires [118]. Furthermore, a novel 'head-on' microphotoluminescence setup was established during this thesis enabling a characterization of the far field emission of single semiconductor nanowires [39]. Both new techniques will be introduced in more detail.

3.1 Synthesis of semiconductor nanowires

Semiconductor NWs were grown using the vapor-liquid-solid (VLS) mechanism, which is a "bottom-up" approach introduced by Wagner and Ellis [130]. There's a variety of techniques available for NW growth, which provide the 'vapor' of material for the VLS mechanism. Furthermore, it has to be distinguished between self-catalyzed (also: homoparticle assisted) VLS growth (ZnO [131] and GaN NWs [132, 133]) and the heteroparticle assisted VLS approach requiring a metal catalyst deposited prior growth on the substrate (CdS [23] and ZnO NWs [134]). The source material for the NW growth accumulates in the catalyst droplet ('liquid' phase) and a steady material supply causes a concentration increase until supersaturation. Subsequently, the source material nucleates at the droplet-substrate interface as 'solid phase' resulting in the growth of a NW. The hetero seed metal catalyst is hardly soluble in the NW material, thus the catalyst droplet remains at the top (or more seldom at the bottom) of the NW. In contrast, there is usually no residual catalyst particle for the self-catalyzed VLS growth due to solidification of the droplet during the cooling of the sample [135, 136]. The NW diameter can be controlled to some extent by the size of the catalyst droplet and an epitaxial relation between NW and substrate causes a directed growth.

3.1.1 Vapor transport technique for II-VI semiconductors

Pure (unintentional doped) CdS and ZnO NW samples were grown by a vapor transport technique in a horizontal tube furnace. The source material (CdS powder or a mixture of ZnO and graphite powder with molar ratio 1 : 1) was evaporated at high temperatures of 800°C for CdS and 1050°C for ZnO, respectively. The vapor was transported by a carrier gas, either Ar for CdS NW or Ar + O_2 for ZnO NWs, towards the growth substrates, which were kept at lower temperatures. The growth substrate (Si chips) were coated with $5-10\,\text{nm}$ gold for the hetero seeded growth of CdS and ZnO NWs or with a 500 nm layer of Al doped ZnO (AZO) for the self-catalyzed growth of upstanding ZnO NWs, see figure 3.1a. Typical lengths and diameters for the II-VI semiconductor NWs used in this thesis

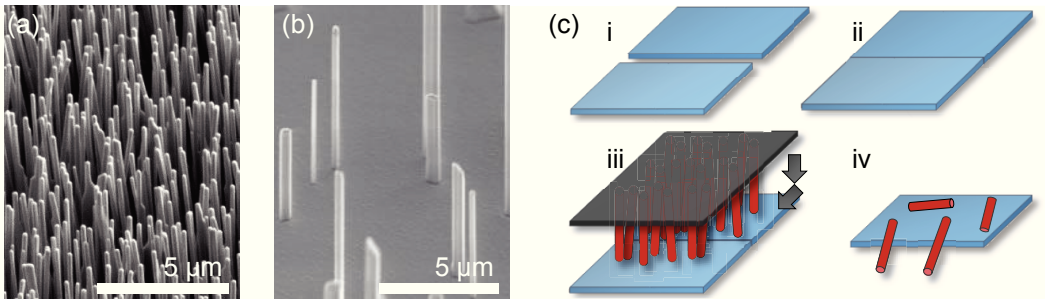

Figure 3.1: (a) Scanning electron microscopy (SEM) image of a ZnO NW sample grown on AZO using the vapor transport technique. (b) SEM image of GaN NWs grown on sapphire using MOVPE. (c) Schematic drawing of the modified imprint technique; using two substrate pieces with smooth edges and putting them together (i-ii), laying a NW sample on top and sliding perpendicular to the edge (iii), resulting sample (iv).

are L $\sim 5 - 30\,\mu$m and $\oslash \sim 100 - 500\,$nm. Further details on the growth of CdS NWs including a growth phase diagram can be found in [23, 137] and details for ZnO NWs are given in [134, 138].
Tin doped CdS (CdS:Sn) NW samples were synthesized by the group of Jia Grace Lu at the University of Southern California. Here, a mixture of CdS, SnO, SnO_2 and graphite powder with a molar ratio of 1 : 1 : 1 : 0.1 was used as source material and evaporated at 1000°C. The vapor was transported downstream by Ar carrier gas towards the Si growth substrates. Tin oxide was reduced to Sn by carbon during a previous heating step at 600°C forming the Sn hetero catalyst for the NW growth. Thus, Sn is incorporated into the wurtzite CdS NWs during growth [34].

3.1.2 Metal-organic vapor phase epitaxy - MOVPE

Gallium nitride NWs were synthesized by the group of Silke Christiansen at the Max Planck Institute for the Science of Light. The GaN NW samples, shown in figure 3.1b, were grown on c-plane sapphire in a horizontal flow metal-organic vapor phase epitaxy (MOVPE) reactor using trimethylgallium (TMGa), ammonia, silane as precursors and hydrogen as carrier gas. First, a thin buffer layer of AlN with N-polarity was deposited on the sapphire to support the NW growth. The self-catalyzed growth of GaN NWs was then carried out at a temperature of 1050°C, a pressure of 100 mbar and a V/III ratio between $6 - 25$. Note that silane strongly enhances vertical growth and causes n-type doping. The GaN NWs typically exhibit lengths $\lesssim 10\,\mu$m and diameters between $200 - 1000\,$nm. A more detailed study on the GaN NW growth is given in references [132, 133].

3.2 Sample fabrication - processing

For the optical experiments on single semiconductor NWs, some of them were transferred from the growth batch onto clean substrates by a dry imprint technique. Two NW laser

geometries, photonic NW and hybrid plasmonic NW lasers were introduced in chapter 2. **The photonic NW geometry** requires to place the NW on a low refractive index substrate in order to enable efficient waveguiding of the photonic mode. Thus, the NWs were imprinted onto Si substrates with a thermally grown 1.5 µm thick SiO_2 layer on top. In **the plasmonic NW geometry** the NWs were separated from a Ag substrate by a 10 nm thick LiF spacer layer. These substrates were fabricated by the group of Rupert Oulton at the Imperial College London. The fabrication process started with the thermal evaporation of a 100 nm thick Ag film on Si(100) substrates. Subsequently, the 10 nm thick LiF film was deposited on top. Both evaporation steps were carried out at room temperature in high vacuum at $\sim 10^{-6}$ mbar using deposition rates of 1.2 nm/s for Ag and 0.1 nm/s for LiF, respectively [118]. The hybrid plasmonic geometry requires a smooth film underneath the NW in order to minimize the plasmonic losses and ensure uniform field confinement [123]. Furthermore, the NW should lie flat on the surface. Therefore, scanning electron microscopy (SEM) and atomic force microscopy (AFM) measurements were performed on the combined Ag/LiF films. The film quality was sufficiently smooth and homogeneous for the purpose of this work with a surface roughness of $\sim$ 1.3 nm (RMS) over an area of $10 \times 10\,\mu m^2$ [118].

Samples for 'Head-On' measurement. After imprinting, semiconductor NWs usually lie completely on the substrate, which is sufficient to perform conventional microphotoluminescence (µPL) measurements. Unfortunately, this geometry prohibits the direct access to the emission out of the end facet without scattering from the substrate surface. In this thesis single NWs were deposited at the edge of the substrate partially suspended in air in order to enable detection of the light emitted from the loose end facet. This modified imprint technique is schematically depicted in figure 3.1c. Two substrate pieces with smooth edges were put together in order to form an even, flat surface. Subsequently, the NW growth batch was put on top and slowly slid perpendicular to the substrate edge. A sketch of the final sample (iv) is depicted in figure 3.1c.

3.3 Structural characterization

In chapter 2 it has been explained, how emission properties and optical performance, e.g. waveguiding and lasing, depend on the material composition, defect concentration and morphology. Therefore, several structural characterization methods were applied within this thesis, which are summarized in the following.

Scanning electron microscopy - SEM

The morphology of NWs was characterized by a high resolution SEM (FEI DualBeam Helios NanoLab 600i FIB system) equipped with a field emission electron gun. The system provides lateral resolutions of $\sim 1-2$ nm. The SEM images were usually acquired

using the secondary electron detection, which images well the NW morphology. Note, single NWs were usually imaged only after optical (photoluminescence) measurements in order to avoid any interaction or damage induced by the electron beam. Detailed information about the SEM can be found in references [139, 140].

Transmission electron microscopy - TEM

The crystalline structure of NWs was investigated by TEM (JEOL 2100F; University of Southern California) with sub-nm resolution. Here, the image is formed by detection of high energetic electrons, which are transmitted through the specimen undergoing scattering at the lattice atoms. Detailed information about this technique like the several imaging methods are given in reference [140].

X-ray diffraction analysis - XRD

The crystal structure of some NWs was characterized by XRD (Rigaku Ultima IV, University of Southern California), which is based on the constructive interference of X-rays being reflected at the crystal planes of the sample. This considerations result in Bragg's law. Reference [141] provides detailed information about Bragg's law and XRD.

Energy dispersive X-ray analysis - EDX

The stoichiometric composition of NWs was examined by means of EDX in a JEOL SEM equipped with a liquid nitrogen cooled Si EDX detector. High energetic electrons penetrate into the sample causing an ionization of the semiconductor atoms. Upper shell electrons then occupy the remaining vacancy and their excess energy dissipates as characteristic X-ray photon. Typically, the detection limit is $\sim 1\,\mathrm{at.\%}$.

3.4 Optical characterization

Luminescence arises from the recombination of charge carriers after an external excitation and is usually distinguished depending on the excitation source; cathodoluminescence relies on the excitation by energetic electrons, while photoluminescence requires photons for excitation etc. Using luminescence spectroscopy, materials can be examined in order to gain information about the radiative carrier recombinations, which were introduced in chapter 2.1.

3.4.1 Cathodoluminescence spectroscopy - CL

In CL spectroscopy, an electron beam excites the semiconductor material mainly due to inelastic interaction processes. This technique provides rather high spatial resolution, as it can be integrated in a SEM system. The electron-hole pair generation rate

G per incident electron depends on the electron beam energy E_{beam} and the band gap energy by $G \approx E_{beam}/2.8E_g$ [142]. Matching the penetration depth of the electron beam roughly with the dimension of the NWs requires $E_{beam} \sim 1$ - 10 keV. A parabolic mirror collects the luminescence light, which is then guided towards the detection system. Therefore, the light collection is global, which is disadvantageous in comparison to microphotoluminescence measurements. General reviews on CL measurements are given in references [142, 143]. The CL system used within this thesis, the Gatan MonoCL3+ in a JEOL SEM, is described explicitly in reference [137].

3.4.2 Photoluminescence spectroscopy - PL

Photoluminescence spectroscopy usually uses mono-energetic photons for the excitation, which are typically provided by a laser. As an advantage, the heat generation under photon excitation is less compared to the electron excitation used in CL, where much energy is dissipated via phonons. The scope of this thesis demanded the use of several optical measurement setups: 'Standard' (micro)PL spectroscopy was performed using a home-built setup, which was installed and established by S. Geburt [137]. Gaining further insights into the ultrafast lasing processes required the usage of a recently developed 'double-pump' approach introduced by T. Sidiropoulos [118], which exploits the nonlinearity of the laser process. Finally, a 'head-on' setup was installed within the frame of this thesis in order to image the laser light directed from the end facet of single NWs.

MacroPL setup

Figure 3.2a shows a scheme of the so called macroPL setup, which was applied for the characterization of either as-grown or as-imprinted NW ensembles, as the spot size of the excitation source on the sample is $\sim (500 \times 700)\,\mu m^2$. Thus, the measured signal superimposes the emission of at least $50 - 100$ single NWs depending on the coverage of the sample. The laser beam is directed towards the sample by mirrors and a prism and can be attenuated by seven orders of magnitude. The luminescence light is collected by spherical fused silica lenses and focused into a 500 mm monochromator (Princeton Instruments SP-2500i). The dispersed luminescence light is detected by a liquid nitrogen cooled, front illuminated CCD camera. Depending on the used grating the detection system reaches spectral resolutions between 0.05 nm for 1800 grooves/mm and 0.67 nm for 150 grooves/mm. The samples can be kept in a helium flow cryostat (Janis ST-500) enabling sample temperatures between $\sim 4 - 300$ K.

Time-resolved photoluminescence spectroscopy - TRPL

The TRPL measurements were performed by Marcel Wille and the group of Prof. Marius Grundmann at the University of Leipzig following the principle of Time-Correlated Single Photon Counting (TCSPS) [144]. The excitation is applied by a titanium sapphire (Ti:Sa)

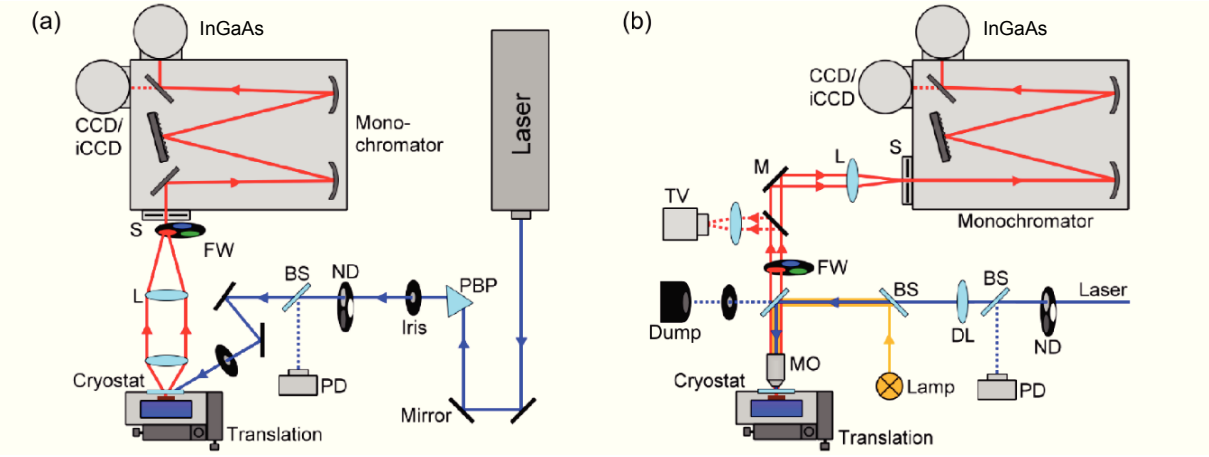

Figure 3.2: Schematic drawing of the macroPL and µPL setups, adopted from reference [137]. The laser beam is directed towards the sample by mirrors (M) and through a Pellin Broca prism (PBP). Neutral density (ND) filters attenuate the laser intensity, while on-line monitoring of the power is carried out using a beam splitter (BS) followed by a power diode (PD). (a) The luminescence from the sample mounted in the cryostat is collected by a lens (L) and focused onto the monochromator entrance slit (S) after passing through a set of long pass filters (FW). The spectrally dispersed light is detected by a CCD. (b) Here, the laser beam as well as white light is focused onto the sample by a microscope objective (MO). The MO collects the luminescence light, which is focused onto the monochromator slit after passing through FW. Microscopic images can be obtained by a TV camera.

laser, whose wavelength could be frequency doubled. The ~ 200 fs excitation pulses exhibit a wavelength of 437 nm at a repetition rate of 3.8 MHz. The laser is focused onto the sample down to $\sim 50 - 100\,\mu$m in diameter leading to intensities of $0.5 - 5\,\mathrm{W/cm^2}$. The luminescence light originating from the NW sample is dispersed by a monochromator (Horiba HR320) equipped with a 1200 grooves/mm grating and afterwards detected by micro-channel photomultiplier.

MicroPL (µPL) setup

The µPL setup schematically depicted in figure 3.2b was established as a supplement of the macroPL for the investigation of single NWs, which were dispersed onto clean substrates. The laser beam is focused onto the sample with small spot sizes of $\sim 1-30\,\mu\mathrm{m}^2$ (depending on the used objective) as well as white light for microscopic observation. Note that the laser spot is enlarged for lasing experiments by a defocusing lense (DL) to spot diameters of $\sim 20-30\,\mu$m. The luminescence light is collected by the same objective. The spectral detection system is similar to the macroPL and the cryostat is also available in the µPL setup. The installed TV camera enables furthermore microscopic brightfield and luminescence imaging. In general, the µPL setup allows spatial resolved detection, this means that the exact point of excitation and detection can be defined separately. Further technical details including lists of available excitation sources and optical components are given in reference [137].

Double-Pump measurement technique

Figure 3.3a shows the beam path of the double-pump setup to measure the temporal dynamics of single nanowire lasers. This setup is a supplement of a conventional µPL setup equivalent to the setup in 3.2b in order to generate two excitation pulses, which can be temporally delayed with respect to each other. The initial excitation of $\sim 150\,\mathrm{fs}$ pulses are generated in a titanium sapphire (Ti:Sa) laser followed by a second harmonic generation system. The repetition rate is adjusted by a pulse picker, such that significant heating and damage of the NW material is circumvented. The initial beam is splitted into a weak beam, which is referred to as pump 2, and a strong beam (pump 1). Then, the weak pump is delayed using a motorized translation stage providing a temporal resolution of $\sim 1.3\,\mathrm{fs}$ and a maximum delay of 167 ps. Subsequently, both beams are spatially

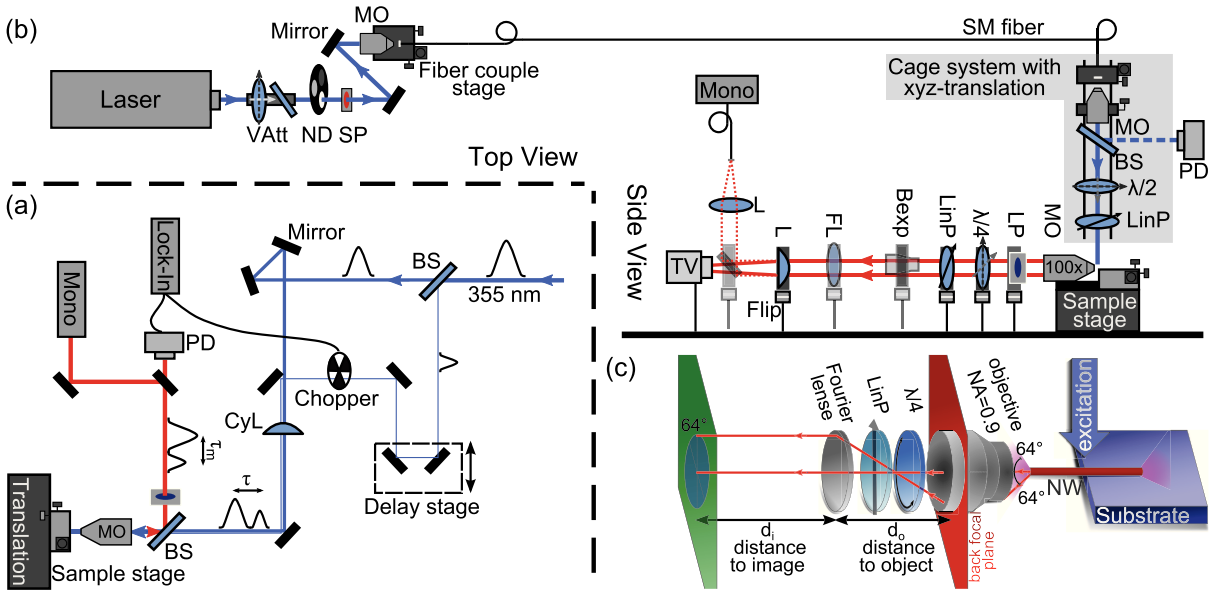

Figure 3.3: (a) Schematic drawing of the double-pump setup. The beam splitter BS sends $\sim 45\%$ of the laser beam through a delay line. The pump beam (pump 1) and the delayed beam (pump 2) are combined by a half mirror and focused onto the sample by a microscope objective (MO). The cylindrical lens (CyL) enlarges the excitation spot on the sample forming an ellipse. The double-pump response from the NW is collected by the same MO and then detected using either the monochromator or by modulating the delayed beam by a photodetector (PD) connected to a Lock-In amplifier. The scheme is adopted from reference [118]. (b) Sketch of the head-on measurement setup. The laser beam is coupled into a UV single mode (SM) fiber after passing through a variable attenuator (VAtt), a neutral density (ND) filter and a shortpass filter (SP; at 405 nm) in order to avoid unwanted wavelengths. The MO mounted in the movable cage system collimates the Gaussian-like laser beam and sends it through a $\lambda/2$ waveplate followed by a linear polarizer to adjust the polarization direction on the sample. The NW laser light is collected and detected by a mutually decoupled beam path, which is equipped with a high NA MO (NA = 0.9; 100x) and a longpass (LP) filter. The $\lambda/4$ waveplate and the linear polarizer (LinP) are applied to measure the polarization of the NW emission for all imaging/measurement configurations. The laser light is detected either in real space using the lens (L), spectrally using a mirror directing the light into the monochromator (see figure 3.2) or angular resolved using the Fourier lens (FL). (c) Highlighted scheme for the Fourier imaging.

recombined and focused onto the sample after passing a cylindrical lens (CyL) creating two overlapping elliptical excitation spots. The double-pump response of the NW is finally detected either in a spectrometer (Mono) or by modulating pump 2 with a chopper wheel in a photodiode (PD). Due to the usage of a Lock-In amplifier, the PD can measure the spectrally integrated temporal response with a better signal-to-noise ratio. The physics of the double-pump spectroscopy are going to be explained in chapter 5 and even more detailed in reference [118].

Head-On measurement setup

The direct investigation of the NW laser emission within this thesis demanded the installation of a new, so called 'head-on' setup, schematically drawn in figure 3.3b. For a spatially adjustable excitation, the laser beam is coupled into a single mode (SM) fiber, which additionally ensures a Gaussian excitation spot. A further microscope objective (MO) at the top of the 'xyz' movable cage system extracts the laser light from the fiber, which then goes through a waveplate ($\lambda/2$) and a linear polarizer (LinP). Thus, spot size, polarization and position on the fixed sample can be adjusted independently.
The mutually decoupled detection beam path is equipped with a high numeric aperture objective (Zeiss Epiplan Neofluar 100x, NA = 0.9) followed by several individually insertable optical components: The TV camera images the NW emission either in real space (lens L) or angular resolved in the Fourier space (lens FL), while spectral detection is obtained via coupling the light into a multimode fiber and sending it into the spectrometer of figure 3.2. All detection modi may benefit from a polarization analysis using the quarter waveplate ($\lambda/4$) in combination with the linear polarizer (LinP) [145]. The linear polarizer is fixed (at 0°), while the quarter waveplate needs to be rotated, such that the intensity is detected for at least eight equidistant angles (here 0°, 22.5°, 45°, 67.5°, 90°, 112.5°, 135°, 157.5°). The Stokes parameters are calculated from this data set of at least eight intensities. Figure 3.3c depicts the Fourier imaging microscopy with a maximum detection angle of 64°.
An evaluation algorithm for the polarization dependent Fourier images was established in the Master thesis of Max Riediger [41]. First, it subtracts the darkframe and scales each image with the pump laser intensity in order to correct the small laser deviations. Second, the image noise is reduced by the algorithm, as it applies a Gaussian filter followed by the calculation of the Stokes parameters S_0 - S_3 performed for each pixel. Finally, the algorithm converts the Fourier images obtained with the CCD into polar coordinates by the relation $\theta = \arcsin(\mathrm{NA} \cdot \mathrm{r}/\mathrm{r}_{\max})$, where r ($\mathrm{r}_{\max}$) is the in plane (maximum) distance from the center of the image. Certainly, the angular resolved images contain all relevant polarization information by means of S_0 - S_3 (compare chapter 2.1.5).

3.5 Simulations and modelling

Laser rate equations

It is widely accepted that gain formation in semiconductor nanowires occurs due to an EHP [21, 137, 146–148]. Although there are substantial differences between an atomic 3-(or 4-)level system and a real semiconductor laser, the qualitative coincidence of the atomic-like model and the experiment validates to use the model for the double-pump response. Photonic NW lasers, as described in chapter 2.1.6, typically generate laser emission in a spectral region where the unexcited semiconductor absorbs only very little, which makes it reasonable to model them as 4-level system. Whereas, the plasmonic NW laser emission usually overlaps more with the material absorption spectrum [31, 149] indicating a 3-level model as more appropriate. However, a 3-level laser model is used to model the double pump response of both, while the difference between photonic and plasmonic lasing is accounted by different transparency conditions. This ensures how close the model is to a 3- or 4- level laser system. The laser rate equations for the ground state E_1, the excited state E_2 and the upper laser level E_3 are given by

$$\frac{dN_2}{dt} = R\,(N_1 - N_2) - \frac{N_2}{\tau_{therm}}, \tag{3.1}$$

$$\frac{dN_3}{dt} = -\beta F A_0 s\,(N_3 - N_0) - F A_0 N_3 + \frac{N_2}{\tau_{therm}}, \tag{3.2}$$

$$\frac{ds}{dt} = \beta F A_0 s\,(N_3 - N_0) + F\beta A_0 N_3 - \gamma s. \tag{3.3}$$

In these rate equations, N_i refers to the population in the level E_i, N_0 defines the population at which transparency occurs, β is the spontaneous emission factor ($\sim x_0$), $A_0^{-1} = \tau_m$ is the spontaneous emission lifetime, which equals the exciton lifetime, F is the Purcell factor, R describes the pump rate, s is the photon cavity number, $\gamma^{-1} = \tau_{ph}$ is the photon cavity lifetime, and τ_{therm} defines the carrier thermalization time from E_2 to E_3. In the simulations, a Gaussian laser pulse of 250 fs initiates carrier excitation. Typical values for the simulation of the double pump response are $\beta_{ph} = 0.01$ and $F_{ph} = 1$ for the photonic NW and $\beta_{pl} = 0.2$ and $F_{pl} = 10$ for the plasmonic NW, respectively. In reference [118] reasonable values for the total carrier density $N_T = \sum_{1-3} N_i$ and the transparency point were estimated with $N_{T,ph} \sim 1 \times 10^8$ and $N_{0,ph} \sim 1 \times 10^6$ for the photonic ZnO NW and $N_{T,pl} \sim 1 \times 10^6$ and $N_{0,pl} \sim 1 \times 10^5$ for the plasmonic ZnO NW reproducing the experimental observations qualitatively quite well, although this simplified model hardly explains all processes in the highly excited semiconductor.

Finite-difference time-domain (FDTD) simulations

Gaining further insights into the photonic properties of the semiconductor nanostructures like absorption, scattering and light propagation in terms of modal properties required a

strict numerical modelling, which was performed by Robert Buschlinger from the group of Prof. Ulf Peschel at the Institute of Condensed Matter Theory and Solid State Optics, University of Jena. The electric field distributions of the light wave were calculated by solving the Maxwell's equations using FDTD codes of the commercially available software packages "Lumerical" or "Comsol". In FDTD simulations the three-dimensional NW morphology (diameter, length, shape of the cross section, substrate) is discretized and the respective material is modelled by its refractive index $\hat{n}(\lambda) = n(\lambda) + i \cdot k(\lambda)$.

Light-matter interaction - dynamical simulations

Conventional FDTD simulations neglect material dynamics in terms of temporal dependent carrier densities due to excitation, spontaneous and stimulated recombination, many-body effects in the semiconductor, carrier driven changes of the refractive index, etc. Certainly, modelling this strong light-matter interaction as function of time is urgent in order to describe the semiconductor NW lasing process in an accurate manner including EHP formation and evolution of gain. Therefore, the combined FDTD and semiconductor Bloch equation approach introduced by Buschlinger et al. [150] treats the material dynamics quantum mechanically, including many-body effects, in interaction with the electromagnetic wave(s) treated classically by means of FDTD. It is possible to describe the semiconductor NWs across the whole range of excitation conditions from the low excitation to the lasing regime without being limited to equilibrium distributions of carriers using this recently developed model [150]. Thus, it is of special interest for the qualitative and quantitative comparison with the experimental results obtained within this thesis.

4 Continuous wave lasing of tin doped CdS nanowires

This chapter highlights the structural and optical properties of tin doped CdS nanowires (CdS:Sn NW) towards the achievement of continuous wave (cw) laser emission from a single NW. The synthesis of the CdS:Sn NWs was performed by Mengyao Zhang and Prof. Jia Grace Lu from the University of Southern California. The optical experiments were carried out in collaboration with Marcel Wille (see his master's thesis [36]). Parts of this chapter are published in references [34] and [35].

4.1 Motivation

As functional photonic devices, NWs provide highly localized emission and mark the lower physical size limit of laser systems based on pure photonic modes [23,115]. However, NW lasing has been obtained so far only in pulsed mode operation [21,22,24], but an available nanoscaled continuous wave (cw) laser source may improve integration into all-optical devices. Nanowire lasing via optical carrier injection usually requires pulsed excitation. Thus, the high pumping power induces population inversion causing optical gain and light amplification, while the introduced thermal budget can dissipate during the off times to the substrate. This prevents a substantial material degradation. Managing the thermal budget seems to be the key challenge, which can be overcome by both choosing a high optical gain material with low Mott density and using NWs with nearly perfect resonator structure. Therefore, high quality CdS NWs were fabricated by an optimized growth route circumventing the pretreatment of the growth substrate with catalyst deposition. This technique (see chapter 3.1.1) however uses Sn as catalyst, which is incorporated into CdS material during the growth. Thus, the structural and morphological properties of the Sn doped CdS NWs must be investigated. In literature, it has been reported that group IV elements such as Sn cause compensation effects in II-VI semiconductors [151]. Therefore, the doping levels need to be determined by means of luminescence spectroscopy in order evaluate whether these NWs are really suitable as functional unit for electronics and photonics. Finally, lasing experiments need to show that the CdS:Sn NWs can sustain high cw excitation conditions in order to induce cw laser emission from a single CdS:Sn NW.

4.2 Structure and morphology

The growth substrate was covered with a yellow-grayish layer of nanostructures after synthesis using the vapor transport technique [34]. Figure 4.1a shows a scanning electron microscopy (SEM) image of a typical CdS:Sn NW ensemble with its hierarchical dendrite

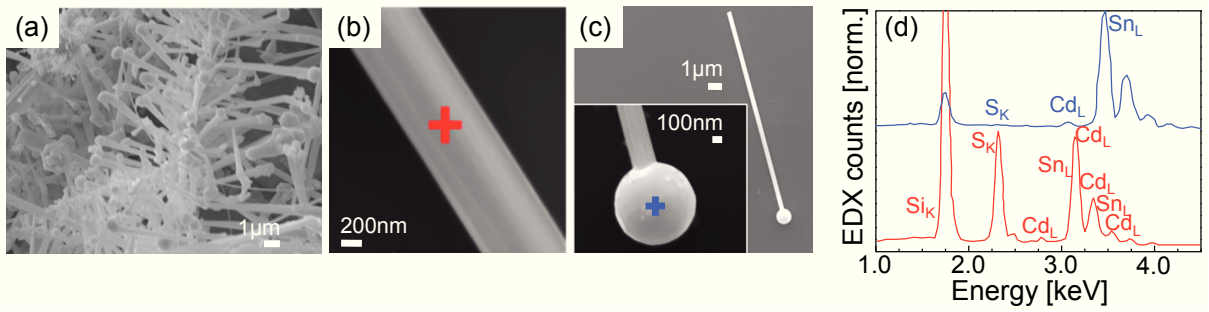

Figure 4.1: (a) Scanning electron microscopy (SEM) image of a typical CdS:Sn nanostructure ensemble after synthesis showing a hierarchical structure. (b,c) The SEM images of single CdS:Sn NWs on Si substrate in order to enable EDX point analysis. (d) The EDX spectra obtained from the marked spots in (b,c).

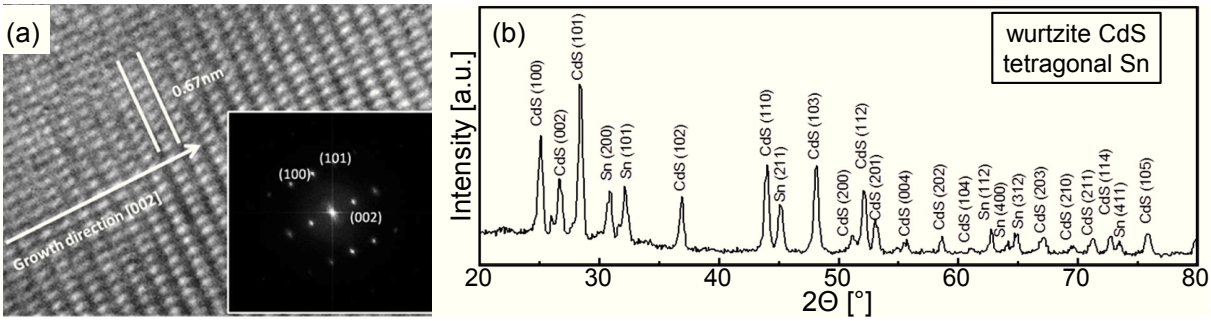

Figure 4.2: (a) High-resolution TEM image of an exemplary CdS:Sn NW ($\sim 100\,\text{nm}$ diameter) shows the single crystalline wurtzite structure. The NWs grow typically along the c-axis and indicate no extended crystal defects and nearly no stress/strain. (b) The X-ray diffraction spectrum obtained from the as-grown CdS:Sn NW ensemble reveals that all NWs grow in wurtzite structure and the remaining Sn catalyst at the NW tip is present in tetragonal crystal structure.

structure. Single NWs were transferred onto clean Si substrates to perform morphological and stoichiometric investigations on them. Most of the NWs exhibit a straight homogeneous morphology with diameters between $\sim 100\,\text{nm}$ and $1\,\mu\text{m}$, while some of them show a strong taper. As NWs with homogeneous diameters of $\gtrsim 200\,\text{nm}$ are the most promising for lasing experiments, this chapter refers only to straight specimen, as shown in figure 4.1b,c. Some of the transferred NWs kept the residual catalyst particle at the top. The stoichiometric composition of single NWs and the remaining tip particle was analyzed by means of EDX, as depicted in figure 4.1d for the NW from 4.1b (red) and the tip particle from 4.1c (blue). This particular NW contains the elements Cd/S/Sn in a stoichiometric ratio of $\sim 50.2 : 48.1 : 1.7$. According to the EDX analysis on ten different CdS NWs, the Sn incorporation is in average $\sim 1 - 4\,\text{at.}\%$ and Sn is spread uniformly along the NW, see supporting information (SI) in [34], while the spherical particle at the NW tip contains predominantly Sn with an amount of $\gtrsim 98\,\text{at.}\%$. Most of the straight NWs show hexagonal cross sections, which is typical for single crystalline wurtzite NWs. Moreover, the high-resolution TEM image and the corresponding fast Fourier transform (FFT) pattern in figure 4.2a clearly reveal that the CdS:Sn NWs grow along the c-axis of

the anisotropic hexagonal wurtzite crystal. The perfectly single crystalline structure does not contain any visible extended defects, dislocations or different crystal phases. Although rather high amounts of Sn were incorporated into the CdS matrix, the lattice parameters $a = 0.41\,\text{nm}$ and $c = 0.67\,\text{nm}$ of the doped CdS remain nearly unchanged in comparison with the parameters of pure bulk CdS indicating that the doped NW lattice is not significantly distorted. Thus, the CdS:Sn NWs are expected to exhibit similar high optical quality and gain values as unintentional doped CdS NWs. The XRD signal obtained from the as-grown NW ensemble (figure 4.2b) can be assigned either to the hexagonal structure of the CdS NWs or to the tetragonal Sn crystal phase of the remaining catalyst. Therefore, the ensemble only consists of wurtzite NWs and no other crystal phases occur for the CdS NWs due to the Sn doping. An extended explanation of the growth process leading to the hierarchical structure and the tapering is given in reference [34].

4.3 Amphoteric nature of Sn in CdS nanowires

The structural and morphological investigations so far have shown that $\sim 1-4\,\text{at.}\%$ of Sn is homogeneously incorporated into the CdS NWs and does not alter the CdS crystal structure significantly. Group IV elements such as Sn typically show amphoteric behaviour in II-VI semiconductors [151]. Because the ionic radius of Sn^{2+} with 1.18 Å is close to that of Cd^{2+} with 0.95 Å [152], a preferential occupation of the Cd lattice site might cause a dominating n-type doping in the CdS:Sn NWs. Hence, the doping levels of the CdS:Sn NWs needs to be determined by means of luminescence experiments in order to gain insights whether Sn is indeed incorporated amphoterically and causes compensation in CdS.

4.3.1 Low temperature luminescence in low excitation regime

Figure 4.3a shows the SEM image of a typical CdS:Sn NW ensemble, which was first investigated by overview cathodoluminscence at 7 K. The CL spectrum of these nanostructures in figure 4.3b reveals three characteristic emission bands: The deep level emission (DLE) around $\sim 2.1\,\text{eV}$ is attributed to intrinsic defects such as carrier recombinations at Cd interstitials (Cd_I), as it similarly occurs in unintentional doped CdS crystals [78]. The near band edge emission (NBE) between $\sim 2.5-2.6\,\text{eV}$ is caused by recombinations of free (FX) and bound excitons (I-lines) accompanied by their phonon replica. This NBE is also known for undoped CdS NWs [137], while in the spectral region between $\sim 2.25-2.45\,\text{eV}$ emission features occur, which are absent in undoped CdS NWs. These emission features are therefore most likely caused by the Sn incorporation and can be assigned to donor-acceptor-pair (DAP) and one free to bound (e,A) transition, as PL analysis will show later. Thus, Sn seems to cause both donor and acceptor levels in CdS. The DAP and (e,A) transitions are furthermore accompanied by their intense phonon replica. The DAP emerges from an electron bound to a donor recombining with a hole bound to an

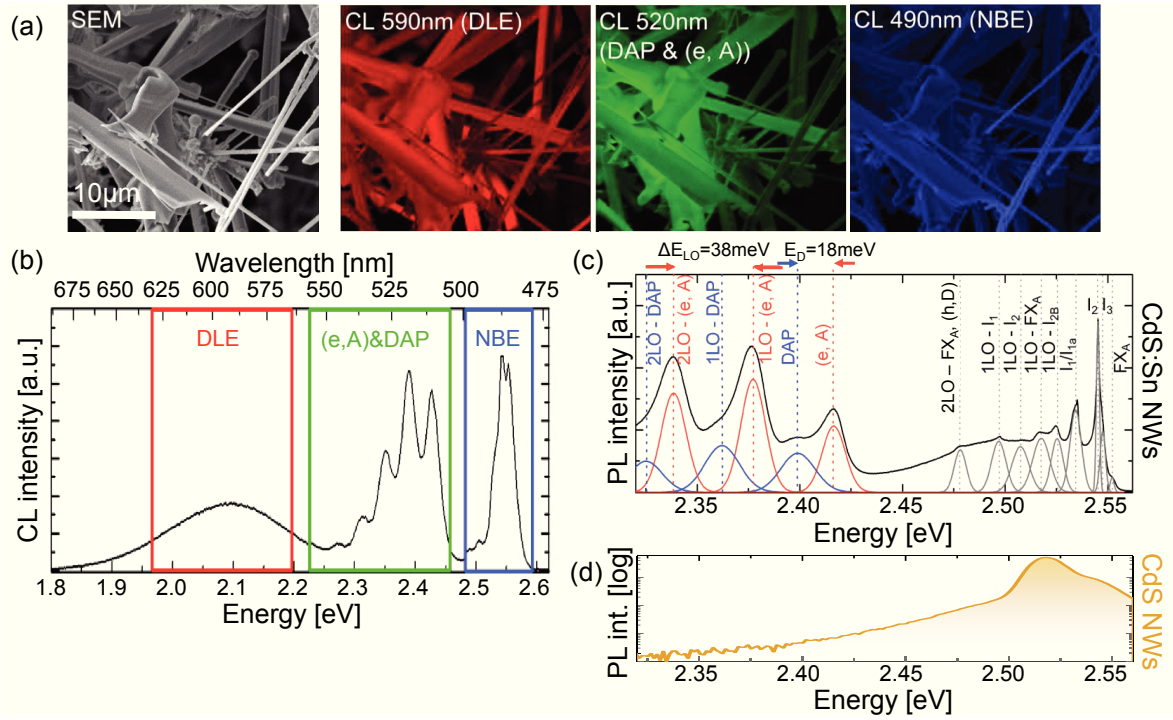

Figure 4.3: (a) Exemplary SEM and monochromatic CL images of a CdS:Sn nanostructure ensemble at 7 K. The NBE at ∼ 490 nm (∼ 2.53 eV) arises mainly from the long and straight NWs, whereas the thick microstructures predominantly emit luminescence at ∼ 520 nm (∼ 2.38 eV) attributed to DAP and (e,A) transitions. Deep level emission (DLE) is obtained from the whole ensemble. (b) Low temperature (7 K) CL spectrum of the respective CdS:Sn NW ensemble in (a) shows the three characteristic emission regions: NBE (blue), DAP and (e,A) transitions accompanied by phonon replica (green) and DLE (red). (c) Low temperature (4 K) PL spectrum of the as-grown CdS:Sn NW ensemble, taken at $\lambda_{exc} = 325$ nm, $I_{exc} = 50\,mW/cm^2$. The transitions are labelled according to their origin as free excitons (FX_A), donor bound excitons (I_2, I_3), acceptor bound excitons (I_1, I_{1a}) and surface excitons (SX) with their respective LO phonon replica ($E_{LO} = 38$ meV). The energetic distance between (e,A) and DAP corresponds to $E_D = 18$ meV. (d) The low temperature PL spectrum (4 K) of an undoped CdS NW ensemble grown without Sn as a catalyst does not show any DAP or (e,A) transitions. The PL spectrum of the undoped CdS NWs is dominated by the first phonon replica of the free exciton (1LO-FX_A) due to the low density of shallow doping levels. Thus, the PL emission appears spectrally broad.

acceptor, while the (e,A) transition is the emission feature of a free electron that recombines with an acceptor bound hole. Consequently, the energetic difference between (e,A) and DAP corresponds approximately to the binding energy of an electron to a donor: $E_D \approx E_{(e,A)} - E_{(DAP)}$. The origins of the luminescence features were further investigated by acquiring the monochromatic CL images in figure 4.3a. The images show that the NBE at ∼490 nm arises mainly from the long and straight NWs. The weak DLE compared to the intense NBE in these thin NWs indicate the high optical quality of thin NWs. Instead, the thicker structures exhibit predominantly luminescence at ∼ 520 nm attributed to the DAP and (e,A) transitions. This results suggest that a larger amount of Sn is incorporated into thicker structures than in the desirable thin and straight NWs. Therefore, thin NWs exhibit a lower donor and acceptor density than thick microstructures.

The low temperature PL measurement (T = 4 K, λ_{exc} = 325 nm, I_{exc} = 50 mW/cm^2) on the as-grown CdS:Sn NW ensemble allows high spectral resolution investigation of the NBE, DAP and (e,A) transitions, as depicted in figure 4.3c. The DAP and (e,A) transitions are indeed absent for undoped CdS NWs which were grown without using Sn as catalyst, compare figure 4.3d. The DAP as well as the (e,A) transition of the CdS:Sn NWs reveal strong phonon replica with a distinct spectral spacing of 38 meV corresponding to the energy of a longitudinal optical (LO) phonon in CdS. Obviously, the material exhibits a strong electron-phonon coupling, because several phonon replica occur with a first phonon replica even more intense than the zero phonon line (ZPL) [36]. From the energetic distance between the DAP at 2.399 eV and the (e,A) at 2.417 eV, the electron donor binding energy can be estimated to be $E_D \approx 18 \pm 1$ meV. Note, that a large r_{AD} distance between donor and acceptor r_{AD} was assumed due to low excitation intensities. In addition, the PL spectrum reveals a strongly featured NBE, whose recombinations are assigned according to the literature [42, 72]: The free exciton emission FX_A occurs at $\sim$ 2.552 eV, accompanied by excitons bound to ionized donors at $\sim$ 2.548 eV (DX, labeled I_3). The emission feature at $\sim$ 2.545 eV is attributed to surface excitons (SX) and excitons bound to neutral donors (D^0X, I_2). The emission features labelled I_1 (2.535 eV)and I_{1a} (2.533 eV) are caused by neutral acceptor-bound excitons and their acoustic phonon replica [153]. The following five emission features at the low energy side correspond to LO phonon replicas of the B-exciton bound to a neutral donor I_{2B}, the FX_A, I_2 and I_1, respectively. In reference [72], the emission feature at $\sim$ 2.477 eV is attributed to a (h,D) recombination of a free hole with a donor-bound electron. The deep donor level is caused by a sulphur vacancy (V_S).

4.3.2 Temperature dependent photoluminescence

Figure 4.4a shows overview PL spectra for an increasing temperature from 4 K to 120 K of a CdS:Sn NW ensemble. The three characteristic emission bands are again highlighted using the same colours as in figure 4.3a,b. In general, the DLE intensity increases relatively to NBE, DAP and (e,A) transitions with increasing temperature. The charge carriers are more mobile at elevated temperatures and dissociate from shallow defect levels, thus localization at deeper defect levels such as Cd_I is more favorable. Furthermore, the NBE luminescence vanishes much faster with increasing temperatures in comparison to the DAP and (e,A) transitions, as the excitons bind less strongly to the shallow defect levels.

Figure 4.4b shows high resolution spectra of the NBE for temperatures between 4 K and 60 K. The bound excitons dissociate from the shallow donors and acceptors between 45 K and 60 K, while the FX emission starts to dominate the NBE spectra at these temperatures. Furthermore, an increasing temperature causes a decreasing semiconductor band gap $E_g(T)$, which is empirically described by the Varshni formula [154]. Consequently, the emission energies of the NBE, DAP and (e,A) transitions also decrease. Since the

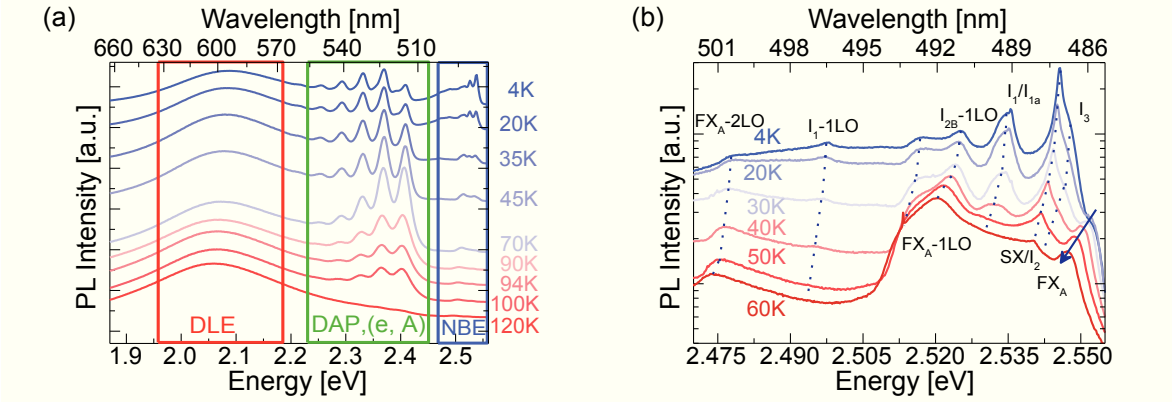

Figure 4.4: (a) Overview PL spectra of the as-grown CdS:Sn NW ensemble from 4 K to 120 K. The PL spectra contain the excitonic NBE (blue), the DAP, as well as the (e,A) transition (green) and the DLE (red). (b) High resolution PL spectra of the NBE in logarithmic scale between 4 K and 60 K. The red-shift of the emission features, which occurs due to the temperature increase, is indicated by the dashed lines.

NBE originates from excitons, whereas the DAP and (e,A) emerge from free and trapped carriers, respectively, these transitions can be distinguished by their energy red-shift as a function of temperature. The red-shifts of bound and free excitons are indicated as dashed lines in figure 4.4b. The obtained energy shift of the FX_A as function of temperature, shown in figure 4.5a (blue), coincides well with reports in literature for undoped CdS single crystals [44]. In addition, figure 4.5a shows the emission energy of the (e,A) transition as a function of the temperature (green), which clearly exhibits a different dependence. Thus, NBE and (e,A) unambiguously have different origins, as the free to bound (e,A) transition shifts less than the NBE. The temperature dependent energy difference:

$$E_{FX} - E_{(e,A)} = E_g - E_B^{FX} - \left(E_g - E_A + \frac{1}{2}k_BT\right) = -E_B^{FX} + E_A - \frac{1}{2}k_BT, \tag{4.1}$$

with the acceptor binding energy at 0 K, E_A, reveals that the (e,A) transition involves a free electron. The kinetic energy of the free electron increases linearly with the temperature ($k_BT/2$), compare black data in figure 4.5a, as expected for a free to bound transition [155, 156]. The acceptor binding energy $E_A \sim 164$ meV can be obtained from the y-axis intersect of the black fit by: $E_A \sim 136\ \text{meV} + E_B^{FX}$.

The (e,A) transition is more intense than the DAP emission, as depicted in figure 4.3c. At temperatures above $\sim$ 15 K the DAP emission feature can hardly be distinguished from the dominating (e,A) transition. Thus, the investigation of the temperature dependence of the DAP is not possible. Note that according to equation 2.2, the temperature dependent red-shift of the DAP emission E_{DAP} should be dominated by the decreasing band gap energy E_g and the temperature dependent donor-acceptor distance r_{AD}, because the carriers are localized at the shallow traps.

Figure 4.5b shows the integrated PL intensities of the excitonic NBE (blue) and the combined DAP and (e,A) emission (green) (including the phonon replica) in logarithmic scale

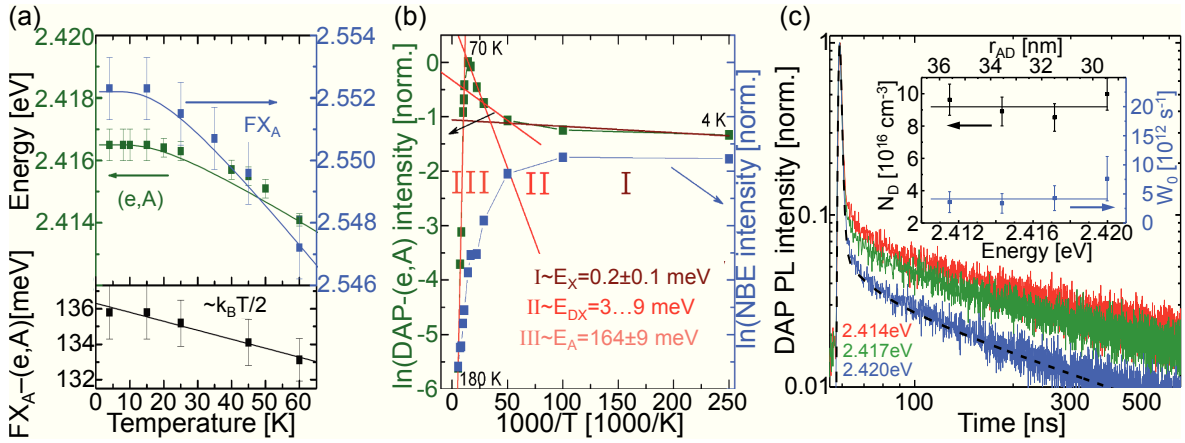

Figure 4.5: (a) Temperature dependent red-shift of the FX (blue) and the (e,A) transition (green) fitted with the modified Varshni relation from reference [157]. The energetic difference $E_{FX} - E_{(e,A)}$ (black) is proportional to the thermal energy, which is indicative of a free to bound transition. (b) Logarithmic PL intensity of the (e,A) transition (green) and the NBE (blue), respectively, as a function of the inverse temperature. The graph exhibits three different regimes (I-III), each with an activation energy for the different carriers contributing to the (e,A) emission. (c) The normalized transient DAP decay at three different DAP transition energies in a double logarithmic plot shows that closer DAPs undergo faster radiative recombination rates. The DAP transient at 2.420 eV is fitted (black dashed curve) with the DAP model of reference [158]. The inset depicts the fitting parameters: donor concentration N_D and transition rate W_0 versus the DAP transition energy.

as function of inverse temperature. The data were obtained from figure 4.4a. The graph is subdivided into three characteristic temperature regimes (I-III), each with a distinct temperature dependence of $I \sim \exp(-E_{act}/2k_BT)$. Thus, relevant dissociation processes and their respective activation energies can be determined. The temperature regime (I) between $\sim 4 - 45\,K$ is governed by a slight decrease of the NBE intensity, while the DAP-(e,A) intensity increases accordingly. Some of the bound excitons already dissociate at these temperatures into free excitons. They can decay due to their limited lifetime, leading to an increased amount of electrons and holes, which recombine subsequently via DAP and (e,A) transitions. The activation energy for this processes E_X is in the range of sub-meV. In the second temperature regime (II) between $\sim 45 - 70\,K$, almost all bound excitons dissociate from their trap causing a pronounced decrease of the NBE intensity. This is accompanied by an increasing DAP and (e,A) emission, which exhibits a slope of $E_{DX} \sim 3 \ldots 9$ meV. The value of E_{DX} matches the binding energy of excitons to neutral/ionized donors (I_3/I_2), because they contribute most to the NBE (compare figures 4.3c and 4.4b). The third temperature regime (III) between $\sim 80 - 180\,K$ shows a strong decrease of the DAP-(e,A) emission intensity of approximately five orders of magnitude. The activation energy $E_A = 164 \pm 9$ meV corresponds to the binding energy of a hole to an acceptor, which has been determined in figure 4.5a. In summary, the dominant donor bound excitons dissociate from the shallow trap mainly between $45 - 70\,K$, while bound holes dissociate from the acceptor between $80 - 180\,K$.

4.3.3 Time-resolved photoluminescence of the DAP

In the investigations of the CdS:Sn NWs so far, the emission feature at $\sim 2.399\,\mathrm{eV}$ was assumed to arise from a DAP transition. Proving the DAP nature requires time-resolved PL measurements, which were performed on an as-imprinted ensemble of NWs at 2 K. The sample contained mainly long and straight NWs, thus the (e,A) and the DAP emission are less intense than in the as-grown ensemble shown in figure 4.3a. Additionally, both emission features are spectrally well separated, for this sample (not shown). Figure 4.5c shows normalized PL transients of the DAP emission at three different energetic positions of the zero phonon line. The DAP transitions decay over few hundreds of ns, whereas the excitonic NBE typically decays much faster with lifetimes of hundreds of ps [159, 160]. The highest DAP emission energy is marked in blue, whereas the lowest energy is shown in red. Closer donor-acceptor pairs reveal according to equation 2.2 higher emission energies and undergo faster radiative recombination rates, as the electron and hole wave functions overlap more than in DAPs of larger distance. Figure 4.5c indicates exactly this trend proving that this emission feature is indeed caused by a DAP transition. Furthermore, the DAP dynamics can be analyzed applying a model introduced by Thomas et al. [158, 161]. The transient DAP decays were fitted (e.g. black dashed line in figure 4.5c) using the equation [158, 162]:

$$\mathrm{I_E}\left(\mathrm{t}\right) = \mathrm{W}\left(\mathrm{r_{AD}}\right) \cdot \exp\left(-\mathrm{W}\left(\mathrm{r_{AD}} \cdot \mathrm{t}\right)\right) \left\langle \mathrm{Q}\left(\mathrm{t}\right)\right\rangle, \text{with} \tag{4.2}$$

$$\left\langle \mathrm{Q}\left(\mathrm{t}\right)\right\rangle = \exp\left[4\pi \mathrm{N_D} \int_0^\infty \left(\exp\left(-\mathrm{W}\left(\mathrm{r}\right)\mathrm{t}\right) - 1\right) \mathrm{r}^2 \mathrm{dr}\right]. \tag{4.3}$$

Here, $\mathrm{W(r_{AD})} \approx \mathrm{W_0} \cdot \exp\left(-2\mathrm{r_{AD}}/\mathrm{a_{B,D}}\right)$ is the transition rate of the DAP, $\mathrm{a_{B,D}}$ is the Bohr radius of the electron at the donor, $\left\langle \mathrm{Q}\left(\mathrm{t}\right)\right\rangle$ denotes the occupation probability at time t taking into account randomly located acceptors. For the fitting of the DAP transients, $\mathrm{r_{AD}}$ was kept fixed according to equation 2.2, as the DAP transition energy, $\mathrm{E_g}$, $\mathrm{E_D}$ and $\mathrm{E_A}$ are known. The Bohr radius was set to $\mathrm{a_{B,D}} = 2.5\,\mathrm{nm}$ [153], while the donor concentration $\mathrm{N_D}$ and the transition rate $\mathrm{W_0}$ were varied. The inset of figure 4.5c shows the results of the fitting for four DAP transients at different energies and the corresponding donor-acceptor distances $\mathrm{r_{AD}}$, respectively. Both parameters, $\mathrm{N_D}$ and $\mathrm{W_0}$, are consistently almost constant for the evaluated DAP transition energies. Thus, a donor concentration of $\mathrm{N_D} = (9.2 \pm 0.4) \cdot 10^{16}\mathrm{cm}^{-3}$ can be estimated for the thin and straight CdS:Sn NWs.

4.3.4 Power dependent photoluminescence of single NWs.

The results obtained so far present the superposition of properties for a high amount of NWs. The properties of single NWs are accessible by applying µPL measurements. Optically excited single NWs exhibit luminescence from the position of excitation as well as slightly weaker out coupled emission from the NW cavity at the end facets due to

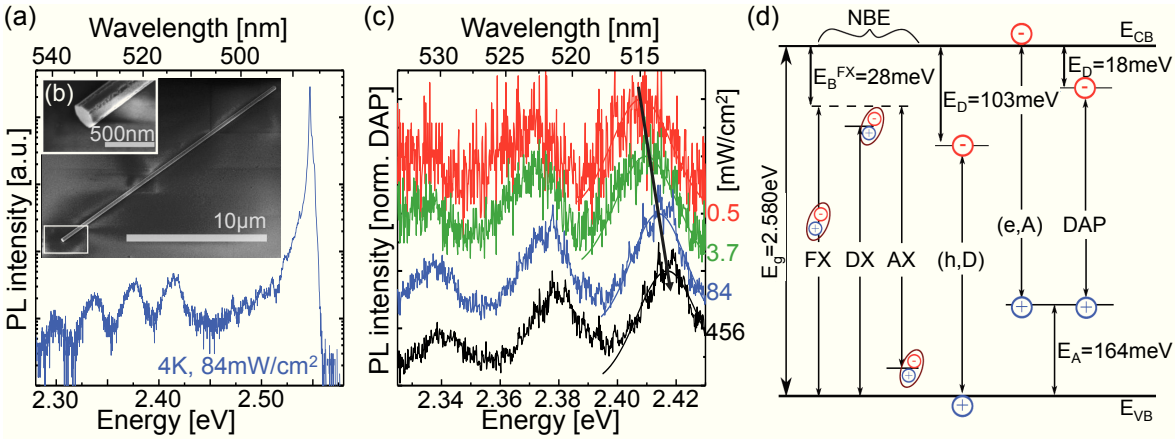

Figure 4.6: (a) Low temperature (4 K) µPL spectrum of the single CdS:Sn NW shown in (b). The spectrum (detected at the excitation spot) exhibits an intense NBE ($\sim 2.47 - 2.58$ eV) as well as the DAP transition accompanied by its phonon replica ($\sim 2.25 - 2.43$ eV). (b) SEM image of the respective NW (diameter ~ 300 nm, length 19.9 µm) with smooth end facets on SiO_2/Si substrate. (c) Power dependent µPL spectra (T = 4 K) indicating the blue-shift of the DAP from low (red; 0.5 mW/cm^2) to moderate excitation intensities (black; 456 mW/cm^2), as depicted by the arrow. (d) Schematic energy levels of Sn doped CdS NWs with excitonic NBE transitions (FX, DX, AX), DAP transition and both free to bound transitions (e,A) and (h,D). The DLE transitions are not shown here.

waveguiding [20]. Figure 4.6a shows the low temperature (4 K) µPL spectrum from the excitation spot of the CdS:Sn NW depicted in figure 4.6b. This particular NW reveals an excellent optical quality with an intense NBE and almost negligible DLE (not shown here). Its NBE is dominated by donor bound excitons I_3 and I_2 [35] indicating the predominant n-type doping of this single NW. In addition, the spectrum shows the emission features between 2.3 eV and 2.4 eV, which were attributed to the DAP transition and its phonon replica in the previous chapter. The DAP emission intensity of the thin NW is almost three orders of magnitude weaker than the NBE intensity, which is in good agreement with the observations from the monochromatic CL images (figure 4.3a). Power dependent emission spectra at T = 4 K are depicted in figure 4.6c. These µPL spectra reveal a clear blue-shift of ~ 10 meV, when the excitation intensity is increased ~ 900 times. This blue-shift appears because the mean distance $\bar{r}_{AD}$ of involved donor-acceptor pairs decreases with increasing carrier concentration induced by higher excitation intensities.

4.3.5 Compensation effects and doping levels

Summarizing the results of the optical spectroscopy leads to the schematic band diagram in figure 4.6d. The band gap of the CdS:Sn NWs at 4 K was determined as $E_g \sim 2.580$ eV, because the FX occurs at ~ 2.552 eV and $E_g = E_{FX} + E_B^{FX}$, with $E_B^{FX} = 28$ meV. The thin CdS:Sn NWs exhibit predominantly n-type behaviour similar to undoped CdS NWs, as indicated by the intense donor bound excitons. In addition, Sn doping in CdS seems also to create acceptor levels, because acceptor bound excitons ($I_{1(a)}$), (e,A) and DAP

transition occur, which are usually not observed for undoped CdS NWs [137]. The free to bound nature of the (e,A) transition and the acceptor level at $E_A \sim 164\,\text{meV}$ were examined by temperature dependent PL studies. Time-resolved PL unraveled the DAP transition and the donor level was determined by $E_{(e,A)} - E_{DAP} = E_D \sim 18$ meV. An additional, deeper donor level appears at $\sim 110\,\text{meV}$ due to sulphur vacancies (V_S) and causes the (h,D) transition. The donor concentration could be estimated as $N_D \sim 9.2 \cdot 10^{16}\text{cm}^{-3}$ by evaluating the DAP decay dynamics in detail.
Furthermore, electrical characterization of single CdS:Sn NWs were carried out in back gate field-effect transistor (FET) configuration [34]. The results show n-type behaviour of the CdS:Sn NWs, which is consistent with the PL/CL measurements. The conductivity of the CdS:Sn NWs is approximately 4 - 5 times higher than in undoped CdS NWs, but the carrier mobility in several investigated NWs ($\mu_e = 0.12 \ldots 2.64\ \text{cm}^2/\text{Vs}$) is considerably smaller than that of bulk CdS ($\sim 350\,\text{cm}^2/\text{Vs}$ [163]) and doped CdS:Ga NWs [164]. In addition, the free carrier density of $\ll 8 \cdot 10^{16}\text{cm}^{-3}$ in the exhaustion region of the semiconductor, when all extrinsic donors are ionized, is much less than the estimated donor concentration N_D in CdS:Sn NWs. Both, low mobility and low carrier density, clearly indicate self-compensation due to the Sn doping, which is again well in agreement with the luminescence studies. The amphoteric nature of Sn in CdS causes an increased number of ionized donors and acceptors leading to the low mobility by enhanced scattering.

4.4 Continuous wave nanowire lasing

Conventional laser devices require three components: (Optical) pumping, gain material and a resonator structure. Semiconductor NWs inherently provide all this basic components for lasing. Lasing in single NWs is usually proven by power dependent measurements in the high excitation regime [22, 23, 110]. The demonstration of a continuous wave nanowire laser requires a constantly applied, high optical excitation. This goes unfortunately along with significant sample heating and material degradation. Thus, it is important to keep the laser threshold of the NWs as low as possible, in particular below the heat induced damage threshold. Therefore, a semiconductor material with high optical gain, perfect single crystalline structure and excellent optical quality is desirable. In addition, the NWs need to exhibit an optimal resonator structure with smooth end facets. In chapter 4.2 and 4.3, the perfect single crystallinity and high optical quality of single CdS:Sn NWs was demonstrated. Single NWs, e.g. the NW in figure 4.6b, show the desired, good resonator properties such as homogeneous diameter and smooth end facets. Additionally, CdS can exhibit tremendously high optical gain values of $\gtrsim 2.5 \cdot 10^4\,\text{cm}^{-1}$, when it is excited into the electron-hole plasma (EHP) regime [96]. These features make the CdS:Sn NWs a model system for low threshold lasing and hence cw lasing.

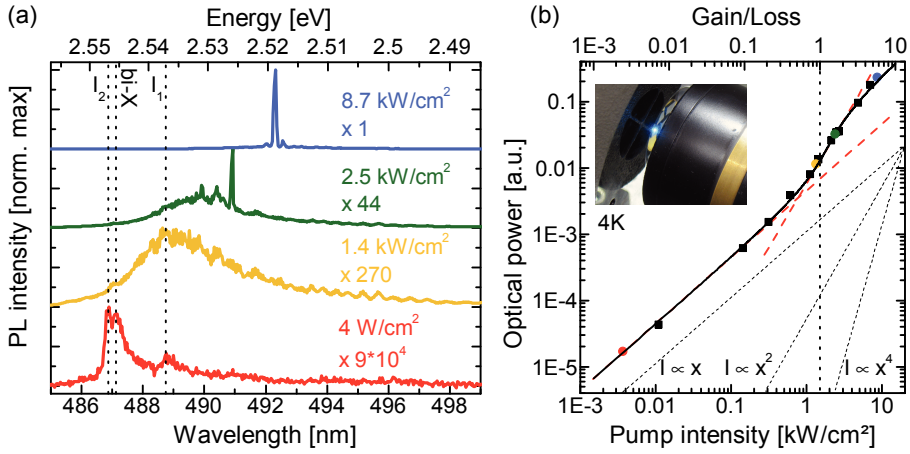

Figure 4.7: (a) Microphotoluminescence end facet spectra at 4 K of the respective CdS:Sn NW in figure 4.6b shows the spontaneous NBE of donor (I_2) and acceptor bound excitons (I_1) at moderate excitation intensities of 4 W/cm^2. At pumping intensities above 1 kW/cm^2 the emission spectra are broadened and red-shifted. The luminescence is superimposed by intensity modulations indicating FP modes. At higher excitations of $\gtrsim$ 2 kW/cm^2, laser modes arise superimposed to the broadened spontaneous emission. These laser modes shift to lower emission energies, as they dominate the spectra at pumping intensities above 5 kW/cm^2. (b) Typical S-shaped power dependence in the double-logarithmic plot of the integrated PL data versus the pump intensity unambiguously proves the cw lasing in the CdS:Sn NW. The data fits the multimode laser model [105] (solid line) with the fitting parameter $x_0 = 0.16$. The dotted lines labelled I $\propto$ x, x^2, x^4 guide the eye to the respective power law. The coloured data points belong to the respective spectra in (a). The inset demonstrates the bright cw laser emission from one single NW.

4.4.1 Nanowire lasing under continuous wave pumping

Figure 4.7a presents the µPL end facet spectra for excitation intensities from few W/cm^2 up to $\sim$ 9 kW/cm^2 of the single CdS:Sn NW shown in figure 4.6b. Note, that the lower x-axis of the spectra now represent the emission wavelength rather than the emission energy, because resonator properties such as mode spacing are defined by optical path lengths. At moderate excitation powers below several hundred W/cm^2, only spontaneous NBE of donor bound (I_2) and acceptor bound (I_1) excitons emerge from the NW end facet indicating an efficient waveguiding. The emission at $\sim$ 487.1 nm was not observed in the low excitation luminescence spectra of chapter 4.3.2 but can be attributed to the formation of biexcitons (bi-X) due to the elevated excitation power [93]. The recombination of bi-X causes the so called M emission band, which is red-shifted by $\sim$ 8 meV relatively to the FX_A [94]. When the excitation power is increased, the M band broadens and shifts to lower energies until it saturates at high pumping intensities of $\sim$ 1 kW/cm^2. The asymmetric emission band between 488 nm and 494 nm occurs above 1 kW/cm^2 superimposed with intensity modulations indicating standing Fabry-Pérot (FP) modes. The modulations are more pronounced at the low energy side of the spectra above 493 nm wavelength, because the guided FP modes exhibit pure photonic character due to low absorption.
The excitation was then increased above 2 kW/cm^2 (green spectrum in figure 4.7a) re-

sulting in the evolution of sharp, equidistant modes superimposed to the broad spontaneous emission. These modes occur at the low energy side of the asymmetric spectrum, where absorption is low. The dominant modes shift further to higher wavelength at $\sim 492.5\,\mathrm{nm}$ and the broad spontaneous emission becomes negligible, if pumping is further increased to $\sim 9\,\mathrm{kW/cm^2}$. Figure 4.7b shows the integrated optical power that is emitted from one NW end facet versus pump intensity. The coloured data points belong to the respective spectra in figure 4.7a. The data follow a S-shaped curve in the double-logarithmic plot, which is characteristic for a laser device, as explained in chapter 2.1.4. The linear slope obtained below $\sim 0.5\,\mathrm{kW/cm^2}$ is attributed to the spontaneous emission regime. The power dependence fades into a superlinear increase approximately at $\sim 2\,\mathrm{kW/cm^2}$, when the sharp, equidistant modes evolve in the emission spectra. This indicates the appearance of amplified spontaneous emission (ASE). The power dependence returns to a linear slope above $\sim 6\,\mathrm{kW/cm^2}$, when the modes already dominate the emission spectra. The power dependence displayed in figure 4.7b is consistent with the Casperson model for multimode lasing [105], which was fitted to the data (solid line). Thus, the evolution of the emission spectra with increasing power as well as the overall power dependence unambiguously prove laser oscillations in one single CdS:Sn NW in cw emission mode. The cw lasing threshold is $\sim 2\,\mathrm{kW/cm^2}$. The inset of figure 4.7b presents a photograph of the bright cw laser emission of this particular NW, which is visible with unaided eye even at ambient light conditions.

4.4.2 Temperature dependence of cw nanowire lasing

In general, carrier dynamics as well as emission properties of semiconductors depend on the ambient temperature, as it was shown earlier within this chapter. At elevated temperatures the ratio of NBE to DLE decreases significantly, because bound and free excitons may dissociate due to the higher thermal energy. Furthermore, the luminescence quantum efficiency usually drops, when the ambient temperature is increased [165, 166], as non-radiative recombinations due to killer centers become apparent. The temperature also influences the Fermi distribution of the charge carriers f_e, f_h and the phonon occupation. This processes contribute to the temperature dependence of the stimulated intrinsic recombination processes in semiconductors, which are responsible for the optical gain.
Since semiconductor lasers rely on intrinsic stimulated recombinations for gain, their laser thresholds exhibit a distinct temperature dependence. According to the literature, the threshold I_{th} of quantum cascade lasers [167], NW lasing due to quantum dots [168] and intrinsic semiconductor NW lasing [169, 170] varies exponentially with the temperature ($I_{th} \propto \exp(T/T_0)$), where T_0 is a characteristic parameter defining the thermal stability of the lasing process. Thus, the ambient temperature was subsequently increased gradually in order to estimated the upper temperature limit of cw lasing in single NWs. Figure 4.8a depicts the temperature dependent lasing performance at a constant pump intensity of $\sim 9\,\mathrm{kW/cm^2}$ of the same CdS:Sn NW as in figure 4.6a,b. The end facet emission spectra

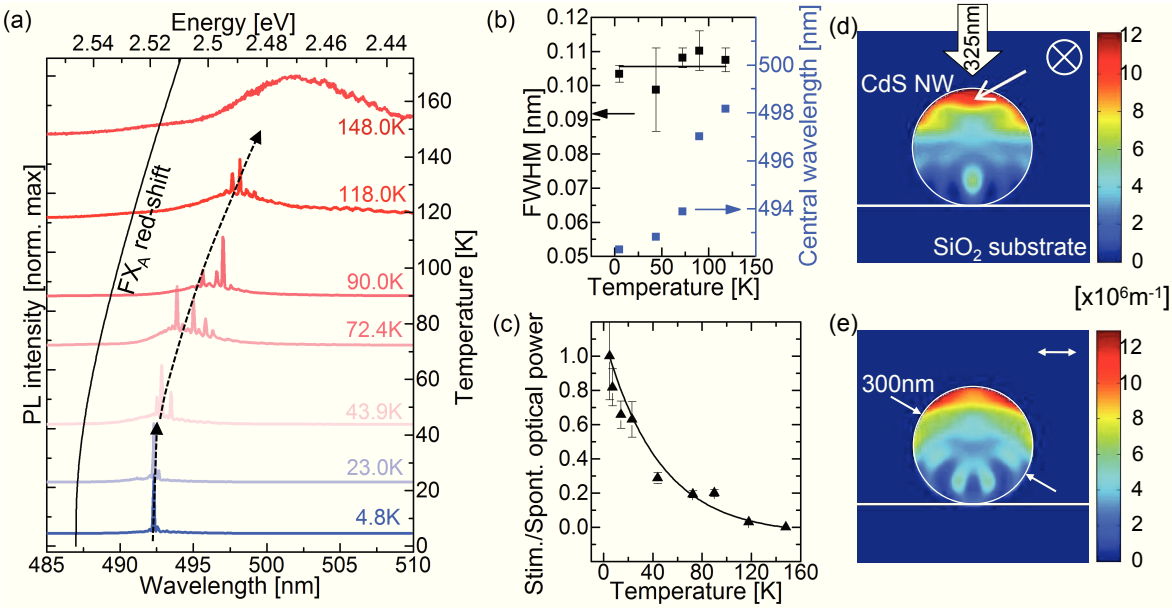

Figure 4.8: (a) Nanowire end facet µPL spectra for temperatures between 4 K and 148 K reveal stable continuous wave lasing up to 120 K. The pump intensity was constant at $\sim 9\,\mathrm{kW/cm^2}$. The longitudinal lasing modes exhibit a red-shift with increasing temperature, as depicted by the dashed arrow. The gain envelopes of the lasing spectra broaden, when the temperature increases. (b) The spectral width of the most intense laser mode (FWHM) remains at a constant value of ~ 0.11 (black) with increasing temperature, whereas the central wavelength shifts significantly to lower energies (blue). (c) The optical gain defined by the ratio of stimulated to spontaneous emission decreases as a function of the temperature. The longitudinal lasing modes and the spontaneous emission of the spectra (a) were fitted by Gaussian functions to obtain the intensity ratio I_{stim}/I_{spont}. (d,e) The absorption cross sections of the CdS NW (diameter ~ 300 nm, similar to the experiment) on SiO_2, optically pumped at 325 nm wavelength with the polarization of the incident light along (d) and perpendicular (e) to the NW axis.

are shifted in such a way that their baseline matches the corresponding temperature adjusted in the cryostat. In addition, the temperature dependent red-shift of the excitonic emission energy at low excitation conditions (chapter 4.3.2) is plotted as solid line in figure 4.8a. For temperatures between 4 K and 25 K, the shift of the lasing modes is almost negligible. A significant red-shift of the lasing modes starts to appear approximately at $\sim$ 40 K, which goes along with a strong broadening of the gain profile with increasing number of modes at the low energy side. The broadening of the gain envelope might be caused by the elevated lattice/carrier temperature, because the Fermi distributions f_e and f_h smear out due to carriers thermally occupying higher energy states. In general, the lasing mode energy qualitatively follows the evolution of the band gap $E_g(T)$, as indicated by the dashed arrow. In figure 4.8b, the central wavelength of the laser emission is plotted as function of the temperature. In reference [96], a comparable red-shift was obtained for EHP gain spectra in CdS single crystals. The cw lasing emission remains stable up to 120 K at the given pump intensity of $\sim 9\,\mathrm{kW/cm^2}$. This is also evident from the constant, low FWHM values of the laser modes between 4 K and 120 K plotted in figure 4.8b. Note, the spectral width of the cw laser modes with $\sim 0.10 - 0.11$ nm is significantly smaller

than the spectral width at pulsed $\sim$ ps or $\sim$ 100 fs pumping [37, 171]. This effect is likely caused by the stable carrier density n during the cw laser operation, wheres the carrier density at pulsed lasing drops dramatically during the inversion depletion within the NW output pulse. This variation in the carrier density causes a change in the refractive index during the output pulse accompanied by a red-shift of the lasing mode, becoming apparent as broadened laser mode in the time integrated spectra. This carrier density driven NW lasing dynamics are explained in more detail in reference [170]. Obviously, the net optical gain decreases with increasing temperature. This is defined by the ratio of stimulated optical power to the amount of broad spontaneous emission underneath the lasing spectra, which is plotted in figure 4.8c. At low temperatures, the lasing modes dominate the emission spectra, while at $\sim$ 120 K only weak stimulated modes appear superimposed to the pronounced spontaneous emission indicating ASE. The data roughly fit an exponential decay and qualitatively coincide with the expected temperature dependence of the lasing threshold intensity ($I_{th} \propto \exp(T/T_0)$). The gain of an EHP in CdS decreases from $5 - 50$ K by a factor of ~ 3 [96]. This is in good agreement with the data in figure 4.8c.

4.4.3 Gain mechanism

In literature, four possible mechanisms are proposed to cause optical gain in highly excited semiconductors with strongly bound excitons ($E_B^{FX} > k_B T$). The CdS:Sn NWs indeed exhibit strong excitonic luminescence especially at low temperatures, see chapter 4.3.1. The four gain mechanisms are exciton-exciton (X-X), exciton-electron (X-e^-) and exciton-phonon (X-LO) scattering as well as the formation of an electron-hole plasma (EHP). The X-e^- scattering mechanism can contribute to stimulated emission only at temperatures above $\gtrsim$ 50 K, whereas the X-LO scattering in principle can contribute already at low temperatures [98]. However, X-e^- and X-LO mediated optical gain requires significantly higher threshold concentrations than the X-X gain mechanism [98, 172]. In addition, the spectral position, in particular that of the X-LO (at $\sim$ 492.9 nm), does not fit to the lasing spectra in figure 4.7a. For this reasons, the X-e^- and X-LO scattering are not considered as possible gain mechanism for the cw lasing in CdS:Sn NWs. Thus, only the X-X scattering and the EHP formation remain as possible gain mechanisms. The room temperature lasing in CdS and ZnO NWs (at pulsed excitation) has been attributed to the EHP gain mechanism, see references [23, 115, 146] and chapter 2.1.6, while pulsed CdS NW lasing at low temperatures was claimed so far to be caused by X-X scattering [173]. The significant red-shift of the lasing mode with increasing excitation power (figure 4.7a) indicates band gap renormalization effects such as in an EHP due to the high carrier densities. In contrast, the X-X scattering mediated lasing process would not shift, if the temperature was kept constant. However, a temperature increase due to high pump intensities seems to contribute to the energetic red-shift of the lasing modes. The NW temperature would need to increase by $\sim$ 60 K between 2.5 kW/cm^2 and 8.7 kW/cm^2 in order to cause a red-shift of $\sim$ 1.3 nm, compare the excitonic red-shift in figure 4.8a. Such

a strong temperature increase would cause also a significant broadening of the gain profile, which is obviously not present in figure 4.7a. In addition, by the comparative µPL study of the temperature induced excitonic red-shift, the heating of the NW was estimated to be only $\sim 35\,\mathrm{K}$, when the pump intensity was increased by more than four orders of magnitude from $0.1\,\mathrm{W/cm^2}$ to $1.2\,\mathrm{kW/cm^2}$ (see supporting information of reference [35]). Hence, the temperature seems not to have a remarkable impact on the red-shift of the lasing mode, thus it must largely be caused by the band gap renormalization of the EHP. Furthermore, the stimulated recombination in an EHP provides high optical gain values of $g \approx 2.5 \cdot 10^4\,\mathrm{cm^{-1}}$. In contrast, the X-X scattering reveals gain values only up to $\sim 160\,\mathrm{cm^{-1}}$ [93]. However, the modal gain in the NW resonator needs to overcome the resonator losses, as described in the equations 2.5-2.7. The confinement factor in a 300 nm wide CdS NW is approximately $\Gamma \sim 1.1$ [39] and the waveguide losses are negligible in comparison to the mirror losses $\alpha_W \ll \alpha_M$. Thus, the material gain needs to exceed the mirror losses by: $1.1 \cdot g > 1/L \cdot \ln(1/R)$. Assuming a mode reflectivity of $\lesssim 0.56$ [39] and the lower length limit for photonic lasing of $\sim 5\,\mu\mathrm{m}$ [137], NW lasing requires an optical gain in the order of $g \gtrsim 10^3\,\mathrm{cm^{-1}}$. Even if the NW in figure 4.6b is homogeneously pumped over its entire length (19.9 µm) and cross section, an optical gain of $\gtrsim 270\,\mathrm{cm^{-1}}$ is necessary to induce lasing. Thus, only the EHP formation provides enough optical gain to ensure NW lasing, while the X-X scattering seems to be insufficient. The lasing mechanism remains most likely unchanged over the whole temperature range from 4 K up to 360 K [170, 174], regardless whether cw or pulsed pumping is applied.

4.4.4 Carrier density under continuous wave excitation

The discussion so far implies that the necessary optical gain for NW lasing is provided by the EHP formation that occurs when the charge carrier density overcomes the Mott density n_M. Therefore, a simplified model is used to estimate the carrier density during cw pumping: The absorption of 325 nm excitation within a circular CdS NW with a diameter of $\sim 300\,\mathrm{nm}$ was calculated by means of FDTD using the complex refractive index data of reference [175]. The inhomogeneous absorption profiles for light with polarization parallel and perpendicular to the NW axis are depicted in figures 4.8d,e. They exhibit high absorption regions close to surface towards the incident pumping beam as well as a focusing effect due to the circular shape of the NW. The absorption was subsequently multiplied by the incident excitation density assuming that each absorbed photon creates an electron-hole pair. Thus, a pattern for the electron-hole pair generation rate G in $[\mathrm{cm^{-3}s^{-1}}]$ is obtained. Then, the semi-empirical model developed for this purpose was applied in two steps. First, the electron-hole pair density n(t) was calculated for a fixed volume with a certain generation rate G (close to the surface as indicated by the arrow in figure 4.8d) neglecting any carrier diffusion. Furthermore, it was assumed that electron-hole pairs recombine with characteristic lifetimes depending on their surrounding carrier density: If the electron-hole pair density is far below the Mott density

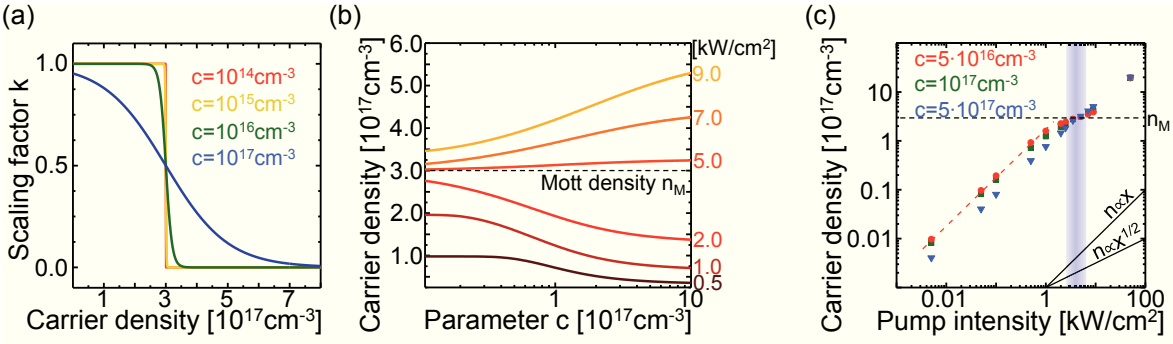

Figure 4.9: Simulation of the carrier density under the continuous wave excitation. (a) The scaling factor k as a function of the carrier density describes the transition from the pure excitonic regime (k = 1) to the EHP regime (k = 0) around the Mott density ($n_M = 3 \cdot 10^{17}\,cm^{-3}$). The transition smears out for an increased transition parameter c. (b) The carrier density for different pump intensities as a function of the transition parameter c reveals that the Mott density is exceeded between $2-5\,kW/cm^2$ nearly independent on the parameter c. (c) The calculated power dependence depicts the carrier density as a function of the pump intensity for three different c values. The carrier density exhibits a linear slope below and above the lasing threshold of $\sim 2\,kW/cm^2$ (blue region). The carrier density overcomes the Mott density n_M around the threshold pump intensity in qualitative coincidence with the experiment.

$n(t) \ll n_M$, the excitons shall recombine isolated from any screening with typical lifetimes of $\tau_X \sim 1\,ns$ [176]. But, if the electron-hole pair density is far above the Mott density $n(t) \gg n_M$, an electron shall recombine with a hole in an EHP-like state with $\tau_{EHP} \sim 200$ ps [177]. Since the semiconductor does not switch abruptly from the excitonic to the EHP regime, the intermediate density regime with $n \sim n_M$ was modelled using a modified lifetime τ^* with $1/\tau^* = k/\tau_X + (1\text{-}k)/\tau_{EHP}$, where k is an introduced scaling factor $k = [\exp(\{n\text{-}n_M\}/c) + 1]^{-1}$, see figure 4.9a. The transition parameter c is approximated with values of $\sim 2 \cdot 10^{16} - 10^{17}\,cm^{-3}$, since the modified lifetime τ^* shall exhibit nearly excitonic lifetimes for $n \lesssim 0.1 \cdot n_M$ and nearly EHP lifetimes for $n \gtrsim 10 \cdot n_M$, respectively. In the calculations, the carrier density reaches almost a constant value after $\gtrsim 10\,ns$. Figure 4.9b depicts this steady carrier density versus the transition parameter c. It exceeds n_M above an excitation of $5\,kW/cm^2$ for all values of c. In addition, the steady state carrier density was calculated as function of the pumping intensity, as shown in figure 4.9c for comparison with the experiment in figure 4.7b. In the excitonic regime below $1\,kW/cm^2$, the power dependence shows a linear slope. The carrier density n overcomes the Mott density at $\sim 3 - 4\,kW/cm^2$, approximately when the transition from ASE to lasing occurs in the experiment. The power dependence reveals a sub-linear slope in the transition region. At higher pumping intensities the carrier density dependence becomes linear again. Thus, the simulations and the experimental observations coincide and prove that the electron-hole pair density indeed can exceed n_M at the experimentally determined laser threshold of $\sim 2\,kW/cm^2$.

In a second step, carrier diffusion was taken into account in order to estimate n(t,x) in the NW cross section. Similar assumptions were used: If $n < n_M$, the excitons diffuse in

an ambipolar manner with the diffusion coefficient $D_X \sim 13\,cm^2/s$ [178]. If $n > n_M$, the electron-hole pair diffuses also ambipolar with $D_{EHP} \sim 10\,cm^2/s$ [179]. Note, the influence of an internal electric field as a result of charge separation is neglected for reasons of simplicity. The transition region between the excitonic and EHP-like state is modelled for diffusion and recombination by the same scaling factor k. At the pumping intensity of $5\,kW/cm^2$ (for $c = 2 \cdot 10^{16}\,cm^{-3}$) an almost steady state is reached after $\sim 50\,ns$, when the electron-hole pair density is homogeneously spread over the NW cross section with an average value of $n \sim 2.7 \cdot 10^{17}\,cm^{-3}$ for parallel polarized excitation and $\sim 2.8 \cdot 10^{17}\,cm^{-3}$ for perpendicular polarized excitation, respectively. Therefore, n reaches almost n_M at pumping intensities slightly higher than the experimentally determined threshold. The average electron-hole pair density increases further with increasing pumping intensity and exceeds n_M for $\sim 9\,kW/cm^2$. Thus, the semi-empirical model slightly overestimates the lasing threshold in comparison with the experiment. The model might be improved by choosing material parameters such as carrier lifetimes and ambipolar diffusion from experimentally determined values for the CdS:Sn NWs.

4.4.5 CW Lasing in undoped CdS NWs and at room temperature

In subsequent studies on undoped CdS NWs, which were synthesized via the VLS mechanism using an Au catalyst, the cw lasing at low temperatures was proven as well [36]. Thus, CdS:Sn and undoped CdS NWs exhibit excellent crystal quality and resonator morphology sufficient for cw lasing. Since both specimen show comparable lasing thresholds of $\sim 1 - 2\,kW/cm^2$ and lasing characteristics such as emission wavelength, the Sn doping seems to have no significant influence on the CdS material properties in the high excitation regime. Therefore, it was valid to use the material lifetimes and diffusion coefficients of undoped CdS for the estimation of the electron-hole pair density during cw pumping in the previous chapter.

By applying a constant cw pumping of $\sim 9\,kW/cm^2$ the lasing emission kept stable up to $\sim 120\,K$. However, an absolute upper temperature limit for cw lasing depends on the weakened optical gain for an increasing temperature. Therefore, the pumping intensity must be increased accordingly, such that an excitation induced heating and degradation problem arises. The laser threshold of a device depends exponentially on the the temperature by: $I_{th} = I_{th,0} \cdot \exp(T/T_0)$ [167–170]. Thus, increasing the upper temperature limit for cw lasing requires either a significant increase of the characteristic temperature T_0 or a decrease of the device threshold $I_{th,0}$. A change of T_0 can be achieved by using other gain materials with different effective carrier masses, as the optical gain of an EHP depends on the density of states [100]. Alternatively, this challenge might be accomplished by exploiting other gain mechanisms, e.g. of quantum mechanically confined structures such as quasi-2D quantum films, 1D quantum wires or even 0D quantum dots [180]. Secondly,

the resonator reflectivity can be optimized in order to lower $I_{th,0}$, e.g. by realizing Bragg reflectors [29] at the NW end facets.

4.5 Summary

Tin doped CdS NWs were synthesized via the VLS mechanism in a horizontal tube furnace. Their structural properties were investigated, revealing that they grow along the c-axis of a perfectly single crystalline wurtzite structure. Although $\sim 1-4\,\text{at.}\%$ of Sn are incorporated into the CdS lattice during growth, the CdS structure remains almost unchanged. Low temperature CL and PL investigations revealed that the incorporation of Sn causes optically active transitions in the semiconductor material, which are absent for undoped CdS NWs. By means of temperature dependent and time-resolved PL studies these transitions were determined as donor-acceptor pair (DAP) and free to bound transitions of a free electron with an acceptor bound hole (e,A). Furthermore, a schematic band diagram was depicted indicating the energetic positions of several donor and acceptor levels in band gap of the CdS:Sn NWs. The coincidence of optical spectroscopy with electrical measurements on single CdS:Sn NWs revealed self-compensation in the CdS:Sn NWs due to the amphoteric nature of Sn in wurtzite CdS.
The grown CdS(:Sn) NWs exhibit an extremely high optical quality and a good resonator morphology enabling low lasing thresholds upon optical pumping. Thus, cw lasing of single NWs could be achieved. Furthermore, the cw lasing emission kept stable up to temperatures of $\sim 120\,\text{K}$ for the given pump intensity of $\sim 9\,\text{kW/cm}^2$. The discussion of the gain mechanism suggests that lasing in CdS:Sn and undoped CdS NWs is most likely induced by the formation of an electron-hole plasma upon high pumping powers. Additionally, calculations revealed that the carrier density under cw excitation overcomes the Mott density at pump intensities of $\sim 2-4\,\text{kW/cm}^2$, which is consistent with the experimental results of the low temperature measurement.

5 Ultrafast temporal dynamics

This chapter reports on the ultrafast temporal dynamics of semiconductor NW based laser devices, including laser onset time and output pulse width. The nanoscaled coherent light sources are distinguished between **photonic** and **plasmonic** NW lasers. Their dynamics were investigated in close collaboration with Dr. Themistoklis Sidiropoulos and Dr. Rupert Oulton (Imperial College London) using a recently developed double-pump measurement technique, see chapter 3.4.2 and the PhD thesis of Themistoklis Sidiropoulos [118]. Parts of this results are published in references [37, 38].

5.1 Motivation

Understanding the fundamentals of semiconductor NW based lasers encourages conceptional thinking of ideas that exploit coherent radiation available at dimensions below the wavelength barrier [181]. These concepts include nonlinear frequency generation [16], single molecule sensing [15, 182], optical switching [17] and embedding the nanoscaled coherent light sources in photonic circuitry. Fundamental properties of NW lasers such as emission wavelength, polarization features [33, 39] and resonator modification treatments [27, 28] have been investigated thoroughly, while the NW laser dynamics remain relatively unstudied. The temporal NW laser responses are difficult to measure due to their ultrafast nature between hundreds of femtoseconds and a few picoseconds. In addition, the far field intensity of single NW lasers is rather weak, thus conventional pulse characterization techniques, such as measuring the autocorrelation, fail. However, knowing the NW operation speed is crucial to fully exploit the potential of the NW coherent light source. The laser dynamics include the onset time of lasing τ_{on} as well as the output pulse width $\mathrm{t_{pulse}}$. In this thesis, a double-pump approach was used, that exploits the nonlinearity of the laser process itself, in order to study these NW laser dynamics. The laser onset time is first investigated for CdS, ZnO and GaN NWs providing insights into its dependency on material properties. Additionally, the onset time shall be modified by adjusting the pump energy. Then, the laser pulse width (upper limit) is determined for plasmonic ZnO NW lasers in comparison to photonic NW lasers (diameter $\lesssim 200\,\mathrm{nm}$) in order to verify an enhanced light-matter interaction due to hybrid plasmonic modes, as plasmonic ZnO NW lasers are predicted to exhibit Purcell enhanced stimulated and spontaneous decay rates.

5.2 Nanowire lasing under sub-ps pulsed pumping

The NW lasers were optically pumped at room temperature using pulses of nominally $\sim 150\,\mathrm{fs}$. Therefore, the NW lasers exhibit significantly different emission features than

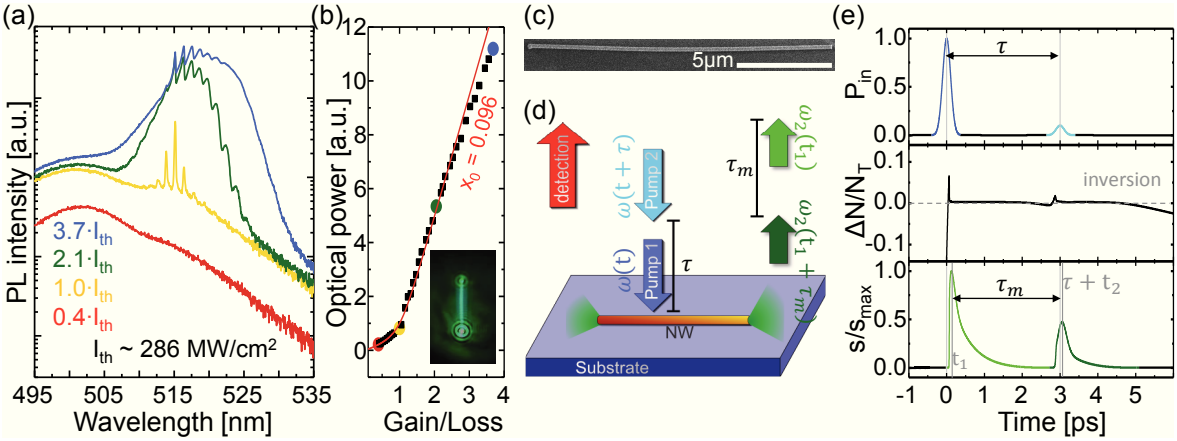

Figure 5.1: (a) Output spectra of the respective CdS NW in (c) for four different pump intensities at 300 K. Below the threshold I_{th}, featureless spontaneous emission originates from the NW, while stimulated FP modes dominate the spectra above I_{th}. (b) The laser power dependence of the CdS NW as a function of the gain/loss ratio is fitted by a multimode laser model [105] with the laser threshold $I_{th} \sim 286\,MW/cm^2$ and $x_0 = 0.096$. The inset shows a luminescence image of the lasing CdS NW. (c) SEM image of the CdS NW (length 15.9 µm; diameter ≈ 190 nm). (d) Schematic drawing of the double-pump measurement technique applied to a NW lying on a low refractive index substrate. (e) The upper graph shows the impinging power of the strong pump 1 followed by the weak pump 2, which is time-delayed by τ. The middle graph reveals the material response to the two pump pulses as the difference in population ΔN between excited (upper) laser level and the ground (lower) laser level. The graph is normalized to the maximum inversion N_T. The lower graph shows the normalized cavity photon number s/s_{max} for the NW laser.

in the cw operation mode (compare chapter 4) or at pumping with ∼ns pulses as in references [22, 23]. The differences become especially apparent at high optical pumping with excitation powers $\gtrsim 2 \cdot$ threshold. Figure 5.1a shows the CdS NW emission for pump intensities ($\lambda_{exc} = 355$ nm) between $\sim 0.4 \cdot$ threshold and $\sim 3.7 \cdot$ threshold with ~ 150 fs excitation pulses. Only featureless spontaneous emission originates from the NW far below the threshold, where the power dependence in figure 5.1b reveals a linear slope. Sharp and equidistant FP modes appear superimposed to the broad spontaneous emission around the laser threshold accompanied by a superlinear power dependence in figure 5.1b. At pump intensities well above the threshold the power dependence returns to a linear slope indicating stable laser oscillations in the CdS NW shown in figure 5.1c. The lasing modes unambiguously dominate the emission spectra in the lasing regime, while the gain envelope broadens at the low energy side of the spectra typical for EHP gain. In addition, the lasing modes seem to broaden and start to smear out in the time-integrated spectra. This was not observed for cw and ∼ ns pumping [22, 23, 35].

This broadening is a consequence of the temporal carrier dynamics achieved under fast optical pumping. The refractive index of the NW material decreases for high carrier densities compared to the unexcited condition. As the high carrier density is decreasing during the NW laser output, the refractive index n increases accordingly [183]. The increasing refractive index leads to a red-shift of the NW lasing modes according to the mode condi-

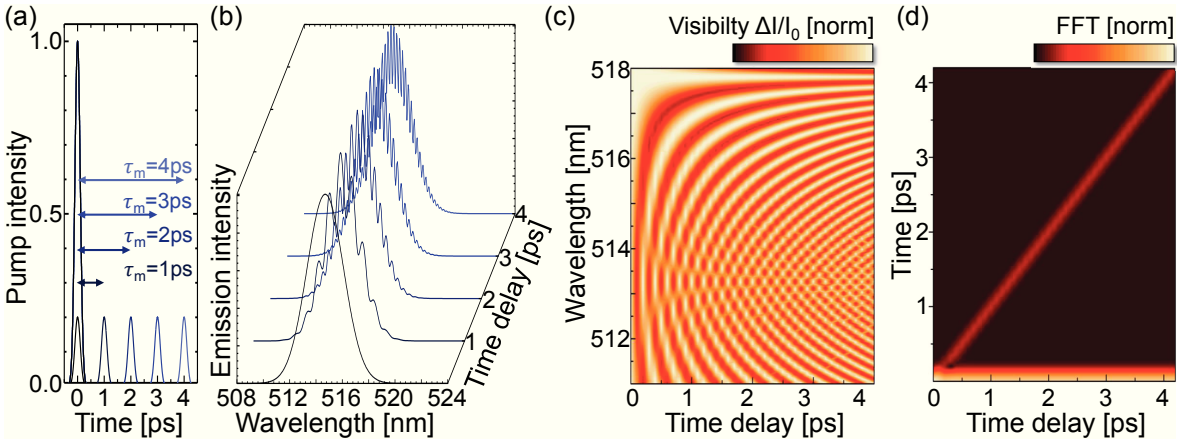

Figure 5.2: (a) Series of five different time delays between two interfering Gaussian pulses ($\tau_{\mathrm{pulse}} = 0.1\,\mathrm{ps}$; amplitude ratio of 1:0.2) with respective temporal separations of $\tau_{\mathrm{m}} = 0; 1; \ldots; 4\,\mathrm{ps}$. (b) The Fourier transform of the respective two pulses from (a) into the frequency domain reveals unambiguously the interference pattern. The modulation frequency of the interference increases with increasing τ_{m}. (c) Differential spectral intensity $\Delta\mathrm{I}(\lambda,\tau)/\mathrm{I}_0(\lambda)$ of two interfering pulses versus the time delay. (d) The Fourier transform of the interference spectra as a function of the time delay reveals a sideband with a linear slope.

tion $\lambda_{\mathrm{mode}}/\mathrm{n}_{\mathrm{eff}} = \mathrm{const}$. This red-shift of the FP modes becomes apparent as a broadening of the mode in the time-integrated spectra. It has been shown in reference [170], that the refractive index changes by $\sim 2-3\,\%$ during the output pulse of a ZnO NW laser. It can expected that the refractive index of CdS NW lasers changes similarly. However, if the pump pulse is temporally much longer than the NW output pulse ($\sim 20\,\mathrm{ps}$), the mode shift can be neglected. The NW material remains over this time range in a steady state condition with stable refractive index n, as charge carriers are constantly generated and recombined. The emitted light shows thus sharp mode lines in the time-integrated spectra.

5.3 Nanowire laser onset time

5.3.1 Two output pulse interference

Figure 5.1d depicts a schematic drawing of the double-pump measurement technique. The pump wavelength for the lasing measurements and the double-pump measurements is usually set to 355 nm, but some NWs were excited at 420 nm in order to highlight the pump energy dependence of τ_{on}. Figure 5.1e shows the expected NW response to the double-pump excitation calculated using the rate equations in chapter 3.5. References [38, 118] provide a more detailed description of this technique. This thesis only refers to positive time delays $\tau > 0$, when the strong pump 1 approaches first. Pump 1 inverts the laser levels to $\Delta\mathrm{N}/\mathrm{N}_{\mathrm{T}} > 0$, as it has sufficient power to cause lasing. Here, $\Delta\mathrm{N} = \mathrm{N}_3 - \mathrm{N}_0$ denotes the difference between the upper and the lower laser level and N_{T} is the total number of excited carriers. The population inversion is then depleted by the emission

of an output pulse with its maximum at t_1. Subsequently, the weak pump 2 approaches at the time delay τ. Pump 2 is not able to induce lasing on its own, but effectively samples the laser process that was induced by pump 1. The dynamics of the total output power of the double-pump measurement as function of the time delay τ will be explained in chapter 5.4. Here, short time scales $\tau \lesssim 8\,\mathrm{ps}$ are evaluated, when the absorption of pump 2 induces a second output pulse at a time τ_m after the first output pulse. For these short time scales the second pulse can, in case of coherence, interfere with the first pulse. Therefore, the NW laser output needs to be measured temporally as well as spectrally as function of τ in the time regime 0 ps $< \tau <$ 8 ps. Note that $(\tau + t_2) = (\tau_m + t_1)$ in figure 5.1e.

The expected interference and the related aspects in the spectral response are displayed by the simulations in figure 5.2. Figure 5.2a shows a series of five different time delays between the two interfering Gaussian pulses, which are temporally separated by $\tau_m = 0; 1; \ldots; 4\,\mathrm{ps}$. The electric field of the pulses is given by:

$$E(t) = E_0 \cdot e^{-t^2 \ln 2/\sqrt{2}\tau_{pulse}^2} \cdot e^{i\omega_0 t}, \tag{5.1}$$

with a pulse width of $\tau_{pulse} = 0.1\,\mathrm{ps}$, the central wavelength $\lambda_0 = 514.5\,\mathrm{nm}$ and an amplitude ratio of 1:0.2. Figure 5.2b depicts the corresponding time-integrated interference spectra of the two Gaussian pulses for the five respective time delays. The interference of two pulses in the frequency domain can be written as:

$$\begin{aligned} |E_1 e^{i\Phi_1(\omega,\tau)} + E_2 e^{i(\Phi_2(\omega,\tau)-\omega\tau_m)}|^2 = |E_1 e^{i\Phi_1(\omega,\tau)}|^2 + |E_2 e^{i(\Phi_2(\omega,\tau)-\omega\tau_m)}|^2 \\ +2E_1E_2\cos\left(\omega\tau_m + \Delta\Phi(\omega,\tau)\right), \end{aligned} \tag{5.2}$$

with the difference of the spectral phases of the two pulses $\Delta\Phi(\omega,\tau)$. The third term in equation 5.2 indicates the increasing modulation frequency of the spectral intensity with increasing time delay τ_m, which becomes apparent in figure 5.2b. Furthermore, the spectral response is modelled for varying time delays in steps of $\Delta\tau = 100\,\mathrm{fs}$. In figure 5.2c the normalized visibility $\Delta I(\omega)/I_0(\omega)$ is plotted as function of the time delay. The visibility can be obtained by re-writing equation 5.2 as:

$$\Delta I(\omega) = I(\omega)_{1+2} - I(\omega)_1 - I(\omega)_2 = 2E_1E_2\cos\left(\omega\tau_m + \Delta\Phi(\omega,\tau)\right) \tag{5.3}$$

and $I_0(\omega) = I(\omega)_1 + I(\omega)_2$. The colour plot in figure 5.2c unambiguously shows the decreasing modulation period of the spectral output when τ_m is increased. However, the time delay τ_m between the two pulses cannot be accessed directly from this plot. Obtaining information about the temporal characteristics of the output pulse requires a Fourier transformation of the spectral intensity modulation. The Fourier transform of the spectral intensity into the time domain in figure 5.2d reveals the temporal characteristic of the two output pulses as a sideband that follows the linear trend $\tau_m = \tau - (t_1 - t_2)$.

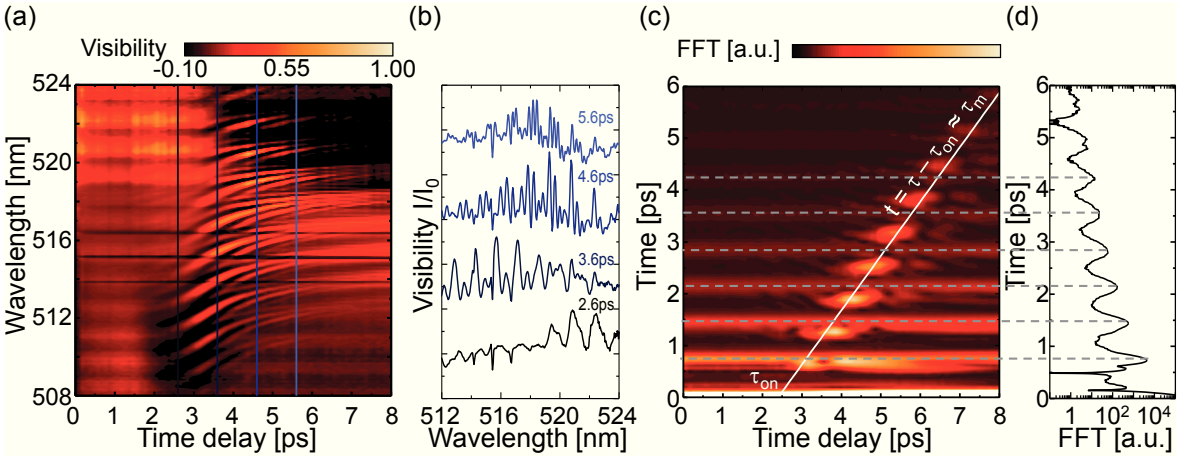

Figure 5.3: (a) The normalized difference spectra $\Delta I(\lambda,\tau)/I_0(\lambda) = I(\lambda,\tau)/I_0(\lambda) - 1$ (visibility) of the CdS NW in figure 5.1c, with the µPL spectrum at double-pump excitation $I(\lambda,\tau)$ and the µPL spectrum at single strong pulse excitation $I_0(\lambda)$. Pump 1 (pump 2) power was set to twice ($0.2\times$) the laser threshold. (b) The visibility spectra for time delays of $\tau = 2.6$; 3.6; 4.6; 5.6 ps reveal the increasing spectral modulation frequency. The position of the respective linescans is marked in (a) by vertical coloured lines. (c) Fourier transform (FFT) of each interference spectrum $I(\lambda,\tau)$ versus the time delay τ. The white line depicts the linear trend of the sideband $\tau_m = \tau - \tau_{on}$ with $\tau_{on} \approx 2.5$ ps. (d) Fourier transform of the lasing spectrum obtained at single-pump excitation with twice the laser threshold.

The sideband amplitude does not get weaker, because an amplitude decay of the pulses is not taken into account here, see figure 5.2a. Furthermore, any temporal retardation of the two output pulses relatively to the pump pulses is neglected here, thus $t_1 = t_2 = 0$.

5.3.2 Determination of laser onset time

Since NW lasers generate two coherent output pulses under double-pump excitation, it is possible to determine their approximate laser onset time τ_{on} by measuring the appearance of interferences in the lasing spectra. Figure 5.3a shows such results for the CdS NW, which is displayed in figure 5.1c, excited with the strong pump 1 and the weak pump 2. Pump 1 was set to twice the laser threshold, while pump 2 excited the NW at ~ 0.2 times the laser threshold. In general, this relative values for pump 1 and pump 2 were applied to all NW lasers during the measurement. The spectral output of the NW laser $\Delta I/I_0$ in figure 5.3a clearly changes with increasing time delay τ as indicated by equation 5.3. Indeed, modulation emerges between $\sim 2-3$ ps. Furthermore, linescans between $\tau = 2.6 - 5.6$ ps indicate an unambiguous increase in the modulation frequency, see figure 5.3b. The interference spectra were Fourier transformed into the time domain revealing the sideband that is caused by the increasing spectral modulation (figure 5.3c). Additionally, the experimentally measured sideband exhibits the expected linear dependence $\tau_m = \tau - (t_1 - t_2)$, which was simulated in figure 5.1e. Now, taking into account that the NW laser is still inverted or even close to inversion, when the weak pump 2 impinges on the NW, it is reasonable to assume that $t_1 \gg t_2$. This is consistent with the calculated

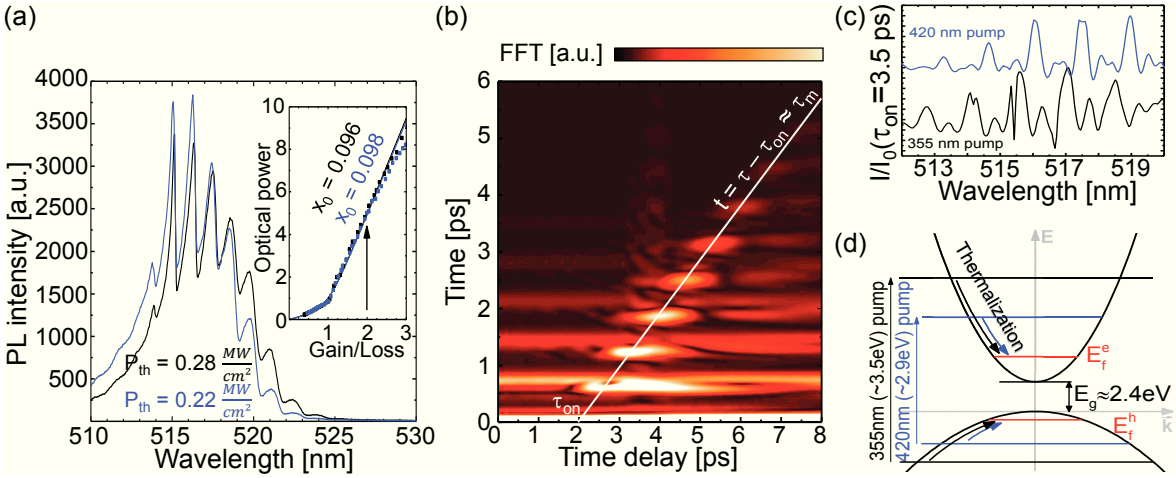

Figure 5.4: (a) Lasing spectra of the CdS NW shown in figure 5.1c at pumping wavelengths of 420 nm (blue) and 355 nm (black). The pump intensity was set to twice the threshold indicated by the arrow in the power dependences (inset). Spectra and normalized power dependences show nice coincidence for both pump wavelengths. (b) The Fourier transform of the double-pump measurement ($\lambda_{exc} = 420$ nm) reveals the sideband that is shifted to shorter time delays compared to figure 5.3c with an x-axis intersect at $\tau_{on} \approx 2.0$ ps. (c) Normalized difference spectra at $\tau = 3.5$ ps for 420 nm (blue) and 355 nm (black) pumping. (d) The schematic band diagram of CdS depicts the reduction of the pump energy leading to a decreased thermalization time that ultimately causes a shorter τ_{on}.

laser response in figure 5.1e. Thus, the x-axis intersect of the linear sideband $t_1 \lessapprox \tau_{on}$ corresponds to the time required to establish an output pulse after optical excitation. The CdS NW therefore reveals an onset time of $\tau_{on} \approx 2.5$ ps at $\lambda_{exc} = 355$ nm. Further investigated CdS NW lasers with different diameters exhibit similar τ_{on} values of ~ 2.5 ps, indicating that the onset time is a material driven parameter, which does not depend on the optical system or the transverse laser mode. In addition to the intense sideband, time delay independent modulations occur in the FFT marked with horizontal dashed lines. These constant modulations are caused by the longitudinal FP modes in the NW laser spectra, as depicted in the FFT signal of a single-pump lasing spectrum in figure 5.3d.

5.3.3 Tuning the laser onset time

After pumping CdS NW lasers at 355 nm (≈ 3.49 eV) an output pulse around ~ 515 nm (≈ 2.41 eV) is established approximately 2.5 ps later, independent of the optical cavity. As τ_{on} is an indication of the thermalization time of the excited carriers to the upper laser level, the large difference between pump and output energy of ~ 1.01 eV holds therefore potential to decrease the laser onset time by a reduction of the pump energy. Thus, the exact same CdS NW, shown in figure 5.1c, was subsequently investigated by pumping with a reduced excitation energy of ~ 2.95 eV (420 nm). The lasing performances for both pumping conditions (420 nm and 355 nm) are compared in figure 5.4a. Both lasing spectra were obtained at twice the laser threshold and coincide, as they reveal the iden-

tical longitudinal modes and similar output intensities. The gain envelope shows a slight blue-shift and the lasing threshold decreases for the pump energy of 2.95 eV. However, the normalized laser characteristics perfectly coincide, as depicted in the inset of figure 5.4a. Furthermore, an impact of the pump energy on the transverse modes can be neglected, as the laser emission from the CdS NW remains predominantly polarized perpendicular to the NW axis [37]. Figure 5.4b shows the FFT signal obtained from the interference spectra at double-pump excitation with 420 nm. The sideband exhibits in agreement with figure 5.3c a clear linear dependence, but is now shifted to significantly shorter time delays. Thus, the x-axis intersect occurs now at a lower value of $\tau_{\mathrm{on}} \approx 2.0\,\mathrm{ps}$. Furthermore, the spectral modulation appears also at shorter time delays accompanied by a higher modulation frequency for a fixed time delay, as depicted in figure 5.4c for $\tau = 3.5\,\mathrm{ps}$. Therefore, the laser onset time is significantly reduced by $\sim 0.5\,\mathrm{ps}$, when the pump energy is reduced from $\sim 3.49\,\mathrm{eV}$ to $\sim 2.95\,\mathrm{eV}$. Note that the time delay independent modulations in the FFT occur at the same time values as for 355 nm pumping, because the CdS NW exhibits the same longitudinal lasing modes independent of the pump energy, compare figure 5.4a. Similarly, the onset time of a 270 nm diameter CdS nanowire changed from a value of $\tau_{\mathrm{on,420\ nm}} \approx 1.9\,\mathrm{ps}$ to $\tau_{\mathrm{on,355\ nm}} \approx 2.3\,\mathrm{ps}$, when the pump energy was increased from $\sim 2.95\,\mathrm{eV}$ to $\sim 3.49\,\mathrm{eV}$. Figure 5.4d shows a schematic drawing of the CdS band structure for the case of 355 nm and 420 nm pumping, respectively. Treating the semiconductor NW laser schematically as a multilevel laser system, the pump level (black for 355 nm, blue for 420 nm) and the upper laser level defined by the quasi Fermi levels $\mathrm{E_F^e}$ and $\mathrm{E_F^h}$ (red) become energetically closer in order to reduce the "density" of states that the carriers have to thermalize through. Thus, this approach is capable of controlling the onset time of a NW laser and solely relies on the band structure of the respective material.

5.3.4 Material dependent laser onset time

Different NW gain materials such as CdS [23, 39], ZnO [115] and GaN [133] were quantitatively compared in order to gain insights about the physical properties determining the onset time and carrier thermalization/relaxation. To this end, photonic GaN NWs emitting in the UV spectral range were examined applying a 355 nm pump in comparison to ZnO NWs [38, 118] and CdS NWs described in chapter 5.3.2. An exemplary GaN NW with 10.5 µm length and $\sim 630 - 710\,\mathrm{nm}$ diameter is shown in figure 5.5a. The evolution of the emission spectra with increasing pump intensity (see supporting information of reference [37]) accompanied by the power dependence in figure 5.5b unambiguously prove laser oscillations in this particular GaN NW. The thick GaN NWs seem to exhibit multi-transverse mode lasing, as several stimulated emission peaks in the output spectra reveal different polarization orientations [184]. However, the laser light is mainly emitted from the NW end facets, as shown in the inset of figure 5.5b, indicating still a FP-like cavity. Figure 5.5c shows the FFT signal obtained for this particular GaN NW laser after applying the double-pump technique. The evaluation of the linear sideband in the FFT

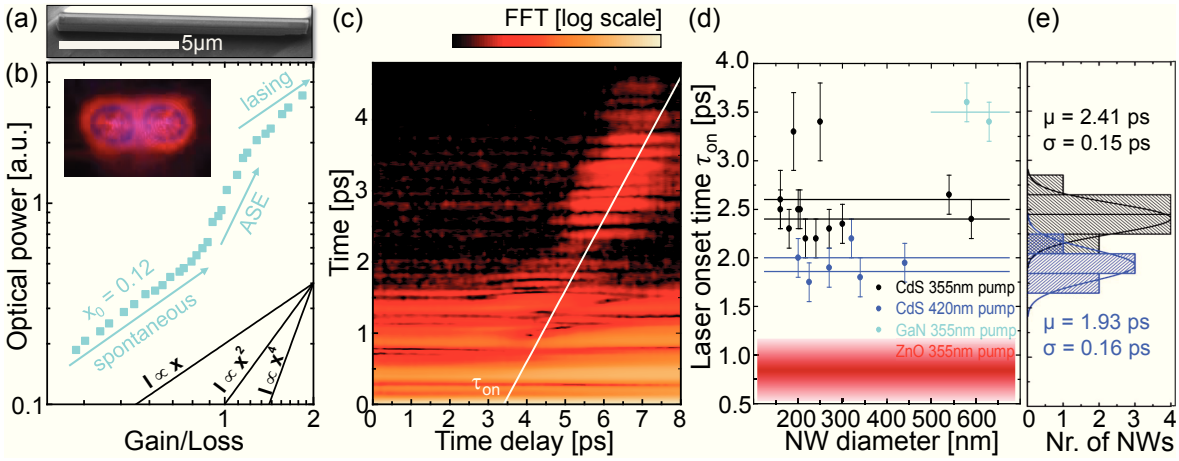

Figure 5.5: (a) The SEM image of an exemplary GaN NW laser (10.5 µm length, diameter $\sim 630-710$ nm) lying on a 1.5 µm SiO_2 layer on Si substrate. (b) The double logarithmic power dependence of the GaN NW exhibits the three characteristic power regimes of spontaneous emission, ASE and lasing. The inset shows a luminescence image of the lasing GaN NW. (c) The Fourier transform (FFT) signal in logarithmic scale of the GaN NW at double-pump excitation exhibits the linear sideband (white line) with $\tau_{on} \approx 3.4$ ps. (d) The laser onset times τ_{on} versus the NW diameter for ZnO (red) taken from ref. [38, 118], GaN (cyan) and CdS (black) using $\lambda_{exc} = 355$ nm and CdS (blue) at $\lambda_{exc} = 420$ nm, respectively. The τ_{on} value is independent of the NW diameter as marked by the horizontal lines. (e) The statistical evaluation of $\tau_{on,355\ nm}$ and $\tau_{on,420\ nm}$ proves that the statistical NW-to-NW variation is smaller than the change for the two different pump wavelengths. On average, ~ 75 % of the CdS NWs exhibit $\tau_{on,355\ nm} \geq 2.30$ ps, while ~ 75 % reveal $\tau_{on,420\ nm} \leq 2.04$ ps.

signal reveals a laser onset time of $\tau_{on} \approx 3.4$ ps. The FFT signal is depicted in a logarithmic scale, because the interference modulations appear less resolved in the time-delayed spectra due to the high number of transverse and longitudinal modes. Thus, the τ_{on} value of GaN NWs is surprisingly slow as the pump energy of ~ 3.49 eV is energetically much closer to the band gap of GaN compared to CdS. However, the time scale of $\sim 3-4$ ps fits recent results for the carrier thermalization in optically excited GaN nanorods obtained by pump-probe measurements [185].

Energy-loss ratio

Figure 5.5d shows the laser onset time τ_{on} of several NW lasers versus their NW diameter. The error $\Delta\tau_{on} \lesssim 0.2$ ps for CdS and GaN NWs was analyzed by fitting the intense spots of the FFT sideband as in figure 5.3c by a Gaussian envelope. Subsequently, the FWHM of the Gaussian envelope is used as error bar for the linear fitting of the FFT sideband in order to evaluate the x-axis intersect including its error value. For an excitation wavelength of 355 nm, the fastest laser onset time occurs for ZnO NWs with $\tau_{on} \sim 0.7-1.1$ ps [38,118], followed by CdS NWs revealing $\tau_{on} \approx 2.5$ ps, while GaN NWs exhibit the slowest onset time of $\tau_{on} \approx 3.5$ ps, although the difference between excitation and emission energy is smallest for GaN. Thus, the carrier thermalization/relaxation defined by the carrier energy loss rate (ELR) is significantly different for the three semiconductors [186].

In addition, the average onset time of CdS nanowire lasers is accelerated from a value of $\tau_{\mathrm{on,355\ nm}} = (2.55 \pm 0.10)\,\mathrm{ps}$ to $\tau_{\mathrm{on,420\ nm}} = (1.93 \pm 0.07)\,\mathrm{ps}$, compare figures 5.5d,e. The ratio of reduced pump energy to reduced onset time corresponds approximately to an ELR of the whole carrier system of $\sim 1\,\mathrm{eV/ps}$. Theoretical calculations by Pugnet et al. [187] predict for CdS an ELR of $\sim 1.9\,\mathrm{eV/ps}$ for a lattice temperature of 4 K and an EHP temperature of 500 K. Since the carriers relax largely by scattering with LO phonons in this energy regime, the temperature dependence of $\langle \mathrm{dE/dt} \rangle_{\mathrm{e\text{-}LO}}$ (equation (3) in reference [188]) can be applied to extrapolate the ELR of Pugnet et al. to room temperature with a value of $\sim 1.1\,\mathrm{eV/ps}$, which is in good agreement with the above estimation for the ELR in CdS.

Electron-phonon interaction

The different onset times for the various semiconductor materials, shown in figure 5.5d, are attributed to the thermalization/relaxation processes after optical excitation, when the excited carriers are subject to microscopic many-body dynamics. In general, excited carriers exhibit spatial and temporal evolution of different characteristic time scales in the respective semiconductors. Photoexcitation initially creates non-equilibrium (quasi-monochromatic distributed) carriers, which evolve towards a quasi-equilibrium distribution within femtosecond time scales via elastic and inelastic carrier-carrier scattering, such that a relaxation of momentum and energy in the carrier system is achieved [189]. However, energy relaxation of the carriers is largely achieved due to excitation of phonons [99]. Thus, the different onset times can be explained by considering carrier-phonon interaction. Carrier diffusion is neglected, because typical diffusion lengths are small within the picosecond time scale [179]. Furthermore, only electrons need to be considered, because (i) the excess energy of photoexcited holes $\Delta \mathrm{E_h}$ reveals much lower values than the excess energy of electrons $\Delta \mathrm{E_e}$. The excess energy is defined by [190]

$$\Delta \mathrm{E_{e(h)}} = (\mathrm{E_{exc}} - \mathrm{E_g}) \cdot \left(1 + \mathrm{m_{eff}^{e(h)}}/\mathrm{m_{eff}^{h(e)}}\right)^{-1}, \tag{5.4}$$

where $\mathrm{E_{exc}}$ is the excitation energy and $\mathrm{m_{eff}^{e(h)}}$ is the effective electron (hole) mass. (ii) Additionally, the hole relaxation rates are higher in all three materials because of the higher effective hole masses [187, 191, 192].

The conduction bands (CB) of ZnO (red), CdS (black) and GaN (cyan) are schematically depicted in figure 5.6a including the respective energies of LO and transverse optical (TO) phonon modes. Electrons dissipate their excess energy mainly into the emission of LO phonons, such that they relax towards the CB minimum, until the electrons do not posses enough energy to emit further LO phonons due to a violation of the energy conservation [189]. Among the electron-phonon interactions, the electron-LO phonon interaction enables the highest ELR. The long-range electron-LO interactions is defined by the Fröhlich coupling constant α, which can be calculated by [193]:

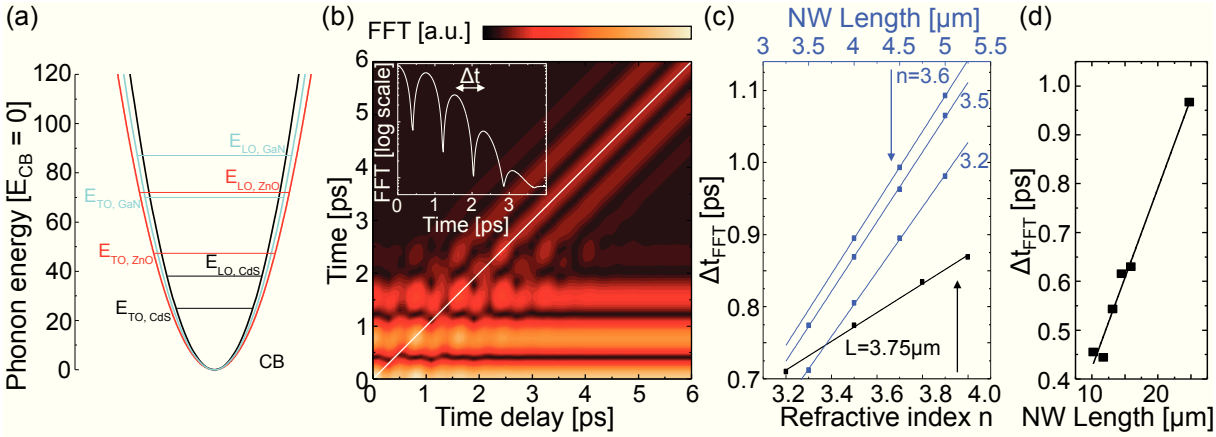

Figure 5.6: (a) Schematic of the conduction bands (CB) of CdS (black), ZnO (red) and GaN (cyan) including the energetic positions of the LO and TO phonons. The different dispersions indicate the different effective electron masses. (b) Simulated FFT signal of the interference spectra of two double-FP mode laser pulses with $\tau_{\mathrm{pulse}} = 1\,\mathrm{ps}$ that are time-delayed by τ_{m}. The inset shows the FFT signal obtained as the linescan (white line) along the sideband. (c) The calculated FFT sideband modulation period Δt_{FFT} versus the refractive index (black) and the NW length (blue) reveal a linear dependence. The FP mode numbers remain constant. (d) The measured sideband modulation period Δt_{FFT} as a function of the NW length for several CdS NWs exhibits a linear slope similar to (c). The linear dependence indicates that the sideband modulations are attributed to the FP type NW cavity.

$\alpha = \mathrm{e}^2\sqrt{\mathrm{m_{eff}}/2\hbar^2\hbar\omega_{\mathrm{LO}}}\,(1/\varepsilon_\infty - 1/\varepsilon_0)$, with the respective high- and low frequency dielectric constants ε_∞, ε_0. Thus, ZnO exhibits the strongest electron-LO phonon coupling with $\alpha_{\mathrm{ZnO}} = 1.0$ [194], while CdS and GaN reveal weaker coupling of $\alpha_{\mathrm{CdS}} = 0.54$ [194] and $\alpha_{\mathrm{GaN}} = 0.49$ [55], respectively. Since the $\mathrm{ELR_{LO}}$ is directly proportional to the Fröhlich coupling constant for a given electron temperature $\mathrm{T_e}$ [186], the photoexcited carriers in ZnO relax significantly faster than in CdS and GaN. In addition, the carrier relaxation in GaN suffers from the hot phonon effect, which substantially reduces the LO emission rate $\tau_{\mathrm{LO}} \propto \alpha^{-1}$ and the ELR by ~ 20 times [188,189]. The hot phonon effect occurs, when LO phonons, which are created by the relaxation of hot carriers, do not have enough time to decay, leading to an increased probability of reabsorbing phonons.

Electrons, which exhibit a remaining kinetic energy between LO and TO phonons, relax largely by the interaction with TO phonons. The electron-TO phonon interaction is determined by the optical deformation potential and its $\mathrm{ELR_{TO}}$ is at least one order of magnitude lower than $\mathrm{ELR_{LO}}$ [187, 189]. If the electron energy subsequently drops below the TO phonon energy, only electron-acoustic phonon interaction causes an energy release. The electron-acoustic phonon interaction depends on the acoustic deformation potential and the piezoacoustical interaction potential [59,187]. Table 5.1 summarizes the respective quantities for the three semiconductor materials qualitatively explaining the different carrier relaxation and laser onset times in ZnO, CdS and GaN. The GaN NW lasers exhibit the slowest carrier relaxation for two main reasons: The hot phonon effect significantly weakens the electron-LO phonon interaction, such that the respective GaN

Table 5.1: Electron-phonon interaction: Overview over the respective constants determining the relaxation time τ_{relax}. The LO phonon emission rate was calculated according to reference [186]: $\tau_{\mathrm{LO}} = (2\alpha\omega_{\mathrm{LO}})^{-1}$. Since GaN exhibits a strong hot phonon effect, τ_{LO} decreases from the theoretical value in brackets to an actual measured value.

	ZnO	GaN	CdS
Fröhlich coupling constant α	1.0 [194]	0.49 [55]	0.54 [194]
LO phonon emission rate τ_{LO}	$\sim 219\,\mathrm{ps}^{-1}$	$\sim 5\,(116)\,\mathrm{ps}^{-1}$ [188]	$\sim 62\,\mathrm{ps}^{-1}$
Optical deformation potential	49.7 eV [196]	41.0 eV [197]	29.6 eV [196]
Acoustic deformation potential	15 eV [194]	10.1 eV [198]	7.0 eV [194]

$\mathrm{ELR_{LO}}$ is $\sim 5\,(30)$ times smaller than in CdS (ZnO) for the same carrier temperatures $\mathrm{T_{e,h}}$. Additionally, the high LO and TO phonon energies in GaN in comparison to ZnO and CdS induce a wide energetic region, in which the carriers release their excess energy only by the weak interaction with TO and acoustic phonons. Therefore, it is now possible to give a rough estimate of laser onset times for other technological relevant semiconductor materials such as GaAs. It is very likely that GaAs has an even slower τ_{on} than GaN, since it suffers also from the hot phonon effect [190]. Indeed, GaAs NW lasers revealed a slow value of $\tau_{\mathrm{on}} \sim 6 - 7\,\mathrm{ps}$ at a pump energy of 1.59 eV in recent studies using the similar double-pump approach [195]. In general, among the semiconductor materials that are usually used for NW lasers, ZnO ought to exhibit the fastest laser onset time τ_{on} due to the strongest carrier-phonon coupling with $\alpha = 1$ [37].

5.3.5 Sideband modulation in the time domain

The temporal characteristics of the NW output pulses occur as linear sideband in the FFT of the spectral intensity modulation in well agreement with the simulations in figure 5.2. However, the experimental obtained FFT sidebands, as shown in figures 5.3c and 5.4b, exhibit intensity modulations. These sideband modulations were not predicted by simulating the interference of two time-delayed Gaussian pulses with a single central wavelength, compare equation 5.2. Since the experimentally obtained FFT signals revealed time delay independent intensity modulations caused by the FP modes of the NW cavity, further simulations were carried out similar to chapter 5.3.1, but now for multi-longitudinal mode lasing.

The optical gain spectrum was defined between 508 nm and 525 nm, the NW length was adjusted between 3 µm and 5 µm in order to enable two FP modes and the pulse shape remained Gaussian-like but now with $\tau_{\mathrm{pulse}} = 1\,\mathrm{ps}$. The emission wavelength of the two FP type modes was calculated by fulfilling the mode condition: $\mathrm{m} \cdot \lambda_{\mathrm{mode}}/\mathrm{n} = 2 \cdot \mathrm{L_{NW}}$. Hence, figure 5.6b depicts the calculated Fourier transform of the interference spectra of two Gaussian pulses with two central wavelengths λ_1, λ_2. Similar to the calculations in chapter 5.3.1, the two pulses are time-delayed by τ_{m} with a temporal resolution of 0.1 ps. Indeed, the FFT reveals time delay independent intensity modulations indicative of the

two FP modes. The linear sideband exhibits furthermore modulations, as depicted in the inset of figure 5.6b, that are caused by a superposition of the constant FP modulations and the linear sideband. Thus, the sideband modulations obtained in the double-pump measurement seem to be attributed to the FP modes of the NW resonator. Consistently, recent double-pump measurements on single FP mode GaAs NWs [195] do not show such sideband modulations due to the absence of different FP modes. Figure 5.6c illustrates the calculated sideband modulation period Δt_{FFT} as a function of the refractive index n (black) and versus the NW resonator length (blue). The modulation period Δt_{FFT} increases linearly for an increasing refractive index, as the spectral separation $\Delta\lambda = \lambda_2 - \lambda_1$ is enlarged. Note that the mode numbers for λ_1, λ_2 remain constant for the calculation. In addition, the modulation period depends linearly on the NW length. However, the slope $(d(\Delta t_{FFT})/dL_{NW})$ rises, when the refractive index is increased, but the slope $(d(\Delta t_{FFT})/d(n \cdot L_{NW}))$ is fixed. Figure 5.6d shows the evaluated sideband modulations of photonic CdS NWs as a function of the NW length. The graph reveals a linear slope in agreement with the calculated predictions of figure 5.6c.

The experimentally determined and the calculated FFT signals indicate some noteworthy, qualitative discrepancies. In contrast to the calculations, the sideband modulations and the time delay independent FP modulations do not occur at the same time in the measured FFT, compare figures 5.3c and figure 5.6b. Thus in figure 5.3c, the modulation of the sideband exhibits a period of $\Delta t_{FFT,\,sideband} = (0.65 \pm 0.01)\,ps$, while the constant FP modulations oscillate slower with $\Delta t_{FFT,\,FP} = (0.70 \pm 0.01)\,ps$. In general, both modulations are caused by the FP type NW cavity. Explaining this effect requires a closer look to the double-pump method: At a time delay $\tau \gtrsim 0$, the NW is still near peak inversion and the weak pump 2 merely amplifies the output pulse [38]. Note, the strong pump 1 depletes the ground state causing a reduction of the material absorption for pump 2. The absorption for pump 2 recovers for a longer time delay $\tau \gtrsim \tau_{on}$. Since the system is still inverted or even close, the absorption of pump 2 leads to the formation of the second output pulse as well as to the amplification of the first output. However, the recovered absorption seems to cause a higher mean carrier occupation for time delays $\tau \gtrsim \tau_{on}$, see chapter 5.4.2. The higher mean carrier concentration is accompanied by a lower refractive index for the NW [170,183], which becomes apparent as the reduced sideband modulation period $\Delta t_{FFT,\,sideband}$ in comparison to the constant modulation period of the FP modes $\Delta t_{FFT,\,FP}$. Taking into account that the modulation period depends linearly on the refractive index: $\Delta t_{FFT} \propto n$, the average refractive index $\overline{n}$ for $\tau \gtrsim \tau_{on}$ is $\sim 7 - 8\,\%$ smaller than for single strong pulse excitation. However, the absolute values cannot be obtained in this way.

5.4 Nanowire based laser pulses

Semiconductor NWs can generate laser pulses extremely fast. These NW laser pulses can be emitted already a few picoseconds after applying a pump pulse. Especially CdS and ZnO NWs exhibit fast onset times of $\tau^{\mathrm{CdS}}_{\mathrm{on,420\ nm}} \approx 1.9\,\mathrm{ps}$ and $\tau^{\mathrm{ZnO}}_{\mathrm{on,355\ nm}} \approx 1.0\,\mathrm{ps}$, respectively, because the exited charge carriers relax fast enforced by a strong carrier-phonon interaction. However, the light-matter interaction is inherently slow as the emission wavelength and wavelength of the electronic states differ extremely. Since the spatial scale of surface plasmon polaritons (SPP) is decoupled from the vacuum wavelength, they may enable accelerated light-matter interaction due to the optical confinement [199], as described in chapter 2.2.4. Within this chapter, fundamental laser properties such as emission wavelength, output polarization and laser power dependence of plasmonic ZnO and CdS NW lasers are demonstrated in comparison to their photonic counterparts. Both NW laser devices work at room temperature and require EHP gain. Furthermore, the double-pump technique is applied in order to unravel the accelerated gain dynamics in plasmonic ZnO NW lasers, because the Purcell effect accelerates both spontaneous and stimulated emission.

The plasmonic NW laser geometry, proposed by Oulton et al. [122], for high mode confinement accompanied by sufficient loss compensation has been introduced in figure 2.7b and its advantage over alternative plasmonic waveguide geometries has been explained in chapter 2.2.4. Plasmonic NW lasing at deep subwavelength scale using CdS NW hybrid plasmonic waveguides as in figure 2.8 has been demonstrated by Oulton et al. as well as the Purcell enhancement of their spontaneous emission rates [30], but only at low temperatures $\leq 10\,\mathrm{K}$. Figure 5.7a shows typical plasmonic (green) and photonic (black) NW room temperature spectra obtained at approximately twice their respective laser threshold. The plasmonic and photonic CdS NWs exhibit a diameter around $\sim 160-190\,\mathrm{nm}$ and $\sim 200\,\mathrm{nm}$, respectively. The stimulated longitudinal modes clearly dominate the emission spectra for both types of NW laser devices, however the plasmonic NW exhibits a suppressed superlinear kink in the power dependence ($\mathrm{x}_{0,\mathrm{plasmonic}} \gtrsim \mathrm{x}_{0,\mathrm{photonic}}$; inset of figure 5.7a) that is known from literature and an indication of enhanced spontaneous emission and reduced mode competition [30, 200]. Surprisingly, the plasmonic NW device starts to lase at almost half the threshold of the photonic NW laser, as indicated in the inset of figure 5.7a, although the plasmonic NW geometry usually suffers from high losses due to the dissipative metal. This surprising ratio might be attributed to three reasons: (i) The plasmonic CdS NW laser reveals a better optical and morphological quality than its photonic counterpart, although both stem from the same growth batch. (ii) The plasmonic NW with a length of $\sim 10.1\,\mu\mathrm{m}$ is shorter than the photonic NW with a length of $\sim 15.9\,\mu\mathrm{m}$. Due to the inhomogeneity of the pump spot the plasmonic NW might have rested in pump spot area of higher average excitation density. (iii) The lasing does not occur close to the surface plasmon energy, thus the plasmonic losses might be not sig-

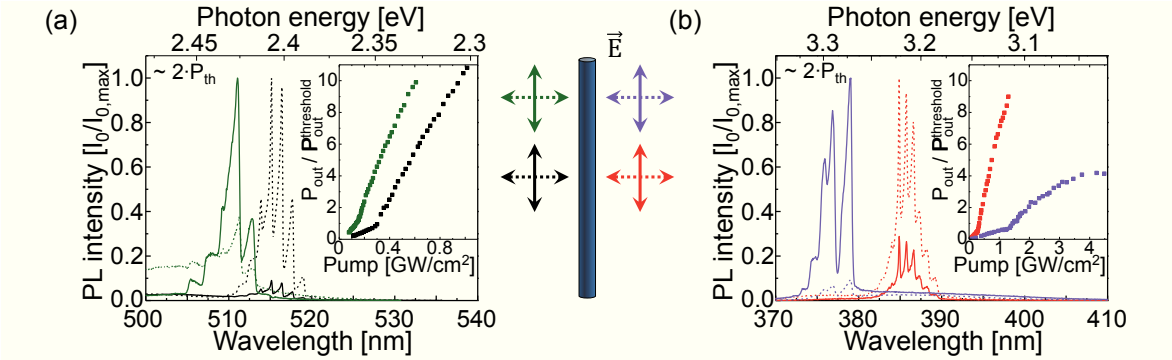

Figure 5.7: (a) Comparison of the laser emission at approximately twice the laser threshold from a plasmonic CdS NW (green) with a diameter of around $\sim 160 - 190\,\text{nm}$ and a photonic CdS NW (black) ($\sim 200\,\text{nm}$ in diameter). (b) Emission spectra of a plasmonic ZnO NW laser (purple) ($\sim 150\,\text{nm}$ in diameter) and a thicker photonic ZnO NW laser (red) with a diameter of $\sim 250\,\text{nm}$. (a,b) The emission spectra are separated into the electric field component with the polarization along the NW axis (solid line) and with the polarization perpendicular to the NW axis (dashed line). The insets depict the respective, colour coded laser characteristics: The emitted output power P_{out} normalized to the output at the threshold $P_{out}^{threshold}$ versus the pump intensity. The complete data set was obtained at $\lambda_{exc} = 355\,\text{nm}$ and at room temperature.

nificantly higher [121] than the losses in the photonic CdS NW. This is in agreement with reference [30], where individual plasmonic and photonic type CdS NW lasers with diameters between $\sim 150\,\text{nm}$ and $\sim 200\,\text{nm}$ revealed comparable thresholds. Figure 5.7b depicts the comparative spectra of plasmonic (purple) and photonic (red) ZnO NW lasers at twice the laser threshold. The plasmonic ZnO NW laser ($\sim 150\,\text{nm}$ in diameter) shows a suppressed superlinear power dependence in the ASE regime similar to the plasmonic CdS NW. Here, the threshold of the plasmonic ZnO NW is approximately five times larger than the threshold of the photonic NW ($\sim 250\,\text{nm}$ in diameter). This threshold increase for the plasmonic ZnO NW is caused by high plasmonic losses of the substrate, as the device lases close to the surface plasmon energy, see figure 5.8a.

Independent of the semiconductor gain material, ZnO or CdS, the NW lasers on the silver film emit light that is predominantly polarized along the NW axis (solid lines), while the output of the photonic NW lasers is polarized perpendicular to the NW axis (dashed lines), see figures 5.7a,b. Thus, the dominant field components of the plasmonic devices coincide with the field components of the hybrid SPP modes, as described in chapter 2.2.2. However, this is only a hint for lasing of the hybrid SPP mode, as for diameters of $\sim 160 - 200\,\text{nm}$ for CdS NWs (figure 2.8b) and $\sim 140 - 180\,\text{nm}$ for ZnO NWs (supporting information of reference [38]), respectively, the fundamental photonic-like $HE_{11a,b}$ modes might show lasing. Although the $HE_{11a,b}$ modes exhibit lower confinement, they may benefit from less plasmonic losses. These $HE_{11a,b}$ modes reveal polarized field components predominantly along the NW similar to the hybrid SPP mode. Therefore, solely a polarization analysis of the output emission seems to be not suitable in order to differentiate between a hybrid SPP mode and a confined or leaky $HE_{11a,b}$ mode [201]. However, the

polarization orientation for thicker photonic NW lasers indicates lasing of a dominant TE mode with strong field components perpendicular to the NW axis.
The lasing modes of both plasmonic NWs appear blue-shifted relatively to the respective photonic NW laser spectra, as shown in figures 5.7a,b. The blue-shift of the gain envelope arises (i) as the plasmonic cavity requires higher gain, which is provided at higher energies in the EHP [183], while significant reabsorption in the material during light propagation seems to be negligible for the plasmonic devices. (ii) Additionally, the vicinity of the semiconductor to the metal film causes a band filling / Burstein-Moss type effect, as ground state dipoles seem to absorb SPPs leading to a significant yield of excited dipole states [31].
However, the following facts strongly indicate lasing of a NW hybrid SPP mode at least for ZnO: The suppressed superlinear threshold behaviour, the required high gain due to plasmonic losses, the polarization orientation of the laser emission, and the fact that plasmonic ZnO NWs down to diameters of $\sim 120\,\text{nm}$ show lasing [118], where photonic lasing cannot occur. Unfortunately, the threshold ratio for CdS NW based lasers is contradictory and thin CdS NW devices with diameters below $\sim 160\,\text{nm}$ were not investigated within this thesis. Therefore, the following sections refer mainly to ZnO NW based lasers.

5.4.1 Dispersion relations of ZnO NW based laser sources

Plasmonic ZnO NW laser reveal approximately five times higher laser thresholds than their photonic counterparts. Considering the dispersion relation of transverse modes in the ZnO NW based laser devices enables further insights into this threshold behaviour, as both laser types are influenced by an interplay between NW material and metallic or dielectric surface, respectively. The dispersion relation of the fundamental plasmonic transverse mode for a NW diameter of 130 nm is depicted in figure 5.8a as purple line. The simulations were done by Themistoklis Sidiropoulos [118] using the permittivity of silver from Palik [202]. The resonance energy of the surface plasmon indeed overlaps with the emission spectrum of the plasmonic ZnO NW laser [118] (grey region) and the gain spectrum of the EHP in ZnO (light grey region). Furthermore, the large surface plasmon wavenumber within this gain spectrum indicates the strong optical mode confinement causing enhanced light-matter interaction in comparison to the the fundamental photonic mode dispersion (red dashed line). Figure 5.8b demonstrates that the high optical field confinement for the hybrid SPP mode occurs between the thin ZnO NW and the silver film, while the fundamental photonic mode in figure 5.8c exhibits a Gaussian like distribution within the NW cross section. The plasmonic NW lasers emit in the vicinity of the SPP resonance, where the plasmonic losses reveal their maximum, as depicted in figure 2.6b. Thus, the lasing threshold of the plasmonic ZnO NWs must exceed the value of the photonic ZnO NW lasers.

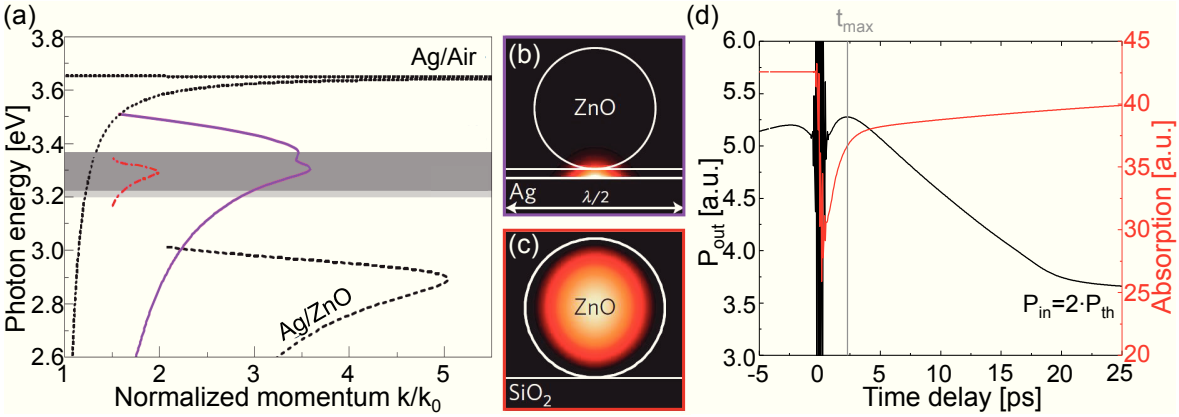

Figure 5.8: (a) Calculated dispersion relations of a silver-air (Ag/Air) interface (black dotted line), a silver-ZnO (Ag/ZnO) interface (black dashed line), a 150 nm diameter ZnO NW on SiO_2 (red dash-dotted line) and a 130 nm diameter ZnO NW hybrid plasmonic waveguide consisting of NW on LiF/Ag film ($h_{LiF} = 10$ nm). The dark grey region marks the emission region of plasmonic ZnO NW lasers and the light grey region depicts the EHP gain. Note that both overlap. (b,c) Calculated modes for the 130 nm diameter ZnO NW hybrid plasmonic waveguide and the 150 nm diameter ZnO NW on SiO_2, respectively. (d) Simulation of the output response P_{out} (black) to the double-pump excitation obtained by integrating over the cavity photon number from figure 5.1e at each time delay. The excitation power P_{in} was set to twice the laser threshold P_{th}. The simulated material absorption (red) indicates the gain depletion for 0 ps $< \tau <$ t_{max} and the subsequent recovery during the NW laser pulse.

5.4.2 Time-integrated double-pump response and pulse width

A further investigation of the accelerated plasmonic NW laser dynamics requires the application of the double-pump technique that was introduced in chapter 5.3.1. Here, not only the spectral response needs to be considered, but additionally the time-integrated intensity response was examined. The black line in figure 5.8d shows the time-integrated output power P_{out} as a function of the time delay τ. The curve was obtained by integrating the cavity photon number s, as simulated in figure 5.1e, over the whole time scale t for each time delay step. The simulations were performed using the laser rate equations of chapter 3.5, but the phase transition from excitonic decay to EHP decay was not included. For time delays around $\tau \approx 0$ ps, the output power strongly oscillates caused by the interference of the two impinging pump pulses. For positive time delays the response is divided into three regimes: (i) When the pump 2 approaches shortly after the pump 1 at $\tau \gtrsim 0$ ps, the laser system still remains close to its peak population, such that pump 2 just amplifies the output pulse generated by pump 1. The material absorption of the NW depicted as the red curve in figure 5.8d significantly decreases due to depletion of the ground state by the strong pump 1. (ii) The NW absorption of the weak pump 2 recovers for longer time delays $\tau > 0$ ps. As the laser is still inverted, a second NW laser pulse can be generated and the first pulse can be amplified. Note, both NW output pulses merge for certain time delays. Thus, the time-integrated output power increases in this time regime up to a maximum at a time delay denoted as t_{max}. Simultaneously, the

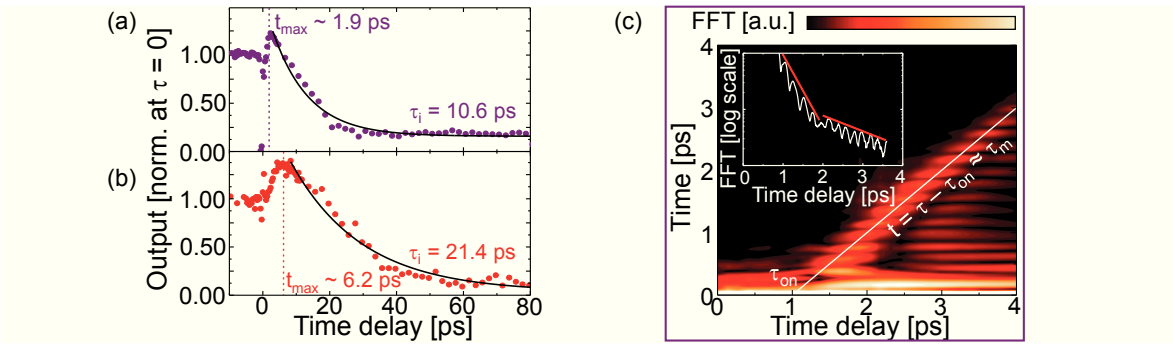

Figure 5.9: (a,b) The total double-pump P_{out} response of NW lasers versus the time delay τ of (a) the plasmonic ZnO NW from figure 5.7b and (b) a photonic ZnO NW of $\sim 200\,nm$ diameter. The data was normalized to the P_{out} value at $\tau = 0\,ps$. Pump 1 and pump 2 exhibited values of twice and 0.2 times the threshold value P_{th}, respectively. The measured curves clearly reproduce the simulated curve from figure 5.8d with the characteristic time t_{max} and the decay constant τ_i. (c) The Fourier transform (FFT) of each interference spectrum obtained by the double-pump measurement of the plasmonic NW shows the typical linear sideband with $\tau_{on} \approx 1.1\,ps$. The inset depicts the linescan along the sideband (white line) with the amplitude decay revealing a transition from fast to slow decay at $\sim 1.9\,ps$. This coincides with t_{max} from (a), as both indicate the time, when the first output pulse is terminated.

absorption recovers almost to its initial value at t_{max}. Although not all carriers occupy the ground state again at t_{max}, the population inversion is depleted. The first output pulse is therefore nearly terminated at the time t_{max}. (iii) For much longer time delays $\tau \gg 0\,ps$, the remaining population of the excited state decays with the spontaneous recombination rate of the semiconductor. The NW can still generate a second output pulse until the remaining carrier population has decayed so far that the weak pump 2 is not sufficient to induce carrier inversion again. The output power reveals therefore an exponential decay in this third time regime. In general, as the time t_{max} indicates the termination of the NW output pulse in the double-pump measurement, the pulse width t_{pulse} can be estimated by: $t_{pulse} \lessapprox t_{max} - \tau_{on}$.

5.4.3 Ultrashort laser pulses of plasmonic lasers

In order to demonstrate the acceleration of NW output pulses by coupling to the hybrid SPP modes, several photonic and plasmonic NW laser devices were investigated in the diameter range between $\sim 140\,nm$ and $200\,nm$ via the double-pump technique. Figures 5.9a and 5.9b show typical NW output power characteristics as a function of the time delay for a plasmonic ZnO NW of $\sim 150\,nm$ diameter and a photonic ZnO NW of $\sim 200\,nm$ diameter, respectively. Both double-pump responses coincide qualitatively with the expected behaviour in figure 5.8d. The output curves of both laser devices exhibit strong oscillations for time delays $\tau \approx 0\,ps$, due to the interference of pump 1 and pump 2. However, the evaluated characteristic times t_{max} and the constants of the exponential decay τ_i differ significantly depending on the type of laser device. The enhanced spontaneous recombination in the plasmonic NW device becomes apparent for $\tau > t_{max}$, as

the second output pulse generated by the weak pump 2 appears for shorter time scales than in the photonic device. Hence, the decay constant τ_i for the plasmonic device is decreased compared to the photonic device due to the Purcell effect. Since spontaneous and stimulated recombination are fundamentally linked, as shown in equation 2.15, the laser pulse width is reduced as well. Thus, the plasmonic NW laser pulse is terminated much earlier, already at $\mathrm{t_{max}} \sim 1.9\,\mathrm{ps}$, while the photonic NW laser exhibits a longer value of $\mathrm{t_{max}} \sim 6.2\,\mathrm{ps}$. This unambiguously proves the enhanced stimulated recombination rate and the acceleration of the laser output pulses to ultrashort time scales by coupling the light field to SPP modes.

Furthermore, the double-pump response of the plasmonic NW device in figure 5.9a was spectrally resolved similar to the evaluation in chapter 5.3. Figure 5.9c shows the respective Fourier transform of the double-pump interference spectra with the characteristic linear sideband and a laser onset time of $\tau_\mathrm{on} \approx 1.1\,\mathrm{ps}$. As mentioned earlier, the FFT sideband contains insights about the temporal characteristic of the two output pulses as: $\mathrm{FT}^{-1}\left\{\Delta \mathrm{I}\left(\omega\right)\right\} = \mathrm{E}_1\left(-\mathrm{t}, \tau\right) * \mathrm{E}_2\left(\mathrm{t} - \tau_\mathrm{m}, \tau\right)$ [118]. For time delays $\tau_\mathrm{on} \leq \tau \leq \mathrm{t_{max}}$, when two output pulses are emitted, both consequently compete for optical gain. This becomes apparent from the bi-exponential decay of the linear sideband, as depicted in the inset of figure 5.9c. Initially, the gain is depleted faster, as the two output pulses compete for gain, whereas the gain decay subsequently slows down, as only the second output pulse depletes the residual inverted carriers. Indeed, the transition from fast to slow decay occurs at $\sim 1.9\,\mathrm{ps}$, such that it coincides with the $\mathrm{t_{max}}$ value from figure 5.9a proving that the first output pulse is terminated at this time. Furthermore, this particular plasmonic ZnO NW exhibits an ultrafast output pulses of $\mathrm{t_{pulse}} \approx 800\,\mathrm{fs}$, whereas the photonic NW pulse is $\sim 5\,\mathrm{ps}$ long.

Comparing the plasmonic and photonic ZnO NW lasers in figure 5.9 has already unraveled significant differences in the stimulated and spontaneous recombination dynamics. Measuring further NW laser devices manifested this trend. The temporal response of five plasmonic and seven photonic NW devices are depicted in figure 5.10a. The data show no significant diameter dependence. Remarkably, the time at which the double-pump response is maximized $\mathrm{t_{max}}$, is much faster for all plasmonic NW laser devices. The average value decreases from $\overline{\mathrm{t_{max}}} \approx 6.0\,\mathrm{ps}$ for photonic ZnO NW lasers to $\overline{\mathrm{t_{max}}} \approx 1.6\,\mathrm{ps}$ for plasmonic NW lasers, respectively. Instead, the laser onset time remains almost at a constant value of $\overline{\tau_\mathrm{on}} \approx 1\,\mathrm{ps}$ independent of the optical system and diameter, as described in chapter 5.3. Thus, the laser onset time is indeed a material driven parameter that is not significantly tunable by modifying the optical system, e.g. by the Purcell effect. In general, the laser pulses can be tuned from extremely fast $\sim 5\,\mathrm{ps}$ for thin photonic ZnO NWs (diameter $\lesssim 200\,\mathrm{nm}$) into the ultrafast subpicosecond regime of $\sim 600 - 800\,\mathrm{fs}$ by extreme mode confinement of the hybrid plasmonic ZnO NW mode emitting near the SPP resonance.

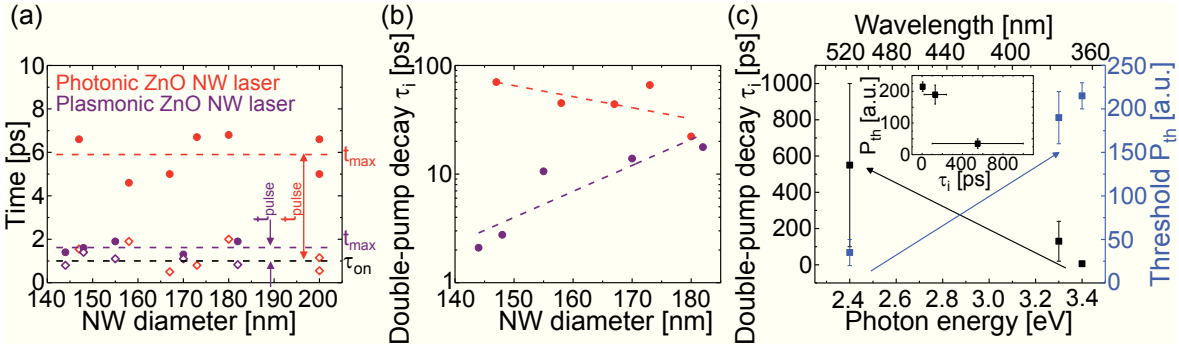

Figure 5.10: (a) Characteristic temporal parameters τ_{on} (open diamonds) and t_{max} (full circles) for photonic (red) and plasmonic (purple) ZnO NW lasers. Pump 1 and pump 2 are set to twice and 0.2 times the threshold value P_{th}, respectively. The black dashed line shows the average value of τ_{on}, which does not depend on the optical configuration. The red (purple) line indicate the average t_{max} for photonic (plasmonic) ZnO NWs. The average pulse width is obtained by: $t_{pulse} \lessapprox t_{max} - \tau_{on}$. (b) The double-pump decay τ_i for plasmonic (purple circles) and photonic (red circles) ZnO NWs. The double-pump conditions are similar to (a). The dashed lines indicate the trend of the experimental data. (c) The experimentally determined span for τ_i (black) and the lasing threshold (blue) of photonic CdS ($E_g = 2.4$ eV), ZnO ($E_g = 3.3$ eV) and GaN ($E_g = 3.4$ eV) NWs, respectively. The inset reveals that materials with slow carrier recombination allow small lasing thresholds.

5.4.4 Double-pump decay versus population inversion

Besides studying the accelerated stimulated dynamics of plasmonic lasers, the comparison of the plasmonic with the photonic NW laser in figures 5.9a,b has brought insights into the material dynamics after output pulse generation when the population inversion is depleted. The duration, which the material can remain close to inversion, such that a second NW laser pulse can be generated by the weak pump 2, is determined by the double-pump decay τ_i. Figure 5.10b shows the τ_i value for a number of photonic (red data points) and plasmonic (purple data points) ZnO NW lasers. The effect of the increasing SPP confinement leads to an acceleration of the double-pump decay τ_i with decreasing nanowire diameter. In contrast, the trend for the photonic NWs is not that clear. The photonic NWs seem to become slower with decreasing diameter, which might be attributed either to improved material quality or the loss of photonic mode confinement. Typical τ_i values for photonic ZnO NWs are in the order of several tens of picoseconds corresponding to the recombination of carriers in the electron-hole plasma [147, 203]. An improved optical quality in thin NWs might cause an enhanced carrier lifetime in the EHP due to an absence of defects.

The material dynamics by means of the double-pump decay are significantly accelerated for plasmonic NW lasers due to the Purcell effect. The increase in SPP confinement for thin NWs speeds up the dynamics to ultrashort values of $\tau_i \lessapprox 2$ ps, while the time required to establish a laser pulse stays almost constant at $\tau_{on} \approx 1$ ps. Thus, the ultrafast laser dynamics suffer from an important limitation: If the plasmonic devices become too fast to enable the build-up of an population inversion, no laser light can be generated.

Consequently, no plasmonic ZnO NW laser devices with diameters below $\lesssim 120\,\mathrm{nm}$ could be reported so far [38]. Establishing faster and smaller devices therefore demands an appropriate choice of the gain material in order to avoid this relation: $\tau_{\mathrm{on}} \gtrsim \tau_{\mathrm{i}}$, as τ_{on} cannot be engineered by the Purcell effect. However, ZnO seems to exhibit the fastest τ_{on} among the typically studied semiconductors, thus the plasmonic ZnO NW laser possibly achieve the maximum possible speed, at which such a semiconductor laser can be operated. Note that smaller NW devices with diameters of $\gtrsim 60\,\mathrm{nm}$ were certainly reported in literature emitting laser light away from the SPP resonance by exploiting different semiconductors as gain material [30, 123].
The fast carrier recombination in terms of the double-pump decay τ_{i} substantially limits the performance of a NW based coherent light source. Hence, the carrier recombination influences the lasing threshold. Figure 5.10c shows the decay constant τ_{i} (black data points) and the lasing threshold $\mathrm{P_{th}}$ (blue data points) for photonic NW lasers made of CdS emitting at $\sim 2.4\,\mathrm{eV}$, ZnO at $\sim 3.3\,\mathrm{eV}$ and GaN at $\sim 3.4\,\mathrm{eV}$, respectively. The error bars reflect the variety of different values for different NW devices. Both quantities reveal the opposite behaviour, the threshold value increases from CdS to GaN, while the double-pump decay constant decreases. This is even more evident in the inset of figure 5.10c. The plot unambiguously indicates that a long carrier lifetime tends to allow a lower lasing threshold, because less pumping power is required in order to invert the laser system. Furthermore, the carrier density for the transition into the EHP regime is overcome more easily for longer carrier lifetimes.

5.4.5 High excitation effect - Band filling in plasmonic lasers

It has been shown in chapter 5.3 that the photonic lasing modes broaden in the time-integrated spectra at very high excitation densities $\gtrsim 2 \cdot \mathrm{P_{th}}$. Plasmonic ZnO and CdS NW lasers exhibit similar effects, as shown in figures 5.7a,b and 5.11. As explained earlier, this effect is based on the significant change of the refractive index during the laser output pulse, when the carrier population is depleted. In addition, another feature occurs in the high excitation spectra of plasmonic NWs: At high pump intensities of $\sim 4 \cdot \mathrm{P_{th}}$, the lasing spectra of plasmonic ZnO and CdS NWs in figures 5.11a,b broaden towards the high energy side in contrast to the spectra of photonic NW lasers, compare figure 5.1a. The emission shape is very asymmetric revealing a smooth shape on the high energy side, whereas the intensity drops abruptly at the low energy side. Even a clear assignment of FP modes becomes complicated, especially for thin ZnO NWs such as in figure 5.7a.
The blue-shift of the plasmonic lasing spectra with respect to their photonic counterparts in figure 5.7 can be attributed to the enhanced plasmonic losses and band filling. The conduction (and valence) band is occupied by carriers following a thermal distribution, which is determined by a Fermi function. Indeed, the smooth shape at the high energy side of the plasmonic lasing spectrum (at four times the threshold) is attributed to band filling, as the emission intensity $\mathrm{I_0}$ fits to the Fermi function by: $\mathrm{I_0} \propto \left(\mathrm{e}^{(\mathrm{E\text{-}\mu})/\mathrm{k_B T}} + 1\right)^{-1}$.

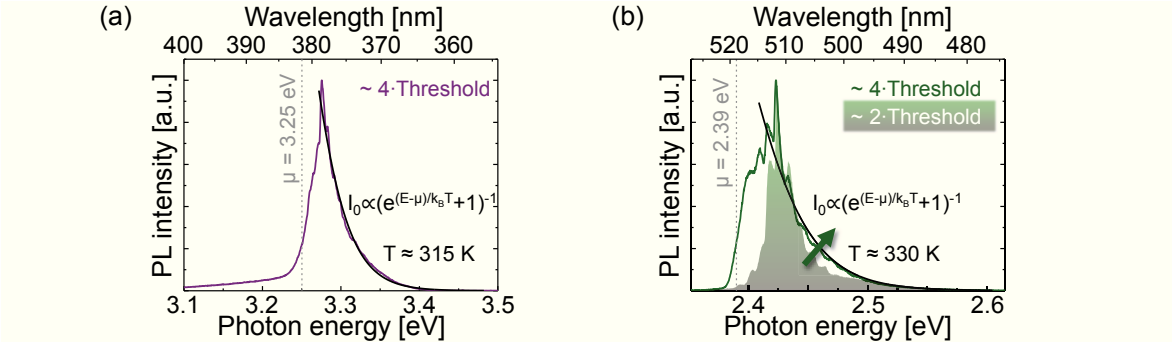

Figure 5.11: (a) Lasing spectrum of a 170 nm diameter plasmonic ZnO NW excited at ~ 4 times the laser threshold. The high energy side is fitted using the Fermi function in order to verify the band filling in highly excited plasmonic NWs. (b) Lasing spectra of a $\sim 160 - 190$ nm wide plasmonic CdS NW pumped at $\sim$ twice (shaded spectrum) and ~ 4 times (green line) the threshold. The arrow indicates the blue-shift at the high energy side in addition to the overall broadening. The lasing spectrum at $\sim 4 \cdot P_{th}$ is fitted using the Fermi function. (a,b) Both plasmonic laser devices exhibit a thermal occupation of carriers with $T \sim 310 - 340$ K at the high energy side.

Here, E is the energy, μ reflects the chemical potential, k_B is the Boltzmann constant and T the (carrier) temperature. The chemical potential μ is defined as the difference of the quasi Fermi energies E_F^e and E_F^h in the conduction and valence band, respectively, as schematically depicted in figure 2.4a. The Fermi function is fitted to the high energy side lasing spectrum of a 170 nm wide plasmonic ZnO NW in figure 5.11a and of a $\sim 160 - 190$ nm wide plasmonic CdS NW, respectively. Both plasmonic devices reveal qualitative similar features at four times the laser threshold, thus the band filling effect at such high excitation indeed occurs due to the vicinity of the metal film [31]. The spectra follow the Fermi function quite well for small intensities, while the Fermi function starts to deviate for energies when the lasing modes dominate the emission. The temperature of the excited state carriers can be derived from the fitting with $\sim 310 - 340$ K. Thus, the carrier temperature seems to be nearly independent of the gain material. Since the temperature value corresponds approximately to the ambient temperature, the carriers have thermalized apparently completely prior to radiative recombination. The chemical potential μ exhibits values of ~ 3.25 eV for ZnO and ~ 2.39 eV for CdS, respectively. At high excitation intensities, band gap renormalization as well as the blue-shift of chemical potential occur due to large carrier concentrations as two competing effects [58, 204]. Therefore, a shift of the chemical potential μ can be hardly predicted. However, the fitting for both semiconductors reveal μ values that are significantly red-shifted in comparison to the free exciton emissions of ~ 3.31 eV in ZnO and ~ 2.46 eV in CdS, respectively. Since the band gap is obviously smaller than the chemical potential with $E_g < \mu$, as shown in figure 2.4a, both plasmonic lasers unambiguously are exposed to a large band gap renormalization indicating the EHP induced stimulated process. Nevertheless, the Fermi-like distribution at the high energy side of the lasing spectra accompanied by its increased blue-shift with increasing excitation indicate the state filling effects of the plasmonic NWs.

5.5 Summary

In this chapter, the ultrafast laser dynamics of semiconductor NW based coherent light sources such as laser onset time, pulse width and gain depletion have been accessed by exploiting a double-pump measurement method [118]. The double-pump approach itself makes use of the nonlinearity of the laser process. By evaluating the spectrally acquired double-pump response, the laser onset time τ_{on} has been determined for several NW laser devices made of different gain materials and in different optical configurations. In addition, the time-integrated intensity response measures the time at which the emitted NW laser pulse is terminated as well as the radiative decay dynamics following this NW output pulse.

The laser onset time τ_{on} is a material dynamics driven parameter, which is independent of the NW diameter or the optical system [37]. Since the onset time depends on thermalization and interaction processes after the photoexcitation, the material dependent carrier-phonon interaction strengths give rise to the different values in CdS, ZnO and GaN NW lasers. Among this three materials, the ZnO NW lasers generate output pulses at the fastest time scales in the order of $\sim 0.7 - 1.1\,\mathrm{ps}$. This ultrafast response is due to the exceptional strong carrier-phonon coupling in ZnO. Other semiconductor NW lasers such as the typically investigated ZnS, ZnSe, CdSe, InGaN and GaAs NWs most probably switch on slower, because they suffer from a weaker carrier-phonon interaction than ZnO. Thus, the carrier relaxation is significantly slower. However, the adjustment of the pump energy is an efficient way to tune the the onset time of a particular semiconductor gain material, as this in-/decreases the excess energy of the carriers. This was proven using photonic CdS NW laser devices.

While the turn on time τ_{on} of a NW laser is determined by the gain material, the pulse width depends on spontaneous and stimulated emission processes and could be accelerated by changing the optical configuration. Semiconductor NWs separated from a silver surface by a 10 nm thin LiF layer form a hybrid plasmonic waveguide, which is referred to as **plasmonic** NW laser. The laser light generated in ZnO NWs coupled efficiently to the SPPs of the silver film in this configuration. Since plasmonic ZnO NW lasers operate near the surface plasmon resonance, the high momentum of the plasmonic transverse mode led to an efficient Purcell enhancement of the spontaneous and stimulated emission rate. Hence, the temporal pulse width could be reduced from $t_{pulse} \approx 4 - 5\,\mathrm{ps}$ for photonic ZnO NWs down to $t_{pulse} \approx 600 - 800\,\mathrm{fs}$ for plasmonic NWs. However, besides the benefit of achieving ultrafast laser dynamics, the plasmonic confinement causes a severe size limitation prohibiting plasmonic lasing for thin sub-120 nm wide ZnO NWs [38]. The enhanced, too fast carrier recombination does not allow the build-up of population inversion. However in any case, plasmonic ZnO NW lasers reveal the fastest on-off switching speeds. A further acceleration requires a proper choice of gain material and most likely new optical configurations going beyond an elongated wire structure.

6 Mode switching in ZnO nanowire lasers

This chapter discusses the transverse mode properties and the angular emission of single ZnO NW lasers of different diameters. It highlights the fundamental connection between transverse mode propagation and both laser output dynamics and emission characteristics. The measurements of the angular emission patterns of several ZnO NWs were carried out in collaboration with Max Riediger (see his master's thesis [41]) using the head-on measurement setup. The head-on setup was established in collaboration with Daniel Ploss and Arian Kriesch (University Erlangen-Nuremberg). The measurements of the NW output dynamics were performed in collaboration with Dr. Themistoklis Sidiropoulos and Dr. Rupert Oulton (Imperial College London). Optical simulations by means of conventional FDTD as well as dynamical simulations applying the combined FDTD and semiconductor Bloch equation approach were performed by Robert Buschlinger and Prof. Ulf Peschel at the Institute of Condensed Matter Theory and Solid State Optics, University of Jena. These results were analyzed and interpreted in close collaboration in order to compare experiment and simulation. Parts of this chapter are published in references [39] and [40].

6.1 Motivation

The availability of coherent light sources on the nanoscale have brought up visionary concepts of integrated photonic circuits, nanospectroscopy and nanosensing [15]. However, the requirements of these concepts go far beyond the simple availability of coherent monochromatic radiation on the subwavelength scale. The photons emitted by these nanowire based lasers must be efficiently captured and precisely coupled to adjacent nanophotonic components and waveguides. Thus, a thorough understanding and control over the fundamental emission properties and the underlying optical lasing modes is required in order to exploit the nanowire light sources for the envisaged ideas. These fundamental emission properties especially include the angular emission distribution, the polarization information by means of the Stokes parameters as well as the respective temporal output dynamics. To this end, suitable experimental techniques and simulation methods must be developed and correlated in order to thoroughly characterize the emission of single NW laser devices.

Photonic ZnO NW lasers are a suitable model system for such a combinatory study applying the developed experimental techniques and simulation methods, as they provide robust ultraviolet laser emission at room temperature due to the optical gain from the electron-hole plasma. Furthermore, their morphology/diameter is controllable by the growth conditions, such that the emission distribution and hence the operating transverse mode(s) can be precisely tuned. Using an appropriate measurement method the respective emission distribution can then be directly imaged for NW lasers of different diameter. Here, the emission intensity from individual NW lasers below and above the

single transverse mode cutoff is sampled using the head-on setup (see chapter 3.4.2) and correlated to the respective temporal dynamics that are measured using the double-pump approach (see chapters 3.4.2 and 5). The head-on measurement relies on a back focal plane polarization imaging technique (compare figure 3.3c) which was applied so far only to NW arrays in the spontaneous emission regime [205, 206]. Moreover, the findings of the mode imaging must be qualitatively compared to the results of the integrated FDTD and semiconductor Bloch equation model (see chapter 3.5 and reference [150]) in order to verify this dynamical simulation model.
Isolating a single transverse lasing mode is crucial for a defined laser beam profile enabling efficient coupling to adjacent optical components without parasitic radiation. The selection of specific transverse modes is a challenging task as these are determined by the nanowire cross section [168]. Thus, the verified simulation model must be used to predict a NW morphology suitable for mode filtering.

6.2 Mode dependent laser emission properties

The single NW (lasing) measurements in the previous chapters were carried out using a conventional µPL geometry, such that excitation and luminescence collection occurred under normal incident to the sample surface. This prevents a thorough characterization of the laser emission from the NW end facet, as it obscures the angular distribution and polarization of the lasing mode in the far field. In this chapter, the head-on measurement setup, as introduced in chapter 3.4.2, is applied in order to avoid these limitations and directly access the laser emission from the end facet.

6.2.1 Spectral emission features measured head-on

Initially, the lasing performance of each individual ZnO NW resting partially on the substrate was investigated by means of spectrally detecting its laser emission from the loose end facet. Figure 6.1a shows exemplary power dependences of a ZnO NW with a diameter at its thinnest of $\sim 140 - 150\,\mathrm{nm}$ using pump pulses of 10 ns at 355 nm with a repetition rate of 100 Hz. The electric field polarization of the pump beam was adjusted either perpendicular (blue data) or parallel (red data) relatively to the NW axis. Both data can be fitted by a theoretical multimode laser model [105] with similar parameters x_0, but the laser threshold is approximately $\sim 20\,\%$ smaller for the pump light polarized perpendicular to the NW axis. The pump intensity and hence the threshold intensity exhibit an error of $\sim 5-10\,\%$. However, polarization sensitive absorption was demonstrated and explained in reference [39] for CdS NW lasers. Therein, the calculated absorption coefficient of CdS NWs (refractive index at 3.49 eV $n_{CdS} = 2.5 + 0.4i$) revealed a more efficient absorption of perpendicular polarized pump light for CdS NW diameters below $\sim 190\,\mathrm{nm}$. Zinc oxide shows a comparable refractive index of $n_{ZnO} \approx 2.20 + 0.45i$ at 3.49 eV [170] indicating that

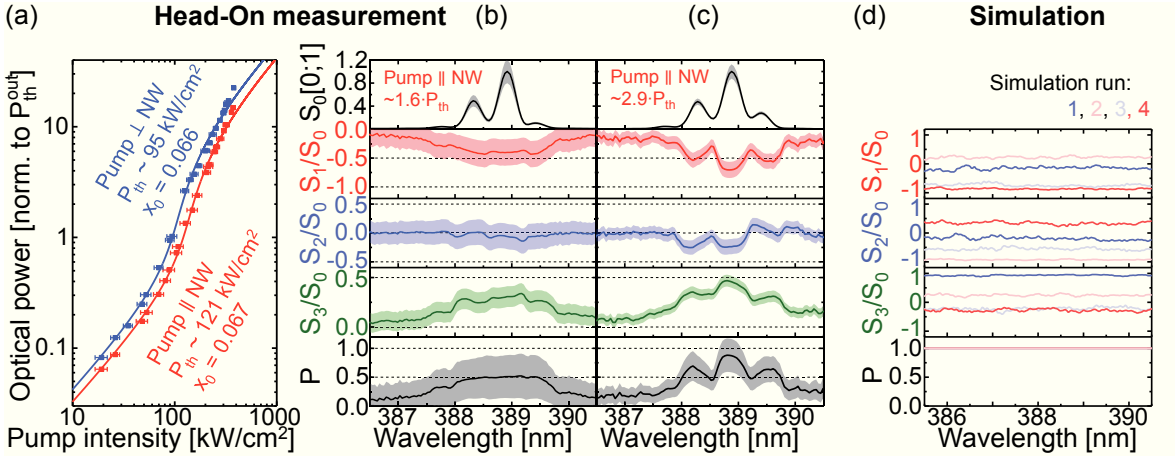

Figure 6.1: (a) The NW laser characteristics of a ZnO NW (thinnest diameter $\sim 140-150$ nm; see figure 6.3a) depicting the optical power as a function of the pump intensity with the electric field polarized parallel (red) or perpendicular (blue) to the NW axis. The data can be fitted using a multimode laser model [105]. The threshold is smaller for perpendicular polarized pump light due to a more efficient absorption. (b,c) Normalized Stokes parameter S_0 - S_3 and the degree of polarization P versus the emission wavelength for the pump intensity equal to ~ 1.6 times (b) and ~ 2.9 times (c) the threshold value. (d) Results of four simulation runs of lasing of a 140 nm wide ZnO NW surrounded by air using the dynamical semiconductor Bloch equation and FDTD approach. The plot shows the normalized Stokes parameters and the degree of polarization as a function of the emission wavelength. The emission is fully polarized, whereas the Stokes parameters are different for each simulation run.

a similar trend for the excitation/absorption anisotropy can be expected for thin ZnO NWs as for CdS NWs. Thus, the smaller threshold for perpendicular polarized pump light (blue) than for parallel polarized pump light (red) is very likely caused by the more efficiently absorbed perpendicular polarized excitation.

The Stokes parameters were measured by means of the approach described in reference [145] using the head-on setup. Figures 6.1b,c depict the spectrally resolved Stokes parameters (S_0 - S_3) for two pumping conditions well above the threshold. The lasing modes unambiguously dominate the emission spectra, as indicated by the overall intensity parameter S_0, whereas the spontaneous emission is almost negligible but intense enough for a reasonable evaluation. The normalized Stokes parameters S_i/S_0 of all stimulated longitudinal modes reveal the similar trend, as they very likely originate from the same transverse mode. The lasing modes are predominantly vertically polarized (with respect to the NW end facet and propagation direction) with contributions of circular polarization. The magnitude of S_i/S_0 is clearly correlated to the intensity S_0 of the stimulated emission, as the highest absolute values $|\ S_i/S_0\ |$ occur for the most intense mode. Furthermore, the spontaneous emission reveals the smallest Stokes parameters, because it is almost unpolarized, such that the degree of polarization drops to $P = 15 \pm 10\,\%$. The degree of polarization P of the longitudinal modes increases with increasing pump intensity from $\sim 50\,\%$ at ~ 1.6 times (figure 6.1b) to $\sim 88\,\%$ at ~ 2.9 times (figure 6.1c) the threshold. Thus, the most intense mode is nearly fully polarized with $P \sim 88\,\%$ at the

highest pump intensity.
Comparative theoretical studies were performed by applying the dynamical simulation method by R. Buschlinger [150]. A ZnO NW laser of a similar diameter ($\sim 140\,\mathrm{nm}$) as in the experiment and completely surrounded by air was pumped into the lasing regime in the simulations. Subsequently, the normalized Stokes parameters S_i/S_0 of the obtained lasing spectrum were recorded and plotted in figure 6.1d for four different simulation runs. The stimulated emission is always fully polarized as expected. Thus, the experimentally determined degree of polarization for the lasing modes coincides almost with the simulation results. However, the simulated Stokes parameters S_i/S_0 are different for every simulation run, as there seems to be no stable mode condition for a NW laser surrounded by air. In contrast, the experimentally investigated ZnO NW laser exhibits reproducible polarization features, as shown in figures 6.1b,c. The substrate disturbs the cylindrical symmetry of the NW waveguide selecting a dominant transverse mode propagating in thin ZnO NWs. However, applying only the spectral measurement of the polarization features does not allow to get all necessary insights in order to identify the lasing transverse mode, as the data is averaged over all emission angles collected by the high NA objective, as shown in chapter 3.4.2.

6.2.2 Transverse modes and mode switching

It has been shown in chapter 2.1.6 that NWs are efficient multimode waveguides. The propagating transverse waveguide modes can be calculated numerically for a static NW refractive index by solving Maxwell's equation using FDTD simulations. Thus, the FDTD results typically represent the conditions of a passive waveguide without any material dynamics such as gain/absorption and many-body effects. Figure 6.2a shows the effective index n_{eff} at 385 nm wavelength as a function of the NW diameter for the six lowest order modes propagating in a NW with circular cross section surrounded by air and lying on a dielectric SiO_2 substrate. The refractive index of the NW was set to $n = 2.2$ in order to simulate highly excited ZnO with a carrier density well above the Mott density n_M according to reference [183]. The ZnO NW waveguide exhibits the multimode cutoff for diameters below $\sim 200\,\mathrm{nm}$, as only the fundamental HE_{11} mode(s) are guided efficiently. The fundamental HE_{11} modes exhibit a cutoff diameter of $\sim 130 - 140\,\mathrm{nm}$. Since NW lasing depends strongly on the mode index and mode reflectivity, calculations in reference [115] predicted a change of the transverse lasing mode from the fundamental HE_{11} mode to a higher order mode around the multimode cutoff occurring at $\sim 200\,\mathrm{nm}$ in highly excited ZnO NWs.
Thick ZnO NWs with diameters above $\sim 260\,\mathrm{nm}$ theoretically support at least six transverse modes. Figure 6.2b shows the simulated field distributions (red) and far field patterns (green) of the four lowest order modes in a 300 nm wide ZnO NW that is completely surrounded by air (Note, the HE modes are degenerated). The fundamental HE_{11} mode reveals a linear polarization at a certain position in time and space and the far field pat-

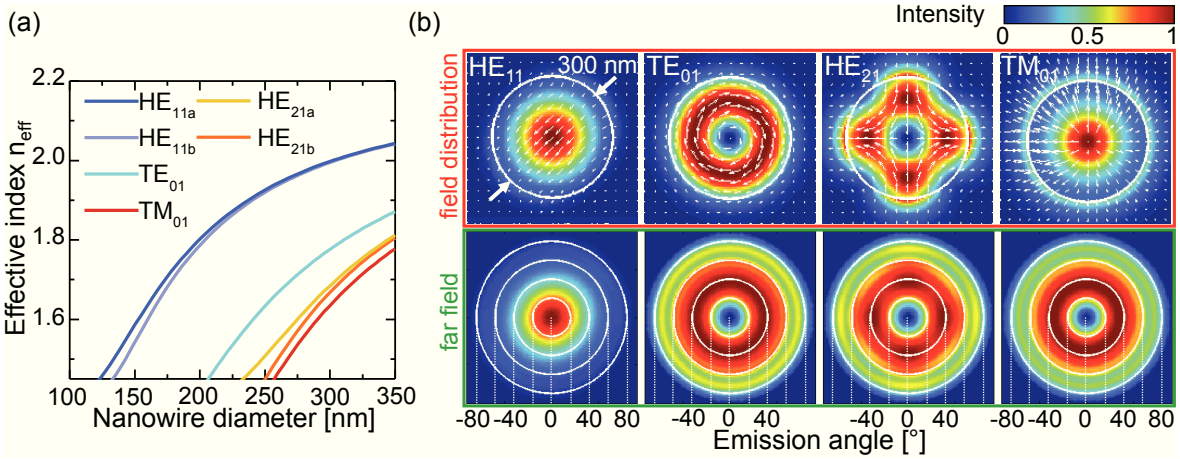

Figure 6.2: (a) The effective mode index n_{eff} versus the NW diameter of the six lowest order modes propagating in a ZnO NW with a circular cross section surrounded by air and lying on a dielectric SiO_2 substrate. The refractive index of ZnO was set to n $\sim$ 2.2 in order to adapt the condition of highly excited ZnO according to reference [183]. The multimode cutoff occurs at $\sim$ 200 nm diameter. Here, the fundamental HE_{11} mode(s) are not degenerated because of the influence of the substrate. (b) Calculated field distributions (red) and far field patterns (green) of the four lowest order transverse modes in a 300 nm wide ZnO NW surrounded by air. Note, the HE modes are degenerated, as the substrate is absent. Among these modes, only the fundamental HE_{11} mode reveals the most intense emission along the NW axis.

tern is given by a Gaussian-like beam profile. The higher order modes show azimuthally polarized (TE_{01}), pillow-like (HE_{21}) and radially polarized (TM_{01}) electric field distributions. Furthermore, the high order modes can be unambiguously distinguished from the fundamental mode by their far field patterns, as they reveal an emission minimum in the center and an intense emission rim at high angles. Thus, only the fundamental HE_{11} mode emits along the NW axis.

6.2.3 Far field emission of lasing nanowires

Usually FDTD simulation methods were applied in order to determine the transverse lasing mode [24, 114]. Only few reports deal with experimental approaches to determine the lasing mode in individual semiconductor NWs [207, 208]. However, these approaches "suffer" from rather strict requirements such as the need for e.g. the interference of FP modes between the two end facets and additional numerical simulations. In contrast, the head-on technique is capable of directly imaging the laser mode distribution of different NW lasers. Throughout this chapter, the results of thin ZnO NWs with diameters below the multimode cutoff are colour coded in green, while the results of thick multimode NWs are highlighted in orange, respectively.

6.2.3.1 Fundamental mode lasing

Figure 6.3a shows the SEM image of the ZnO NW with a diameter at its thinnest of $\sim$ 140 − 150 nm, which was already investigated in figures 6.1a-c. Important morpho-

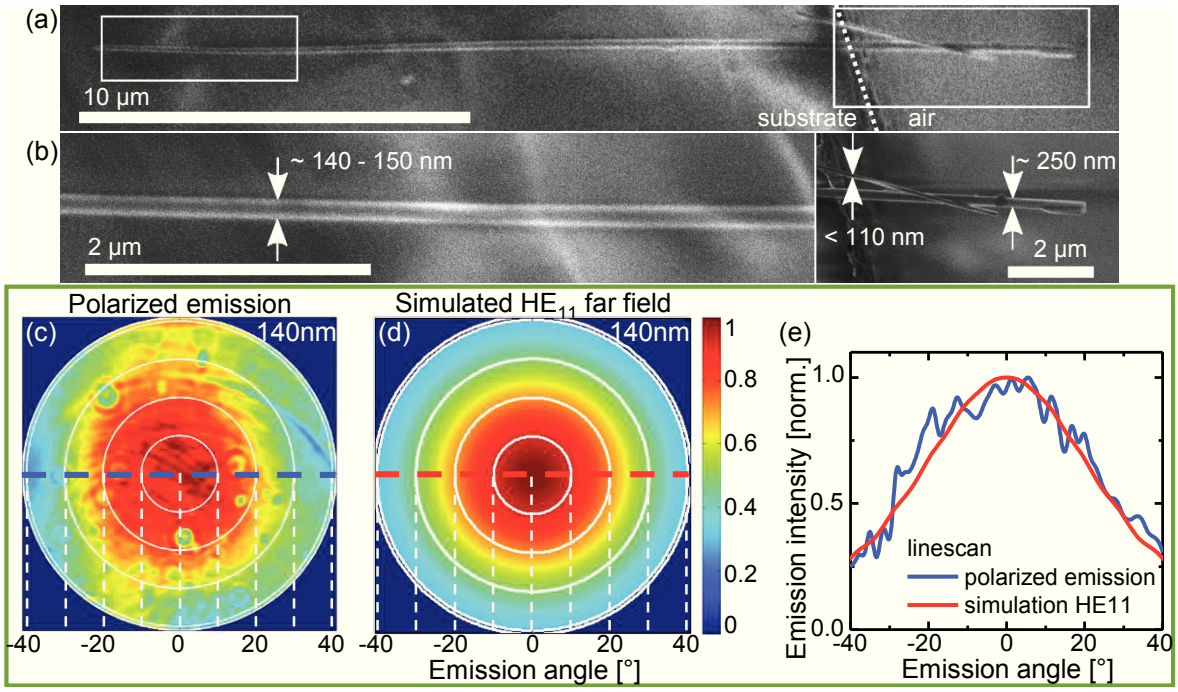

Figure 6.3: (a) The SEM image depicts a thin ZnO NW with a diameter between $140-150$ nm and $\sim$ 250 nm and a length of 25.6 µm, which is partially suspended in air. (b) The SEM images show significant morphology features marked in (a) as well as a second parasitic NW. The parasitic NW does not disturb the measurement, since it is too small to show lasing. (c) Angular resolved polarized laser emission I_{Pol} of the ZnO NW laser depicted in (a). The pump intensity was set to $\sim$ 3 times the laser threshold. (d) Far field pattern of the HE_{11} mode simulated for a respective ZnO NW with 140 nm diameter and circular cross section. The thin ZnO NW laser emits the fundamental HE_{11} mode, as measured and simulated far field patterns show good coincidence. (e) The horizontal linescans of the measured (blue) and the simulated (red) far field distribution qualitatively coincide.

logical properties are depicted in figure 6.3b. There is a second, parasitic NW lying on top of the investigated NW. Lasing of this parasitic NW is prevented by the much too small diameter, thus this NW does not significantly disturb the measurement. According to the calculations in figure 6.2a, this particular ZnO NW was expected to exhibit fundamental mode operation of the HE_{11} mode. The angular resolved fully polarized part of the NW emission I_{Pol} is presented in figure 6.3c. The plot was derived from the superposition of the angular resolved Stokes parameters as $I_{Pol} = \sqrt{S_1^2 + S_2^2 + S_3^2}$. This emission distribution arises mainly from the lasing transverse mode, which revealed the highest degree of polarization P in the spectral investigation, depicted in figure 6.1c. The emission pattern exhibits the highest intensity in the center with an almost isotropic decrease towards higher emission angles. Thus, the obtained image coincides well with the simulated far field emission of the HE_{11} mode emitted from a circular ZnO NW with a diameter of 140 nm, shown in figure 6.3d. This unambiguously proves the occurrence of the fundamental mode lasing in this thin ZnO NW with a diameter below the multimode cutoff, as predicted by the effective mode index in figure 6.2a. Additionally, the horizontal linescans of the measured (blue) and the simulated emission (red) along the polar angle

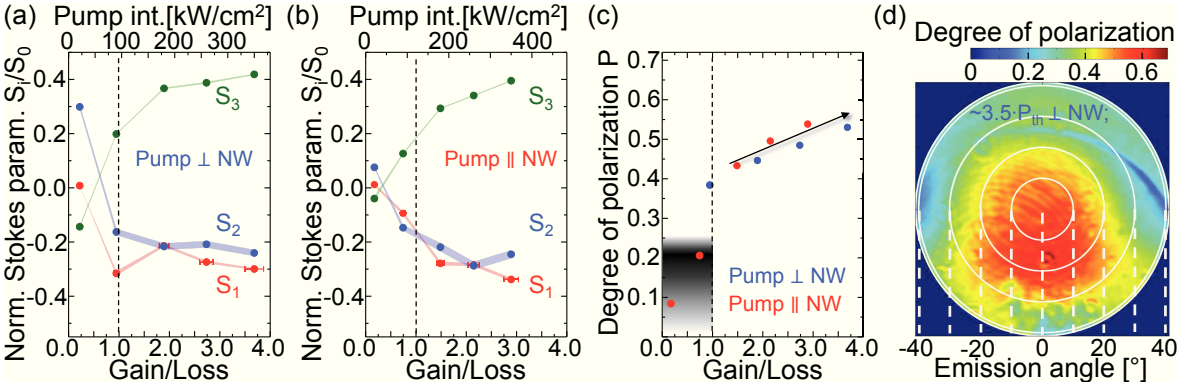

Figure 6.4: (a,b) Normalized Stokes parameters S_i/S_0 as a function of the pump intensity (gain/loss ratio) for perpendicular polarized (a) and for parallel polarized (b) pump light. The Stokes parameters change abruptly when the pump intensity overcomes the threshold. Subsequently they change only gradually. (c) The degree of polarization P versus the gain/loss ratio reveals also an abrupt increase at the laser threshold from a nearly unpolarized state (black shaded area) with $P \lesssim 0.2$ to the lasing regime with higher polarization. The P value increases gradually in the lasing regime, as the spontaneous emission is further suppressed relatively to the laser emission. (d) Angular resolved degree of polarization P at ~ 3.5 times the laser threshold.

of 0° almost perfectly match, as depicted in figure 6.3e. The Fourier image acquisition using the head-on setup averages over 10 s including $\sim$ 1000 excitation pulses with each being a single $\sim$ 10 ns experiment. However, the emission pattern is highly reproducible and independent of the polarization of the pump light (see supporting information of reference [40]).

Gaining further insights into the polarization properties of the thin ZnO NW required the evaluation of the lasing mode's Stokes parameters. The respective normalized Stokes parameters S_i/S_0 are shown in figures 6.4a and 6.4b as a function of the pump intensity for perpendicular polarized and parallel polarized pump light, respectively. The Stokes parameters were averaged over emission angles of $0-5°$, $0-10°$ and $0-15°$, respectively, as the emission is most intense in this angular region. The shaded areas in figures 6.4a,b show the deviation of the three averaged Stokes parameters. This deviation of the three averaged values $S_i^{0-5°}$, $S_i^{0-10°}$ and $S_i^{0-15°}$ is remarkably small indicating that the Stokes parameters of the fundamental transverse mode are nearly homogeneous. The Stokes parameters have similar values independent of the polarization of the pump light. Thus, the orientation of the pump beam polarization influences only the efficiency of the absorption, but does not alter the performance and polarization of the transverse lasing mode(s). The normalized Stokes parameters exhibit rather small values below the laser threshold, as the spontaneous emission is nearly unpolarized with a degree of polarization of $P \lesssim 0.2$, as shown in figure 6.4c. The Stokes parameters abruptly change around the laser threshold, when the sharp stimulated modes evolve in the emission spectra. In addition, the transverse lasing mode is not significantly influenced by the increasing pump intensity, as no further dramatic change in the Stokes parameters occurred. However, the absolute values $|\, S_i/S_0 \,|$ seem to increase gradually, as the highly polarized laser emission further

dominates, while the spontaneous emission gets more and more negligible (compare lasing spectra in figures 6.1b,c). This becomes also apparent as an increasing degree of polarization shown in figure 6.4c. The Stokes parameters obtained from the Fourier imaging coincide only approximately with the values obtained by the spectral measurements that are depicted in figures 6.1b,c, because the Fourier imaging is not wavelength sensitive and averages over the whole emission spectrum containing different polarization information depending on the wavelength. However, the averaged polarization is still predominantly vertically polarized in agreement with the spectral measurements.
Figure 6.4d shows the angular resolved degree of polarization calculated by: $P = I_{Pol}/S_0$. The obtained emission distribution appears asymmetric, shifted downwards to polar angles smaller than 0°, because the contribution of the spontaneous emission is more intense in the upper half of the image due to shadowing by the substrate in the lower half. A stronger contribution of the spontaneous emission becomes apparent as a decreased P value. However, the pattern almost coincides with the far field pattern of the fundamental HE_{11} mode. The degree of polarization exhibits values of $\sim 0.60 - 0.65$ in the center, where the HE_{11} mode is most intense. These rather low values for a laser system are caused by two effects: (i) The incoherent superposition of different longitudinal lasing modes might cause a reduced P value in the acquired Fourier images. (ii) The low P value might also be an indication of variations of the polarization state either during one excitation pulse or between different excitation pulses. This leads to an incoherent superposition of the respective Stokes parameters of differently polarized transverse HE_{11} modes and indeed reduces the degree of polarization. Such an incoherent superposition is exemplary calculated in the following, for two completely polarized modes with $S_i^{(1)}$ and $S_i^{(2)}$ and an intensity ratio of $a^{(1)}/a^{(2)}$, where $a^{(1)} + a^{(2)} = 1$. These modes exhibit different orientations of the linear polarization, which are tilted by 45°. The degree of polarization can be calculated by:

$$\begin{pmatrix} S_0 \\ S_1 \\ S_2 \\ S_3 \end{pmatrix}^{(1+2)} = a^{(1)} \begin{pmatrix} 1 \\ 1 \\ 0 \\ 0 \end{pmatrix}^{(1)} + a^{(2)} \begin{pmatrix} 1 \\ 0 \\ 1 \\ 0 \end{pmatrix}^{(2)}, \tag{6.1}$$

$$P^{(1+2)} = \sqrt{(a^{(1)} + a^{(2)})^2 - 2a^{(1)}a^{(2)}} \leq 1 = P^{(1)} = P^{(2)}, \tag{6.2}$$

revealing that the P value indeed decreases due to the incoherent superposition of different transverse and/or longitudinal modes.

6.2.3.2 Lasing of high order modes and mode competition

In order to prove that the lasing mode in thick ZnO NWs with diameters above $\sim 200\,\text{nm}$ switches to high order mode(s), as predicted by FDTD simulations (compare figure 6.2a),

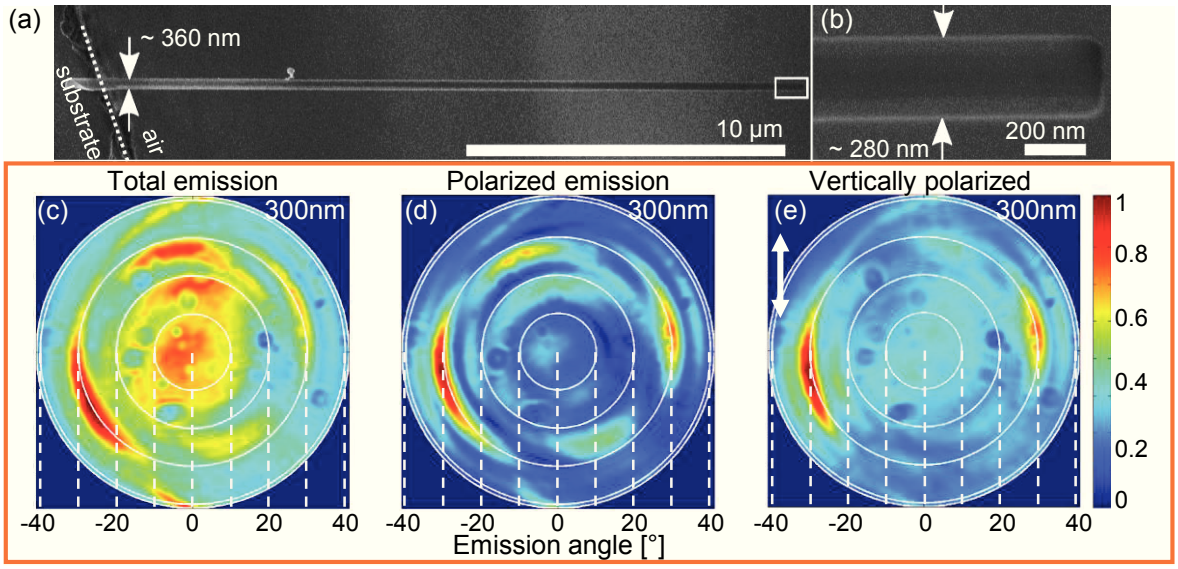

Figure 6.5: (a) The SEM image shows the thick ZnO NW laser with a diameter ranging from $\sim 280\,\text{nm}$ to $\sim 360\,\text{nm}$ and a length of $\sim 23.1\,\mu\text{m}$. (b) SEM image of the NW end revealing the smooth facet. (c) Angular resolved pattern of the total (superimposed polarized and unpolarized) emission from the ZnO NW laser shown in (a). (d) The polarized part I_{pol} of the angular resolved NW laser emission (shown in (c)) was calculated using the Stokes parameters. (e) Fourier image of the vertically polarized emission acquired using a linear polarizer.

the NW shown in figures 6.5a,b was investigated using the head-on Fourier imaging setup. This ZnO NW ($d \sim 280 - 360\,\text{nm}$) exhibits about twice the diameter of the thin ZnO NW investigated in the previous section. ZnO NWs of that thickness can theoretically support at least six modes, as suggested by figure 6.2a. The dependence of the optical output power on the pump intensity accompanied by the evolution of the emission spectra proved laser action (see supporting information of reference [40]). The angular resolved distribution of the total (polarized and unpolarized) NW emission in figure 6.5c is clearly different compared to the emission pattern of the thin NW. Here, the weak central emission decreases towards higher emission angles of $\sim 15 - 20°$ and is additionally surrounded by an intense emission rim at angles of $\sim 30°$. Such an intense emission rim was completely absent for the thin ZnO NW laser indicating laser emission of high order mode(s), as these modes offer rim-like emission distributions (compare figure 6.2b). However, among the first six transverse modes present in a 300 nm wide ZnO NW, only the fundamental HE_{11} emits along the NW axis leading to the most intense emission at the center of the Fourier image. Thus, the total emission pattern for the thick ZnO NW laser seems to be caused by an admixture of several transverse modes with contributions from the fundamental HE_{11} and at least one higher order mode exhibiting an annular distribution at $\sim 30°$. Figure 6.5d depicts the polarized part of the emission pattern I_{pol} measured for the thick ZnO NW laser. The respective Fourier image reveals a minimum in the center, whereas the highest intensity occurs at $\sim 30°$ indicating highly polarized emission of the high order

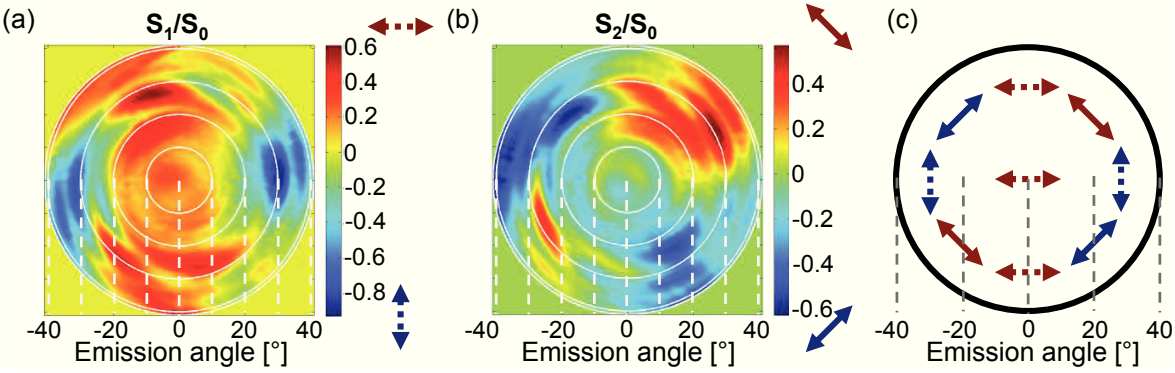

Figure 6.6: (a,b) The angular resolved normalized Stokes parameters S_1/S_0 (a) and S_2/S_0 (b) depict the respective orientation of the linear polarized part of the laser emission from the thick ZnO NW shown in figure 6.5a. (c) Schematic angular resolved emission pattern of the linear polarized emission, as obtained by combining the results of (a) and (b). The emission rim is azimuthally polarized for emission angles $\gtrsim 15 - 20°$. The azimuthally polarized emission coincides with the expectations for the TE_{01} mode, while the horizontally polarized emission in the center indicates the admixture of the fundamental HE_{11} mode.

mode(s). The angular resolved, vertically polarized emission depicted in figure 6.5e shows that the left and right part of the emission rim are predominantly vertically polarized, while the upper and the lower part appear predominantly horizontally polarized.
Furthermore, the respective orientation of the linear polarized laser emission was investigated by measuring the normalized Stokes parameters S_1/S_0 and S_2/S_0 as a function of the emission angle, as shown in figures 6.6a and 6.6b, respectively. In figure 6.6a emission regions of horizontal (red) and vertical (blue) polarization are distinguished, whereas figure 6.6b marks emission regions with a polarization orientation of $\pm 45°$. The schematic drawing in figure 6.6c depicts the orientation of the linear polarized laser emission as a function of the emission angle, as obtained by merging the insights gained from the Stokes parameters. The emission rim with emission angles $\gtrsim 15 - 20°$ is azimuthally polarized, which is unambiguously and only consistent with the polarization of the TE_{01} mode (compare figure 6.2b). The central part of the emission pattern exhibits a dominant horizontal polarization. Thus, the laser emission originating from the thick ZnO NW in figure 6.5a seems to be an admixture of a dominant TE_{01} mode with contributions of the fundamental HE_{11} mode. Static FDTD simulations in the literature usually predict lasing of the TE_{01} mode [115]. However, these simulations were not capable of predicting such an admixture of several transverse modes with contributions of the fundamental mode.

6.2.4 Dynamical simulations

It was possible to observe the switching from single mode to multimode operation in ZnO NW lasers as a function of the diameter. Subsequently, comparative theoretical studies were carried out using the dynamical simulation method, combining both semiconductor Bloch equations and FDTD [150], in order to corroborate these experimental findings.

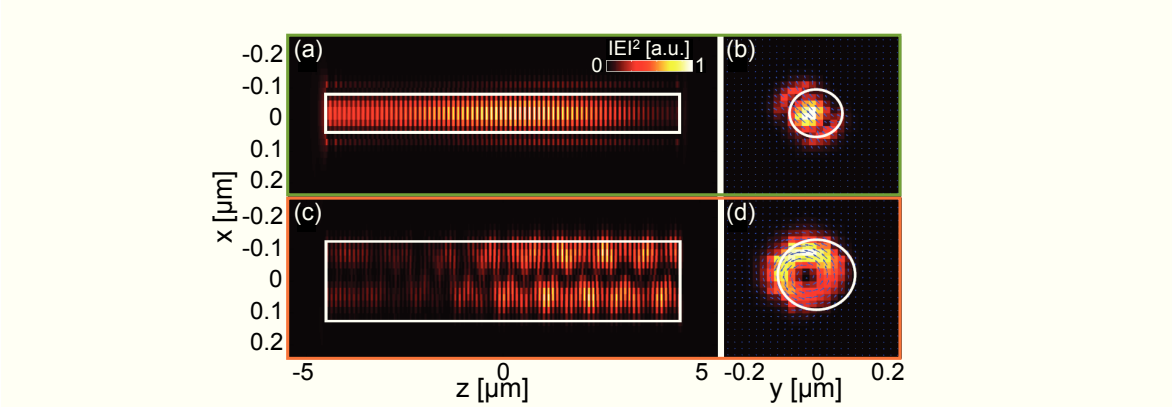

Figure 6.7: Intensity distributions as temporal snapshots of the normalized electric field $|\,E\,|^2$ within ZnO NW lasers of different diameter as simulated by FDTD combined with the semiconductor Bloch equation, as a suitable material model. The plots in the top row (a,b) depict the results of a single mode NW with a diameter of 140 nm (green), whereas the panels in the bottom row (c,d) refer to a multimode NW with 220 nm diameter (orange). Plots (a) and (c) show the longitudinal cross section, while (b) and (d) depict the transverse field profiles.

Most of the material parameters were taken from reference [183] in order to model ZnO appropriately in the different excitation regimes. An overview over all used parameters is given in reference [40]. The simulated NW morphology exhibits a circular cross section and a length of 9 µm. Thus, the simulated NW length was only half the length of the experimentally investigated NWs in order to manage the numerical expenses. However, the simulated NW length is reasonable, as individual ZnO NWs with lengths down to $\lesssim 5\,\mu m$ enable laser oscillations [22].

First, a thin ZnO NW laser with a diameter of 140 nm was considered. Fundamental mode lasing occurred in such a ZnO NW, as it was shown in chapter 6.2.3.1. Indeed, the dynamical simulation confirmed the occurrence of fundamental mode operation for such a thin ZnO NW laser. Figures 6.7a and 6.7b show a temporal snapshot of the HE_{11} mode in the longitudinal cross sectional view and the transverse mode profile, respectively. However, the polarization orientation of the HE_{11} mode varied, when the dynamical simulation was repeated several times, since the mode properties are sensitive to the initial conditions at the onset of lasing. This is in agreement with the varying Stokes parameters in figure 6.1d. Furthermore, a certain superposition of varying polarization orientations might contribute to the rather low degree of polarization, which was observed in the time integrated head-on Fourier measurement (compare figure 6.4d and equations 6.1-6.2).

Subsequently, a 220 nm wide ZnO NW was simulated in order to confirm the multimode lasing in NWs of larger diameter. Note, the simulated NW is much closer to the critical diameter of $\sim$ 200 nm than in the experiment. Figures 6.7c and 6.7d show an exemplary temporal snapshot of the normalized electromagnetic field strength inside the NW along the longitudinal cross section and the transverse mode profile, respectively. In the dynamical simulation, a spatially and temporally varying transverse field profile was observed during laser emission, which was indeed dominated by the azimuthally polarized,

doughnut-like shaped TE_{01} mode, as shown in figure 6.7d. The results of the dynamical simulation coincide with both the predictions of quasi-static calculations [115] and the experimental observations presented in chapter 6.2.3.2. In addition, the admixture of the HE_{11} mode became also apparent in the simulation results by an analysis of the transverse mode profile. The crescent-shaped intensity profile, as shown in figure 6.7d, is caused by the interference of these two transverse modes. The simulation results and the experimental observed multimode NW lasing are therefore in good agreement.

6.3 Transverse mode dependent laser dynamics

6.3.1 Laser dynamics and double-pump response

In macroscopic laser systems such as well studied vertical cavity surface emitting lasers (VCSEL), multimode laser operation significantly changes the laser dynamics [209, 210]. Significant changes of the laser dynamics can also be expected for multimode NW lasers due to mode competition, since the transverse modes exhibit a spatial overlap [209] (compare figure 6.2b). The ultrafast double-pump approach has been introduced in chapter 5. This technique enables an investigation of the ultrafast NW laser dynamics on the picosecond time scale. Thus, the temporal dynamics of several ZnO NW lasers were characterized using the measurement geometry sketched in figure 5.1d. The experimental conditions were similar to the measurements in chapter 5, such that the intensity of the strong pump 1 and the weak pump 2 were set to twice and 0.2 times the laser threshold, respectively.

Figure 6.8a compares the double-pump responses of three different ZnO NWs with diameters in the single mode regime ($\sim$ 151 nm; green), approximately at the multimode cutoff ($\sim$ 210 nm; black), and well in the multimode lasing regime ($\sim$ 281 nm; orange), respectively. For positive time delays $\tau > 0$ ps, when pump 2 samples the laser process that was induced by pump 1, the double-pump measurement is sensitive to the NW laser dynamics, as explained in chapter 5.4. The double-pump response displayed in the top row (green) in figure 6.8a reveals the expected, typical behaviour of a thin photonic ZnO NW laser that is already known from figure 5.9b. Furthermore, this curve can be reproduced using the simple laser rate equation model from chapter 3.5 including the cavity photon number for just one mode. However, clear differences become apparent for the other two NW laser devices in the middle (black) and bottom row (orange), respectively, showing more complicated double-pump responses, which cannot be fitted anymore using the rate equation model with just one cavity photon number. These two NW lasers exhibit two local maxima indicating an unambiguous change in the laser operation due to the multimode behaviour. The $\sim$ 210 nm thick NW at the multimode cutoff shows an initial maximum at $\sim$ 1.5 ps followed by a rapid decay and a subsequent recovery to a secondary maximum at $\sim$ 14 ps. For the thickest $\sim$ 281 nm wide NW, the initial maxi-

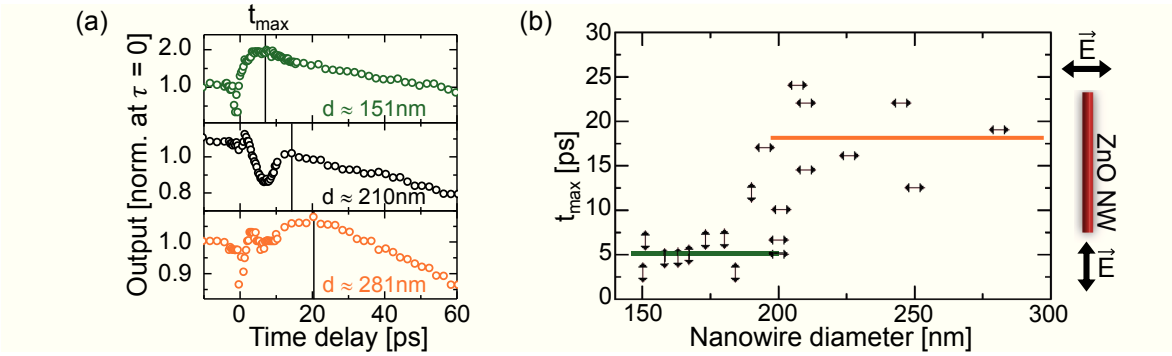

Figure 6.8: (a) Double-pump responses as a function of the time delay τ between the two excitation pulses measured for three exemplary ZnO NW lasers with diameters of $\sim$ 151 nm (green), 210 nm (black) and 281 nm (orange), respectively. The plots indicate the change in the laser dynamics. The vertical black lines show the time delay of the slowest and most prominent maximum in the double-pump output (t_{max}) for each ZnO NW. (b) The time value t_{max}, at which the material absorption recovers (figure 5.8d), versus the NW diameter. The dominant NW laser output polarization relatively to the NW axis is indicated by the orientation of the arrow symbols. The average values $\bar{t}_{max}$ are marked as horizontal line for NWs with diameters below (green; $\bar{t}_{max} \sim 5$ ps) and above (orange; $\bar{t}_{max} \sim 18$ ps) the critical value of $\sim$ 200 nm.

mum at $\sim$ 3 ps decays also in order to recover slowly into a second maximum at $\sim$ 20 ps. Thus, the thinnest NW with the smallest t_{max} value, shows the fastest overall response (t_{max} depicts the time delay, at which the second, slower maximum occurs). In thicker, multimode NWs the second pump 2 cannot be absorbed maximally (compare figure 5.8d) until larger time delays of $\tau \sim 15 - 20$ ps, because a (second) mode with a longer photon cavity lifetime seems to be competing for the optical gain that is available in the semiconductor NW. Hence, the two maxima and the slowed down dynamics are a clear signature of the multimode operation.

Figure 6.8b depicts the dependence of the t_{max} value on the ZnO NW diameter. For NW lasers with two maxima, the second and mostly more prominent maximum is plotted. In general, photonic ZnO NW lasers with diameters below $\sim$ 200 nm exhibit a faster value of $\bar{t}_{max} \sim 5 - 6$ ps (green horizontal line in figure 6.8b), while thicker NW lasers with multimode operation show a slower response with a value of $\bar{t}_{max} \sim 18$ ps (orange horizontal line). Additionally, this abrupt change in the NW laser dynamics involves a change in the output polarization of the NW, as indicated in figure 6.8b by the orientation of the data symbols. Only polarization components perpendicular or parallel to the NW axis can be distinguished in the double-pump measurement, which is a drawback compared to the head-on setup. The dominant perpendicular polarization component of the thick NWs corresponds to a large azimuthal electric field component of the TE_{01} mode within the NW, that was determined using the head-on Fourier measurement (see figure 6.6c). In contrast, the fundamental HE_{11} mode reveals strong electric field components in longitudinal direction parallel to the NW axis, which was observed for thin ZnO NW lasers. Thus, the change from parallel to perpendicular polarized laser emission at NW diameters of $\sim$ 200 nm indicates the switching from fundamental HE_{11} mode lasing to

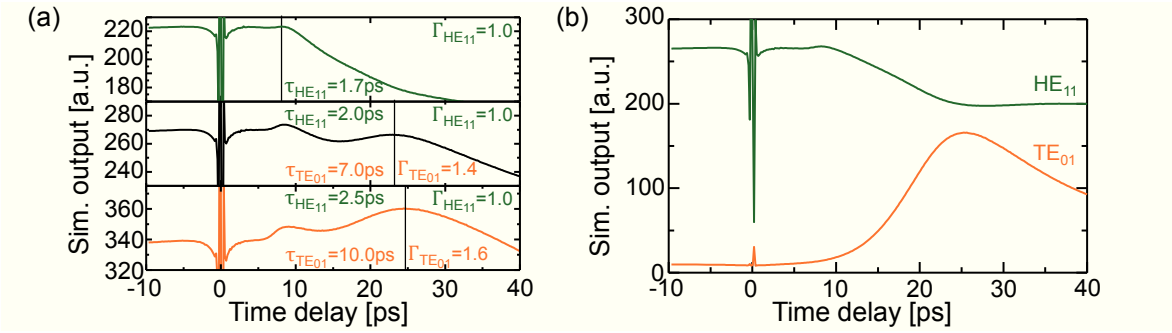

Figure 6.9: (a) The simulation results show the double-pump response as a function of the time delay. Simulations were performed applying a multimode laser rate equation model for a thin ($<$ 200 nm diameter; green), a medium sized ($\sim$ 200 nm diameter; black) and a thick ($>$ 200 nm diameter; orange) ZnO NW laser. (b) Simulated total output of a thick, multimode NW laser separated into the contributions of the two individual transverse modes.

multimode lasing with a dominating TE_{01} mode for larger diameters. Furthermore, the abrupt change in the laser dynamics confirms the results of the head-on measurement revealing a change of the operating laser mode.

As the slow, second maximum dominates the double-pump response especially of thick ZnO NW lasers with predominantly perpendicular polarized emission, this slow component is intuitively assigned to the TE_{01} mode, while the HE_{11} mode seems to cause the fast component. This assignment is consistent with the expected higher resonator feedback of the TE_{01} mode [115] leading to a slower dynamical response. This will be shown in the next chapter. Nevertheless, the determined critical NW diameter for mode switching of $\sim$ 200 nm nicely coincides with the results of the quasi-static calculations in figure 6.2a.

6.3.2 Simulation of the double-pump response

The double-pump responses shown in figure 6.8a can be modelled by laser rate equations, as described in chapters 3.5 and 5.4.2. However, modelling the double-pump response of multimode NWs required a modification of this laser rate equation model (see equations 3.3) by calculating the cavity photon numbers $s_{HE_{11}}$ and $s_{TE_{01}}$ for each mode separately. In general, the Purcell factor was set to F = 1, as the model described photonic NWs and the rate equation for dN_2/dt remained unchanged. However, the components in the laser rate equations including the cavity photon number were changed to:

$$\beta \cdot s \rightarrow \Gamma_{HE_{11}} \beta_{HE_{11}} s_{HE_{11}} + \Gamma_{TE_{01}} \beta_{TE_{01}} s_{TE_{01}}, \tag{6.3}$$

and two separated rate equations for the photon cavity numbers $ds_{HE_{11}}/dt$ and $ds_{TE_{01}}/dt$ were introduced. The ZnO exciton lifetime was set to $\tau_m = A_0^{-1} = 350$ ps, and the spontaneous emission factors exhibited values of $\beta_{HE_{11}} = 0.008$ and $\beta_{TE_{01}} = 0.003$, respectively. In addition, a thermalization time of $\tau_{therm} = 1$ ps was chosen in order to adapt the correct carrier thermalization of ZnO.

The confinement factors $\Gamma_{TE_{01}}$,$\Gamma_{HE_{11}}$ and the photon cavity lifetimes $\tau_{TE_{01}}$, $\tau_{HE_{11}}$ were varied in order to adapt the double-pump response for NWs of different thickness in a correct manner, because all these values depend on the NW diameter. Figure 6.9a shows the simulation results for the total output versus the time delay for three sets of parameters representing the dependence on the NW diameter. Note that the total output was obtained by integrating the photon cavity number for all modes over the whole simulated time scale similar to the simulation shown in figure 5.8d. The used values for the photon cavity lifetimes $\tau_{HE_{11}} = \gamma_{HE_{11}}^{-1}$ (green) and $\tau_{TE_{01}} = \gamma_{TE_{01}}^{-1}$ (orange) as well as for the confinement factors $\Gamma_{HE_{11}}$ (green) and $\Gamma_{TE_{01}}$ (orange) are displayed in figure 6.9a for the respective simulation.
The thin single mode NW with a diameter below 200 nm (green graph in figure 6.9a) was simulated using only the HE_{11} mode, while the medium sized NW with ~ 200 nm diameter and the thick NW above 200 nm diameter were calculated using both modes. The simulation results depicted in figure 6.9a coincide qualitatively with the experimental results shown in figure 6.8a, when the confinement factor of the fundamental mode was kept constant at $\Gamma_{HE_{11}} = 1$, while the confinement factor of the TE_{01} mode increases slightly with increasing diameter. This is in agreement with quasi-static FDTD simulations of semiconductor NW waveguides [39, 115], as the TE_{01} mode is less confined in the vicinity of the multimode cutoff. Furthermore, the photon lifetime of both modes increased, corresponding to an enhanced mode reflectivity, which is also in good agreement with quasi-static FDTD simulations. Note, it was necessary to assume that the HE_{11} mode is collected two times more efficiently than the TE_{01} mode. The HE_{11} mode with shorter photon lifetimes and thus smaller reflectivity is the dominating lasing mode for small time delays, while the TE_{01} mode with higher reflectivity becomes dominant for larger time delays, as depicted in figure 6.9b.
The experimental obtained double-pump responses are described quite nicely by using the modified laser rate equation model with two transverse modes. In addition, the faster response could be assigned to the fundamental mode, while the slower response is caused by the high order mode.

6.4 Mode filtering in tapered nanowires

It has been demonstrated in chapter 6.2 that experimental results of the far field measurement and the results of the dynamical simulation approach show good agreement. Furthermore, the discussion of these results indicated that certain trade-offs occur for an appropriate choice of the NW laser diameter. Thin NW lasers operate in the single mode regime and benefit therefore from the defined emission profile of the fundamental HE_{11} mode (figure 6.3c) and the fastest temporal dynamics in photonic NW lasers (green line in figure 6.8b), but they unfortunately suffer from low output intensities due to the small material volume of the laser device. Conversely, multimode NWs undesirably reveal

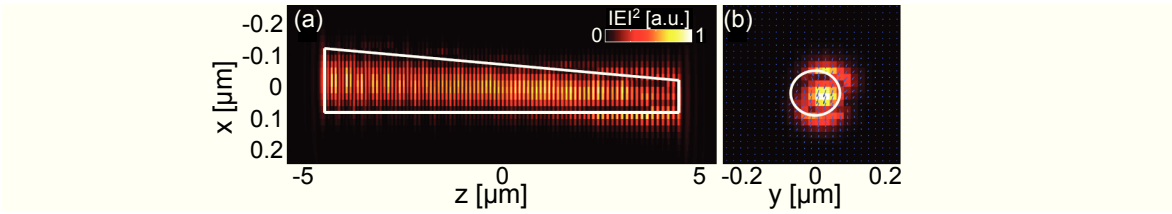

Figure 6.10: A temporal snapshot of the intensity distribution within an optimized NW laser was calculated by the dynamical simulation method [40, 150]. The tailored geometry exhibits a diameter starting in the single mode regime (d_{min} = 120 nm; right end facet) and ending in the multimode regime (d_{max} = 220 nm; left end facet). The colour plots in (a) and (b) show the longitudinal cross section and the transverse mode profile, respectively, indicating that the optimized NW laser exclusively supports a single mode.

a less directional emission (figure 6.5c) and a slower dynamic response (orange line in figure 6.8b). Nevertheless, the morphological properties of NWs can be tailored in order to optimize optical properties such as emission [211] and absorption [13]. Thus, the dynamical simulation method and the gained expertise was used in order to achieve a hybrid situation providing optimized performance including output power, efficiency, and emission directionality, as these properties are essential for capturing and coupling of the NW laser photons to adjacent nanophotonic components.

The NW morphology was simulated and optimized towards a waveguide taper, as shown in figure 6.10, with a diameter starting in the single mode regime with a minimal value of 120 nm and ending in the multimode regime with a diameter of 220 nm, respectively. Hence, the NW taper should provide efficient mode filtering for the undesired higher order modes. Figure 6.10a shows that this numerically optimized NW laser indeed supports only one single laser mode leading to a transverse mode profile (figure 6.10b) that is dominated by the fundamental HE_{11} mode. On average, the dynamical simulations show that the emission power of the tapered NW laser is $\sim 90\,\%$ of the output power emitted by a thick, 220 nm wide NW, while the power radiated by the homogeneously thin NW decreases to only $\sim 70\,\%$. Thus, these results prove that the thorough adjustment of the NW morphology leads to NW lasers with higher emission intensity due to the larger material volume similar to a thick NW accompanied by a more defined emission profile of a thin, single mode NW. Note that such tapered ZnO NWs can be synthesized [212] and the single mode NW laser in figure 6.3a already exhibited such a taper morphology.

6.5 Summary

Recently developed measurement methods were applied in order to investigate how the fundamental emission properties of individual NW lasers depend on the transverse mode structure. These emission properties include the angular resolved emission distribution and the polarization orientation of the NW laser light. Both were detected in the head-on measurement geometry. Furthermore, the output laser dynamics were studied using the

double-pump approach, which was introduced in chapter 5. The spectral polarization properties were determined by means of the Stokes parameters in initial head-on measurements revealing that the longitudinal lasing modes are highly polarized with a degree of polarization of $P \gtrsim 0.8$. Conversely, the spontaneous emission is nearly unpolarized. Thus, detecting the highly polarized part of the emission ($P \gtrsim 0.3\,\%$) is sufficient in order to image the dominant (longitudinal and transverse) lasing modes.
Furthermore, the polarization orientation of the pump light was used to adjust the supply with photoexcited charge carriers, as the light absorption within the NW laser depends on the orientation of the electric field relatively to the NW axis [37]. However, changing the carrier supply by the orientation of the excitation polarization did not significantly alter the dominant polarization properties of the lasing mode, which is predominantly determined by the NW diameter.
Fourier imaging of the angular emission distribution has clearly proven single transverse mode lasing of the fundamental HE_{11} mode at room temperature in a thin ZnO NW laser exhibiting a diameter below the cutoff of the higher order TE_{01} mode. Power dependent measurements of the Stokes parameters using the Fourier imaging revealed that the P value at small emission angles (in the image center) abruptly increases at the laser threshold. This abrupt change is indicative of the onset of lasing. The respective short laser pulses of the thin NW were in the range of $\sim 5\,\mathrm{ps}$ enabling fast modulation capabilities of such ZnO NW lasers.
A significant change in the laser dynamics occurred at the transition diameter from single to multimode waveguiding of $d \approx 200\,\mathrm{nm}$, as the measured output dynamics get slower and more complicated showing the signature of two transverse modes. The abrupt change in the temporal dynamics was accompanied by the change of the output polarization indicating a switching in the transverse lasing modes. Lasing in thick multimode NW lasers above of $d \approx 200\,\mathrm{nm}$ is thus dominated by the higher order TE_{01} mode, but with strong contributions of the fundamental HE_{11} mode. This was verified by the Fourier imaged angular emission distribution of a thick ZnO NW laser.
In general, the experimental results show very good agreement with the results of the dynamical simulation method [150], which was subsequently used in order to optimize the NW morphology towards efficient mode filtering. Thus, the selection of the desired fundamental mode in a tapered NW is an efficient method to create a bright and efficient NW laser device benefiting from large material volume without suffering from multimode operation.

7 Conclusion and outlook

Semiconductor nanowires (NWs) show excellent optical properties such as light emission from subwavelength dimensions and strong optical confinement in subwavelength geometry. In addition, the large optical gain from the semiconductor material enables light amplification and the NW morphology provides an efficient resonator structure. These unique properties allow semiconductor NWs to be exploited as nanoscaled coherent light sources. Nowadays, such NW lasers consequently occupy the spectrum from the UV to the NIR [116]. However, three fundamental key challenges are considered within this thesis for the successful integration of individual NW lasers as coherent light sources into technological relevant optoelectronic nanoscaled applications: (i) Continuous wave (cw) emission has to be established and its limitations have to be investigated in order to draw the route towards a stable coherent light source with subwavelength dimensions. (ii) The fundamental temporal dynamics of semiconductor NW lasers and the underlying physical properties have to be understood in order to precisely turn such lasers on and off. This allows to investigate approaches towards the modification and control of the temporal dynamics in order to realize ultrafast optical modulators based on NW lasers. (iii) A precise control over the emission properties, by controlling the transverse modes and the temporal dynamics of individual NW lasers is required for an efficient coupling of the laser emission into adjacent nanophotonic components. Several advanced experimental techniques were developed and used in the scope of this work to gain insights into these three challenges. The understanding of the obtained results has lead to efficient modification approaches, optimizing the respective NW laser device, and thus bringing them closer to be exploitable in real world applications.

The investigation of CdS:Sn NWs and their optical properties in chapter 4 focuses on the first key challenge of establishing cw laser emission in individual NWs. The intense optical pumping, required for lasing, usually introduces a high amount of thermal energy into the semiconductor material. This thermal budget needs to be kept as low as possible in order to avoid material degradation under high cw excitation intensities. This was achieved by synthesizing CdS NWs of high optical gain and good resonator quality. These NWs were fabricated via the VLS mechanism using an alternative growth route with Sn as a catalyst leading to an incorporation of Sn into the CdS material. These CdS:Sn NWs grow along the c-axis and exhibit a perfect single crystalline wurtzite structure, as no extended defects were observed in high-resolution TEM. Approximately $\sim 1-4\,\mathrm{at.\%}$ of Sn were incorporated into the CdS lattice during NW synthesis, but the structural properties of CdS:Sn NWs remained nearly unchanged in comparison to undoped CdS. Initially, the optical properties of the NW ensembles were investigated using low temperature CL and PL measurements. Both reveal in good agreement that the incorporated Sn causes optically active transitions in the CdS material, as these transitions are absent

for undoped CdS NWs. These transitions were assigned to donor-acceptor pair (DAP) and free to bound transitions of a free electron with an acceptor bound hole (e,A) by temperature dependent and time resolved PL measurements that were also carried out on the NW ensemble. Thus, the energetic positions of the Sn induced donor and acceptor levels were determined and depicted in a schematic band diagram of the CdS:Sn material. In particular, the monochromatic CL images obtained at low temperatures show that straight, long CdS:Sn NWs with diameters below $\lesssim 400\,\mathrm{nm}$ exhibit strong excitonic near band edge emission in comparison to the shallow (DAP and (e,A) transitions) and deep defect (DLE) related emission. As these type of CdS:Sn NWs were suitable to achieve lasing due to the good resonator structure, the optical properties of single NWs were subsequently investigated by means of µPL at low temperatures. Indeed, single NWs reveal at moderate optical cw excitation a dominant excitonic emission and negligible emission related to DAP, (e,A) and DLE transitions indicating their excellent optical quality. The µPL measurements, using high intensity cw excitation, reveal a broadening of the spontaneous emission superimposed by evolving sharp modes, which dominate the emission spectra at even higher pump intensities. Additionally, the power dependence of the optically pumped NW changes from a linear slope in the excitonic (spontaneous) emission regime to a superlinear increase when the sharp modes occur in the spectra indicating amplified spontaneous emission. The return to a linear dependence at the highest pump intensities proves cw laser oscillations in individual CdS:Sn (and undoped CdS) NWs at low temperature of 4 K. Furthermore, cw lasing was verified by fitting the experimental data by a multimode laser model [105]. The temperature stability of the cw NW lasing was subsequently checked at the pump intensity of $\sim 9\,\mathrm{kW/cm^2}$. The lasing spectra red-shifted with increasing temperature following the temperature induced band gap reduction. This is accompanied by a decreasing ratio of stimulated to spontaneous emission due to the decreasing optical gain. The cw lasing of this particular NW kept stable up to $\sim 120\,\mathrm{K}$ at these pump conditions. The cw lasing in single CdS:Sn and undoped CdS NW lasers is most likely induced by the formation of an electron-hole plasma, as the carrier density overcomes the Mott density at high cw excitation similar to the laser threshold in the experiment.

Based on this new insights, future work should focus on the consequent increase of the threshold temperature of cw NW lasing from $\sim 120\,\mathrm{K}$ towards room temperature and should investigate further gain materials than the already investigated CdS and GaAs/AlGaAs NWs [171] in order to extend the spectral range of such devices. The increase of the cw threshold temperature might require a modification of the NW resonator towards an enhanced reflectivity lowering the laser threshold. This approach might be accomplished by Bragg reflectors at the NW end facets. Alternatively, the temperature stability of the gain medium must be increased either by using a different semiconductor material or by using different gain concepts such as quantum mechanically confined structures. Besides this challenge, the research should envisage approaches for an electrically

or optically driven switching mechanism for the cw NW laser emission. The NW laser might be constantly supplied with a carrier density close to the population inversion/laser threshold and an (temporally variable) electrically or optically applied trigger can eventually induce laser emission.

Chapter 5 investigates the ultrafast temporal dynamics of semiconductor NW based laser devices including laser onset time, absorption recovery and output pulse width using the recently developed double-pump measurement technique [38, 118]. The material dynamics driven onset time τ_{on} was investigated for three different NW model systems made of CdS, ZnO and GaN, which were already demonstrated to exhibit lasing [22, 23, 133]. The onset time of NW lasers is largely determined by microscopic processes in the semiconductor material following the photoexcitation, as it is independent of the NW diameter, the transverse mode(s) and optical system (photonic or plasmonic). Measuring the onset time of the three different materials at a fixed pump wavelength of 355 nm results in the fastest τ_{on} for ZnO NW lasers of $\sim$ 1.0 ps, followed by CdS NWs revealing a value of $\sim$ 2.4 ps and GaN NWs exhibiting the slowest value of $\sim$ 3.5 ps, although the energetic difference between pump and emission energy is smallest for GaN. The laser onset seems to be largely determined by the carrier relaxation/thermalization in the semiconductor materials, which is described by the energy loss rate (ELR) of the carriers. Among the investigated materials, ZnO exhibits the highest ELR due to the strongest carrier-phonon coupling, whereas the effective electron-phonon interaction in GaN is very weak due to the hot phonon effect. Other semiconductor NW lasers, investigated throughout the literature, very likely switch on slower than ZnO NW based lasers (for a similar energetic difference between pump and emission energy), because they exhibit weaker carrier-phonon interaction than ZnO. Furthermore, the onset time depends on the excess energy of the carriers $\Delta E_{e(h)}$ defined as the energy of the photoexcited carriers relatively to the respective band extremum. The excess energy was tuned using CdS NW lasers as model system by varying the pump energy between 3.49 eV and 2.95 eV. This reduction of the pump energy led to an acceleration of the laser onset from $\sim$ 2.4 ps to $\sim$ 1.9 ps. The process was fully reversible, making this an intuitive and efficient way to adjust the laser onset time. However, the temporal tuning range is limited by the ELR of the respective material.

While the laser onset time τ_{on} depends on the microscopic relaxation processes in the gain material, the stimulated and spontaneous emission processes are determined by the optical geometry of the NW cavity and its surrounding. These emission processes, and especially the laser output pulse width, were modified by coupling the light, generated in the NW lasers, to surface plasmon polaritons of a silver surface, which was separated from the NW by a 10 nm thick LiF layer. These plasmonic laser devices were characterized by means of their spectral response revealing a band filling effect. Compared to photonic devices, the plasmonic laser characteristics indicated a suppressed superlinear light versus

pump response near the laser transition. Plasmonic ZnO NW lasing benefits from the extraordinarily high mode confinement of light, as these devices operate near the surface plasmon resonance leading to an Purcell enhanced stimulated emission rate. This was proven using the double-pump technique. The pulse width decreased significantly from $\sim 4-5\,\mathrm{ps}$ for photonic ZnO NW lasers down to ultrafast $\sim 600-800\,\mathrm{fs}$ for plasmonic ZnO NWs. In addition, the device diameters can be decreased to dimensions below the physical limitations of photonic lasing of $\mathrm{d} \gtrsim 140\,\mathrm{nm}$ using the plasmonic NW lasing approach. However, it was observed that temporal and size limitations occur approximately at diameters of $\sim 120\,\mathrm{nm}$, since the Purcell enhanced spontaneous carrier recombination becomes too fast, suppressing the build-up of a population inversion under short pulse excitation ($\sim 150\,\mathrm{fs}$). Currently, plasmonic ZnO NWs exhibit the fastest on-off switching speeds.
The temporal NW laser dynamics should be further, investigated using a suitable model system such as e.g. ZnO or CdS NW based lasers. These measurements should be performed as a function of pump energy and pump power in order to determine the functional dependence of the onset time (relaxation processes) on the excess energy and the carrier density. Furthermore, it should be checked whether the double-pump technique can be exploited to quantitatively characterize the effective mode and refractive indices of NW laser devices. This might be achieved by improving the simulation models used in chapter 5. The microscopic relaxation/thermalization processes in the gain material are significantly influenced by the lattice and carrier temperature. This should be investigated. While it is straightforward to vary the lattice temperature, it is more challenging to adjust the carrier temperature, as both influence each other by carrier-phonon interactions. Finally, approaches should be developed which further accelerate the onset dynamics. One approach might be performed with a constant carrier supply (electrically or optically), such that the NW laser is close to inversion and the pump pulse inducing gain just adds carriers to invert the active medium. Another approach should check whether the onset time can be accelerated by using quantum confined gain materials, as 2D structures exhibit faster energy relaxation times than their 3D counterparts [186]. In addition, the optical device configuration should be varied for example by enhancing the cavity quality factor $\mathrm{Q_{cav}}$. The enhanced Q-factor combined with the plasmonic NW laser geometry might help to overcome the lower size limit for plasmonic ZnO NW lasing.

In chapter 6, the third challenge is addressed by a combinatory study using head-on, double-pump measurements, and the dynamical simulation method. Single transverse mode lasing of the fundamental $\mathrm{HE_{11}}$ mode was proven for a thin ZnO NW laser with a diameter below the single mode cutoff by Fourier imaging of the angular emission distribution. The emission pattern for this particular NW with a diameter of $\sim 140-150\,\mathrm{nm}$ at its thinnest part revealed the most intense emission along the NW axis, which coincides nicely with the results of static FDTD simulations. The laser pulses of this single trans-

verse mode NW lasers were in the range of $\sim 5\,\mathrm{ps}$, as determined by the double-pump technique. The NW laser dynamics changed abruptly at a NW diameter of $\sim 200\,\mathrm{nm}$, because the transition from single to multimode waveguiding occurs at this diameter. The output dynamics became significantly slower than 5 ps and more complicated, indicating the signature of multimode lasing of two transverse modes. The polarization orientation was measured for several NW lasers showing that fast single mode NWs exhibited a dominant electric field along the NW axis, which is indicative of the HE_{11} mode, while slow multimode NWs were predominantly polarized perpendicular to the NW axis. The perpendicular polarization of the laser emission is a signature of a dominant TE_{01} mode. Multimode lasing of a dominant TE_{01} mode with a strong admixture of the fundamental HE_{11} mode was proven by Fourier imaging of the angular emission distribution of a thick ZnO NW well in the multimode regime. These results of the head-on measurement are in well agreement with results of dynamical simulations using the FDTD and semiconductor Bloch equations approach. Finally, this dynamical simulation method was used to predict efficient photonic mode filtering in a tapered nanowire laser. The tapered ZnO NW with a diameter starting in the single mode regime (120 nm) and ending in the multimode regime (220 nm) selects the desired fundamental mode for lasing with improved output power, efficiency and directionality.
The mode switching behaviour should be verified using different NW materials in order to optimize also the theoretical simulation techniques. Furthermore, fundamental insights into the time-resolved mode structure during the NW laser pulse could be gained by integrating the head-on measurement setup into the double-pump setup. Thus, the angular emission distribution could be imaged for certain time delays τ between the two pump pulses. Mode competition and interaction of both modes could be imaged by this integrated head-on and double-pump technique, which is also capable of measuring other nanophotonic devices.

The three chapters about the continuous wave NW lasing (chapter 4), the temporal dynamics of the NW lasing process (chapter 5) and the transverse mode structure in NW lasers (chapter 6) have successfully addressed the three key challenges, as identified in chapter 1. Furthermore, they provide an important fundamental understanding of nanowire based coherent light sources, as they draw a consistent description of their physics. This is urgently required for future integration of NW lasers into nanoscaled optoelectronic applications. Additionally, new measurement and simulation techniques were developed, which could be further applied in order to investigate the fundamentals of individual nanophotonic devices, targeting the next steps in nanophotonic research such as the realization/integration of electrically driven nanoscaled coherent light sources and dynamically tunable lasers.

Bibliography

[1] Moore G 1965 *Electronics* **38** 114

[2] Rhines W C (April 2016) Moore's law and the future of solid-state electronics *Guest Blog of Scientific American, a Division of Nature America, Inc. - (http://blogs.scientificamerican.com/guest-blog/moore-s-law-and-the-future-of-solid-state-electronics/)*

[3] International Technology Roadmap for Semiconductors - ITRS 2.0 (May 2016) *http://www.itrs2.net/*

[4] Maiman T 1960 *Nature* **187** 493

[5] Radloff W 2010 *Laser in Wissenschaft und Technik* (Spektrum Akademischer Verlag)

[6] Eaton S W, Fu A, Wong A B, Ning C Z and Yang P 2016 *Nat. Rev. Mater.* 16028

[7] Choquette K D and Hou H Q 1997 *Proc. IEEE* **85** 1730–1739

[8] Mahler L, Tredicucci A, Beltram F, Walther C, Faist J, Witzigmann B, Beere H E and Ritchie D A 2009 *Nat. Photon.* **3** 46–49

[9] Altug H, Englund D and Vuckovic J 2006 *Nat. Phys.* **2** 484–488

[10] Fan Z, Wang D, Chang P C, Tseng W Y and Lu J G 2004 *Appl. Phys. Lett.* **85** 5923

[11] Fan Z and Lu J G 2005 *Appl. Phys. Lett.* **86** 123510

[12] Wallentin J, Anttu N, Asoli D, Huffman M, Aberg I, Magnusson M H, Siefer G, Fuss-Kailuweit P, Dimroth F, Witzigmann B and et al 2013 *Science* **339** 1057–1060

[13] Krogstrup P, Jörgensen H I, Heiss M, Demichel O, Holm J V, Aagesen M, Nygard J and Fontcuberta i Morral A 2013 *Nat. Photon.* **7** 306–310

[14] Tchernycheva M, Messanvi A, de Luna Bugallo A, Jacopin G, Lavenus P, Rigutti L, Zhang H, Halioua Y, Julien F H, Eymery J and et al 2014 *Nano Lett.* **14** 3515–3520

[15] Yan R, Gargas D and Yang P 2009 *Nat. Photon.* **3** 569–576

[16] Voss T, Kudyk I, Wischmeier L and Gutowski J 2009 *Phys. Status Solidi B* **246** 311–314

[17] Piccione B, Cho C H, van Vugt L K and Agarwal R 2012 *Nat. Nano.* **7** 640–645

[18] Yu H, Fang W, Wu X, Lin X, Tong L, Liu W, Wang A and Shen Y R 2014 *Nano Lett.* **14** 3487–3490

[19] Xu J, Zhuang X, Guo P, Zhang Q, Huang W, Wan Q, Hu W, Wang X, Zhu X, Fan C, Yang Z, Tong L, Duan X and Pan A 2012 *Nano Lett.* **12** 5003–5007

[20] Voss T, Svacha G, Mazur E, Müller S, Ronning C, Konjhodzic D and Marlow F 2007 *Nano Lett.* **7** 3675–3680

[21] Johnson J C, Choi H J, Knutsen K P, Schaller R D, Yang P and Saykally R J 2002 *Nat. Mater.* **1** 106–110

[22] Zimmler M, Bao J, Capasso F, Müller S and Ronning C 2008 *Appl. Phys. Lett.* **93** 051101

[23] Geburt S, Thielmann A, Röder R, Borschel C, McDonnell A, Kozlik M, Kühnel J, Sunter K A, Capasso F and Ronning C 2012 *Nanotechnology* **23** 365204

[24] Saxena D, Mokkapati S, Parkinson P, Jiang N, Gao Q, Tan H H and Jagadish C 2013 *Nat. Photon.* **7** 963–968

[25] Qian F, Li Y, Gradecak S, Park H G, Dong Y, Ding Y, Wang Z L and Lieber C M 2008 *Nat. Mater.* **7** 701–706

[26] Yang Z, Wang D, Meng C, Wu Z, Wang Y, Ma Y, Dai L, Liu X, Hasan T, Liu X and et al 2014 *Nano Lett.* **14** 3153–3159

[27] Gao H, Fu A, Andrews S C and Yang P 2013 *Proc. Natl. Acad. Sci. USA* **110** 865–869

[28] Xiao Y, Meng C, Wang P, Ye Y, Yu H, Wang S, Gu F, Dai L and Tong L 2011 *Nano Lett.* **11** 1122–1126

[29] Fu A, Gao H, Petrov P and Yang P 2015 *Nano Lett.* **15** 6909–6913

[30] Oulton R, Sorger V, Zentgraf T, Ma R, Gladden C, Dai L, Bartal G and Zhang X 2009 *Nature* **461** 629–632

[31] Liu X, Zhang Q, Yip J N, Xiong Q and Sum T C 2013 *Nano Lett.* **13** 5336–5343

[32] Zhang Q, Shan X, Feng X, Wang C, Wang Q, Jia J and Xue Q 2011 *Nano Lett.* **11** 4270–4274

[33] Hurtado A, Xu H, Wright J B, Liu S, Li Q, Wang G T, Luk T S, Figiel J J, Cross K, Balakrishnan G, Lester L F and Brener I 2013 *Appl. Phys. Lett.* **103** 251107

[34] Zhang M, Wille M, Röder R, Heedt S, Huang L, Zhu Z, Geburt S, Grützmacher D, Schäpers T, Ronning C and Lu J G 2014 *Nano Lett.* **14** 518–523

[35] Röder R, Wille M, Geburt S, Rensberg J, Zhang M, Lu J G, Capasso F, Buschlinger R, Peschel U and Ronning C 2013 *Nano Lett.* **13** 3602–3606

[36] Wille M 2013 *Optische und elektrische Eigenschaften von Zinn-dotierten CdS Nanodrähten* Master's thesis Friedrich Schiller University Jena

[37] Röder R, Sidiropoulos T P H, Tessarek C, Christiansen S, Oulton R F and Ronning C 2015 *Nano Lett.* **15** 4637–4643

[38] Sidiropoulos T P H, Röder R, Geburt S, Hess O, Maier S A, Ronning C and Oulton R F 2014 *Nat. Phys.* **10** 870–876

[39] Röder R, Ploss D, Kriesch A, Buschlinger R, Geburt S, Peschel U and Ronning C 2014 *J. Phys. D: Appl. Phys.* **47** 394012

[40] Röder R, Sidiropoulos T P H, Buschlinger R, Riediger M, Peschel U, Oulton R F and Ronning C 2016 *Nano Lett.* **16** 2878–2884

[41] Riediger M 2015 *Emissionscharakteristik von ZnO-Nanodrahtlasern* Master's thesis Friedrich Schiller University Jena

[42] Thomas D G and Hopfield J J 1962 *Phys. Rev.* **128** 2135–2148

[43] Hotje U, Rose C and Binnewies M 2003 *Solid State Sci.* **5** 1259–1262

[44] Imada A, Ozaki S and Adachi S 2002 *J. Appl. Phys.* **92** 1793

[45] Bieniewski T M and Czyzak S J 1963 *J. Opt. Soc. Am.* **53** 496–497

[46] Özgür Ü, Alivov Y I, Liu C, Teke A, Reshchikov M A, Dogan S, Avrutin V, Cho S J and Morkoc H 2005 *J. Appl. Phys.* **98** 041301

[47] Wang Z L 2004 *J. Phys.: Condens. Matter* **16** R829

[48] Meyer B K, Alves H, Hofmann D M, Kriegseis W, Forster D, Bertram F, Christen J, Hoffmann A, Straßburg M, Dworzak M, Haboeck U and Rodina A V 2004 *Phys. Status Solidi B* **241** 231–260

[49] Yoshikawa H and Adachi S 1997 *Jpn. J. Appl. Phys.* **36** 6237

[50] Klingshirn C 2007 *ChemPhysChem* **8** 782–803

[51] Klingshirn C, Fallert J, Zhou H, Sartor J, Thiele C, Maier-Flaig F, Schneider D and Kalt H 2010 *Phys. Status Solidi B* **247** 1424–1447

[52] Lei T, Fanciulli M, Molnar R J, Moustakas T D, Graham R J and Scanlon J 1991 *Appl. Phys. Lett.* **59** 944–946

[53] Monemar B 1974 *Phys. Rev. B* **10** 676–681

[54] Maruska H P and Tietjen J J 1969 *Appl. Phys. Lett.* **15** 327–329

[55] Barker A S and Ilegems M 1973 *Phys. Rev. B* **7** 743–750

[56] Strite S and Morkoc H 1992 *J. Vac. Sci. Technol., B* **10** 1237–1266

[57] Reshchikov M A and Morkoc H 2005 *J. Appl. Phys.* **97** 061301

[58] Klingshirn C 2005 *Semiconductor optics* vol 1439 (Springer Verlag)

[59] Yu P Y and Cardona M 2005 *Fundamentals of semiconductors* (Springer)

[60] Titova L, Hoang T, Jackson H, Smith L, Yarrison-Rice J, Lensch J and Lauhon L 2006 *Appl. Phys. Lett.* **89** 053119

[61] Dietz R E, Hopfield J J and Thomas D G 1961 *J. Appl. Phys.* **32** 2282–2286

[62] Reynolds D C, Look D C, Kim W, Aktas Ö, Botchkarev A, Salvador A, Morkoc H and Talwar D N 1996 *J. Appl. Phys.* **80** 594–596

[63] Koida T, Chichibu S F, Uedono A, Tsukazaki A, Kawasaki M, Sota T, Segawa Y and Koinuma H 2003 *Appl. Phys. Lett.* **82** 532–534

[64] Reynolds D, Look D C, Jogai B, Hoelscher J, Sherriff R, Harris M and Callahan M 2000 *J. Appl. Phys.* **88** 2152

[65] Heitz R, Hoffmann A and Broser I 1994 *Phys. Rev. B* **49** 14307–14314

[66] Chichibu S F, Uedono A, Onuma T, Sota T, Haskell B A, DenBaars S P, Speck J S and Nakamura S 2005 *Appl. Phys. Lett.* **86** 021914

[67] Im J S, Moritz A, Steuber F, Härle V, Scholz F and Hangleiter A 1997 *Appl. Phys. Lett.* **70** 631–633

[68] Haynes J R 1960 *Phys. Rev. Lett.* **4**(7) 361–363

[69] Hönerlage B and Schröder U 1977 *Phys. Rev. B* **16** 3608–3612

[70] Colbow K 1966 *Phys. Rev.* **141** 742–749

[71] Thomas D G and Hopfield J J 1962 *J. Appl. Phys.* **33** 3243

[72] Xu X, Zhao Y, Sie E, Lu Y, Liu B, Ekahana S, Ju X, Jiang Q, Wang J, Sun H *et al.* 2011 *ACS Nano* **5** 3660–3669

[73] Gross R and Marx A 2014 *Festkörperphysik* (Walter de Gruyter GmbH)

[74] A la Guillaume C B, Debever J M and Salvan F 1969 *Phys. Rev.* **177** 567–580

[75] Leite R C C, Scott J F and Damen T C 1969 *Phys. Rev. Lett.* **22** 780–782

[76] Damen T C, Porto S P S and Tell B 1966 *Phys. Rev.* **142** 570–574

[77] Dove M T 2003 *Structure and dynamics: an atomic view of materials* vol 1 (Oxford University Press)

[78] Aguilar-Hernández J, Contreras-Puente G, Morales-Acevedo A, Vigil-Galán O, Cruz-Gandarilla F, Vidal-Larramendi J, Escamilla-Esquivel A, Hernández-Contreras H, Hesiquio-Garduno M, Arias-Carbajal A *et al.* 2002 *Semicond. Sc. Technol.* **18** 111–114

[79] Ponce F A, Bour D P, Götz W and Wright P J 1996 *Appl. Phys. Lett.* **68** 57

[80] Liu R, Bell A, Ponce F A, Chen C Q, Yang J W and Khan M A 2005 *Appl. Phys. Lett.* **86** 021908

[81] Janotti A and de Walle C G V 2009 *Rep. Prog. Phys.* **72** 126501

[82] Hou D, Voss T, Ronning C, Menzel A and Zacharias M 2014 *J. Appl. Phys.* **115** 233516

[83] Limpijumnong S and Van de Walle C 2004 *Phys. Rev. B* **69** 035207

[84] Garces N Y, Wang L, Bai L, Giles N C, Halliburton L E and Cantwell G 2002 *Appl. Phys. Lett.* **81** 622

[85] Huang X H, Zhang C, Tay C B, Venkatesan T and Chua S J 2013 *Appl. Phys. Lett.* **102** 111106

[86] Byrne D, Herklotz F, Henry M O and McGlynn E 2012 *J. Phys.: Condens. Matter* **24** 215802

[87] Fröhlich H 1950 *Phys. Rev.* **79** 845–856

[88] Huang K and Rhys A 1950 *Proc. R. Soc. A.* **204** 406–423

[89] Reynolds D C, Litton C W and Collins T C 1971 *Phys. Rev. B* **4** 1868–872

[90] Stoneham A M 1981 *Rep. Prog. Phys.* **44** 1251

[91] Pankove J I 2012 *Optical processes in semiconductors* (Courier Corporation)

[92] Klingshirn C and Haug H 1981 *Phys. Rep.* **70** 315–398

[93] Levy R and Grun J B 1974 *Phys. Status Solidi A* **22** 11–38

[94] Shionoya S, Saito H, Hanamura E and Akimoto O 1973 *Solid State Commun.* **12** 223–226

[95] Hvam J M, Blattner G, Reuscher M and Klingshirn C 1983 *Phys. Status Solidi B* **118** 179–189

[96] Bohnert K, Schmieder G, El-Dessouki S and Klingshirn C 1978 *Solid State Commun.* **27** 295–299

[97] Binet F, Duboz J Y, Off J and Scholz F 1999 *Phys. Rev. B* **60** 4715–4722

[98] Koch S W, Haug H, Schmieder G, Bohnert W and Klingshirn C 1978 *Phys. Status Solidi B* **89** 431–440

[99] Othonos A 1998 *J. Appl. Phys.* **83** 1789–1830

[100] Chow W W and Koch S W 2013 *Semiconductor-laser fundamentals: physics of the gain materials* (Springer Science & Business Media)

[101] Bohnert K, Schmieder G and Klingshirn C 1980 *Phys. Status Solidi B* **98** 175–188

[102] Dingle R 1971 *Appl. Phys. Lett.* **19** 5

[103] Richters J P, Kalden J, Gnauck M, Ronning C, Dietrich C P, von Wenckstern H, Grundmann M, Gutowski J and Voss T 2012 *Semicond. Sc. Technol.* **27** 015005

[104] Coldren L, Corzine S and Mashanovitch M 2012 *Diode lasers and photonic integrated circuits* (Wiley)

[105] Casperson L 1975 *J. Appl. Phys.* **46** 5194–5201

[106] Hecht E 2001 *3. Auflage: Optik* (München: Oldenbourg Wissenschaftsverlag GmbH)

[107] Born M and Wolf E 1999 *Principles of Optics, 7th ed* (Cambridge University)

[108] Pan A, Liu D, Liu R, Wang F, Zhu X and Zou B 2005 *Small* **1** 980–983

[109] van Vugt L, Zhang B, Piccione B, Spector A and Agarwal R 2009 *Nano Lett.* **9** 1684–1688

[110] Gradecak S, Qian F, Li Y, Park H G and Lieber C M 2005 *Appl. Phys. Lett.* **87** 173111

[111] Nobis T, Kaidashev E, Rahm A, Lorenz M and Grundmann M 2004 *Phys. Rev. Lett.* **93** 103903

[112] Czekalla C, Nobis T, Rahm A, Cao B, Zuniga-Perez J, Sturm C, Schmidt-Grund R, Lorenz M and Grundmann M 2010 *Phys. Status Solidi B* **247** 1282–1293

[113] Zimmler M 2009 *Physics and applications of semiconductor nanowire photonic devices* (Harvard University)

[114] Maslov A and Ning C 2003 *Appl. Phys. Lett.* **83** 1237

[115] Zimmler M, Capasso F, Müller S and Ronning C 2010 *Semicond. Sc. Technol.* **25** 024001

[116] Ma Y, Guo X, Wu X, Dai L and Tong L 2013 *Adv. Opt. Photonics* **5** 216–273

[117] Maier S A 2007 *Plasmonics: fundamentals and applications* (Springer Science & Business Media)

[118] Sidiropoulos T P H 2015 *Enhanced light-matter interactions in laser systems incorporating metal-based optical confinement* Ph.D. thesis Imperial College London

[119] Rakic A D, Djurisic A B, Elazar J M and Majewski M L 1998 *Appl. Opt.* **37** 5271

[120] Brendel R and Bormann D 1992 *J. Appl. Phys.* **71** 1

[121] Oulton R F 2012 *Mater. Today* **15** 26–34

[122] Oulton R F, Sorger V J, Genov D A, Pile D F P and Zhang X 2008 *Nat. Photon.* **2** 496–500

[123] Lu Y, Kim J, Chen H, Wu C, Dabidian N, Sanders C, Wang C, Lu M, Li B, Qiu X *et al.* 2012 *Science* **337** 450–453

[124] Ho J, Tatebayashi J, Sergent S, Fong C F, Iwamoto S and Arakawa Y 2015 *ACS Photonics* **2** 165–171

[125] Purcell E M 1946 *Phys. Rev.* **69** 681

[126] Faraon A, Santori C, Huang Z, Acosta V M and Beausoleil R G 2012 *Phys. Rev. Lett.* **109** 033604

[127] McCutcheon M W and Loncar M 2008 *Opt. Express* **16** 19136

[128] Sorger V J, Pholchai N, Cubukcu E, Oulton R F, Kolchin P, Borschel C, Gnauck M, Ronning C and Zhang X 2011 *Nano Lett.* **11** 4907–4911

[129] Khajavikhan M, Simic A, Katz M, Lee J H, Slutsky B, Mizrahi A, Lomakin V and Fainman Y 2012 *Nature* **482** 204–207

[130] Wagner R S and Ellis W C 1964 *Appl. Phys. Lett.* **4** 89

[131] Hsu C L, Chang S J, Lin Y R, Li P C, Lin T S, Tsai S Y, Lu T H and Chen I C 2005 *Chem. Phys. Lett.* **416** 75–78

[132] Tessarek C, Bashouti M, Heilmann M, Dieker C, Knoke I, Spiecker E and Christiansen S 2013 *J. Appl. Phys.* **114** 144304

[133] Tessarek C, Röder R, Michalsky T, Geburt S, Franke H, Schmidt-Grund R, Heilmann M, Hoffmann B, Ronning C, Grundmann M and Christiansen S 2014 *ACS Photonics* **1** 990–997

[134] Borchers C, Müller S, Stichtenoth D, Schwen D and Ronning C 2006 *J. Phys. Chem. B* **110** 1656–1660

[135] Mandl B, Stangl J, Hilner E, Zakharov A A, Hillerich K, Dey A W, Samuelson L, Bauer G, Deppert K and Mikkelsen A 2010 *Nano Lett.* **10** 4443–4449

[136] Geng C, Jiang Y, Yao Y, Meng X, Zapien J A, Lee C S, Lifshitz Y and Lee S T 2004 *Adv. Funct. Mater.* **14** 589–594

[137] Geburt S 2012 *Lasing and ion beam doping of semiconductor nanowires* Ph.D. thesis University Jena

[138] Ogrisek M 2013 *Kontrolliertes Wachstum von Zinkoxid und Vanadium(IV)-oxid Nanodrähten* Master's thesis Friedrich Schiller University Jena

[139] Reimer L and Hawkes P 1998 *Scanning Electron Microscopy: Physics of Image Formation and Microanalysis* Springer Series in Optical Sciences (Springer)

[140] Egerton R F 2005 *Physical Principles of Electron Microscopy* (Springer Science + Business Media)

[141] Pecharsky V K and Zavalij P Y 2009 *Fundamentals of powder diffraction and structural characterization of materials* vol 69 (Springer)

[142] Yacobi B G and Holt D B 1990 *Cathodoluminescence microscopy of inorganic solids* (Springer Science & Business Media)

[143] Yacobi B G and Holt D B 1986 *J. Appl. Phys.* **59** R1

[144] Lakowicz J R 2006 *Principles of fluorescence spectroscopy* (Springer Science & Business Media)

[145] Schaefer B, Collett E, Smyth R, Barrett D and Fraher B 2007 *Am. J. Phys.* **75** 163–168

[146] Versteegh M, Vanmaekelbergh D and Dijkhuis J 2012 *Phys. Rev. Lett.* **108** 157402

[147] Shih T, Mazur E, Richters J P, Gutowski J and Voss T 2011 *J. Appl. Phys.* **109** 043504

[148] Pan A, Liu R, Yang Q, Zhu Y, Yang G, Zou B and Chen K 2005 *J. Phys. Chem. B* **109** 24268–24272

[149] Ma R M, Oulton R F, Sorger V J, Bartal G and Zhang X 2011 *Nat. Mater.* **10** 110–113

[150] Buschlinger R, Lorke M and Peschel U 2015 *Phys. Rev. B* **91** 045203

[151] Panchuk O, Savitskiy A, Fochuk P, Nykonyuk Y, Parfenyuk O, Shcherbak L, Ilashchuk M, Yatsunyk L and Feychuk P 1999 *J. Cryst. Growth* **197** 607–611

[152] Dean J A 1985 *Lange's handbook of chemistry* (McGraw Hill Book Co., New York, NY)

[153] Henry C H, Faulkner R A and Nassau K 1969 *Phys. Rev.* **183** 798–806

[154] Varshni Y 1967 *Physica* **34** 149–154

[155] Dhese K A, Devine P, Ashenford D E, Nicholls J E, Scott C G, Sands D and Lunn B 1994 *J. Appl. Phys.* **76** 5423–5428

[156] Zhao Q X, Willander M, Morjan R E, Hu Q H and Campbell E E B 2003 *Appl. Phys. Lett.* **83** 165–167

[157] Tran T K, Park W, Tong W, Kyi M M, Wagner B K and Summers C J 1997 *J. Appl. Phys.* **81** 2803–2809

[158] Thomas D G, Hopfield J J and Augustyniak W M 1965 *Phys. Rev.* **140** A202–A220

[159] Teke A, Özgür Ü, Dogan S, Gu X, Morkoc H, Nemeth B, Nause J and Everitt H O 2004 *Phys. Rev. B* **70** 195207

[160] Zhang X H, Chua S J, Yong A M, Yang H Y, Lau S P, Yu S F, Sun X W, Miao L, Tanemura M and Tanemura S 2007 *Appl. Phys. Lett.* **90** 013107

[161] Bäume P, Strauf S, Gutowski J, Behringer M and Hommel D 1998 *J. Cryst. Growth* **184-185** 531–535

[162] Stölzel M 2013 *Photolumineszenz von Exzitonen in polaren ZnO/MgZnO-Quantengrabenstrukturen* Ph.D. thesis University of Leipzig

[163] Sze S M and Ng K K 2006 *Physics of semiconductor devices* (John wiley & sons)

[164] Cai J, Jie J, Jiang P, Wu D, Xie C, Wu C, Wang Z, Yu Y, Wang L, Zhang X and et al 2011 *Phys. Chem. Chem. Phys.* **13** 14663

[165] Jiang D S, Jung H and Ploog K 1988 *J. Appl. Phys.* **64** 1371

[166] Hauser M, Hepting A, Hauschild R, Zhou H, Fallert J, Kalt H and Klingshirn C 2008 *Appl. Phys. Lett.* **92** 211105

[167] Faist J, Capasso F, Sivco D L, Hutchinson A L, Sirtori C, Chu S N G and Cho A Y 1994 *Appl. Phys. Lett.* **65** 2901

[168] Tatebayashi J, Kako S, Ho J, Ota Y, Iwamoto S and Arakawa Y 2015 *Nat. Photon.* **9** 501–505

[169] Fallert J, Dietz R J B, Zhou H, Sartor J, Klingshirn C and Kalt H 2009 *Phys. Status Solidi C* **6** 449–452

[170] Wille M, Sturm C, Michalsky T, Röder R, Ronning C, Schmidt-Grund R and Grundmann M 2016 *Nanotechnology* **27** 225702

[171] Mayer B, Janker L, Rudolph D, Loitsch B, Kostenbader T, Abstreiter G, Koblmüller G and Finley J J 2016 *Appl. Phys. Lett.* **108** 071107

[172] Haug H and Koch S 1977 *Phys. Status Solidi B* **82** 531–543

[173] Agarwal R, Barrelet C and Lieber C 2005 *Nano lett.* **5** 917–920

[174] Schwiderke M 2015 *Anregungs- und temperaturabhängige Lasingeigenschaften von Halbleiternanodrähten* Master's thesis Friedrich Schiller University Jena

[175] Ninomiya S and Adachi S 1995 *J. App. Phys.* **78** 1183

[176] Wiesner P and Heim U 1975 *Phys. Rev. B* **11** 3071–077

[177] Majumder F A, Swoboda H E, Kempf K and Klingshirn C 1985 *Phys. Rev. B* **32** 2407–2418

[178] Schwab H, Dörnfeld C, Göbel E O, Hvam J M, Klingshirn C, Kuhl J, Lyssenko V G, Majumder F A, Noll G, Nunnenkamp J and et al 1992 *Phys. Status Solidi B* **172** 479–519

[179] Saito H and Göbel E O 1985 *Phys. Rev. B* **31** 2360–2369

[180] Arakawa Y 1982 *Appl. Phys. Lett.* **40** 939

[181] Stockman M 2014 *Nat. Phys.* **10** 799–800

[182] Anker J N, Hall W P, Lyandres O, Shah N C, Zhao J and Van Duyne R P 2008 *Nat. Mater.* **7** 442–453

[183] Versteegh M A M, Kuis T, Stoof H T C and Dijkhuis J I 2011 *Phys. Rev. B* **84** 035207

[184] Xu H, Wright J B, Hurtado A, Li Q, Luk T S, Figiel J J, Cross K, Balakrishnan G, Lester L F, Brener I and Wang G T 2012 *Appl. Phys. Lett.* **101** 221114

[185] Yang C Y, Chia C T, Chen H Y, Gwo S and Lin K H 2014 *Appl. Phys. Lett.* **105** 212105

[186] Shah J 2012 *Hot carriers in semiconductor nanostructures: Physics and applications* (Elsevier)

[187] Pugnet M, Collet J and Cornet A 1981 *Solid State Commun.* **38** 531–536

[188] Ye H, Wicks G W and Fauchet P M 1999 *Appl. Phys. Lett.* **74** 711–713

[189] Zhang X B, Taliercio T, Kolliakos S and Lefebvre P 2001 *J. Phys.: Condens. Matter* **13** 7053

[190] Shah J 1978 *Solid State Electron.* **21** 43 – 50

[191] Zukauskas A, Tamulaitis G, Gaska R, Shur M, Khan M and Yang J 1999 *Phys. Status Solidi B* **216** 495–499

[192] Prabhu S S and Vengurlekar A S 2004 *J. Appl. Phys.* **95** 7803–7812

[193] Fröhlich H 1954 *Adv. Phys.* **3** 325–361

[194] Yang X, Xu C and Giles N C 2008 *J. Appl. Phys.* **104** 073727

[195] Mayer B, Regler A, Sterzl S, Stettner T, Koblmüller G, Kaniber M, Lingnau B, Lüdge K and Finley J 2016 *arXiv preprint arXiv:1603.02169*

[196] Chernikov A, Bornwasser V, Koch M, Chatterjee S, Böttge C N, Feldtmann T, Kira M, Koch S W, Wassner T, Lautenschläger S, Meyer B K and Eickhoff M 2012 *Phys. Rev. B* **85** 035201

[197] Oguzman I H, Kolnik J, Brennan K F, Wang R, Fang T N and Ruden P P 1996 *J. Appl. Phys.* **80** 4429–4436

[198] Kolnik J, Oguzman I H, Brennan K F, Wang R, Ruden P P and Wang Y 1995 *J. Appl. Phys.* **78** 1033–1038

[199] Stockman M I 2010 *J. Opt.* **12** 024004

[200] Ma R M, Oulton R F, Sorger V J and Zhang X 2012 *Laser Photon. Rev.* **7** 1–21

[201] Wuestner S, Hamm J M, Pusch A and Hess O 2015 *Laser Photon. Rev.* **9** 256–262

[202] Palik E D 1997 *Handbook of optical constants of solids* (Elsevier)

[203] Sun C K, Sun S Z, Lin K H, Zhang K Y J, Liu H L, Liu S C and Wu J J 2005 *Appl. Phys. Lett.* **87** 023106

[204] Klingshirn C, Fallert J, Gogolin O, Wissinger M, Hauschild R, Hauser M, Kalt H and Zhou H 2008 *J. Lumin.* **128** 792–796

[205] Fontana Y, Grzela G, Bakkers E P A M and Rivas J G 2012 *Phys. Rev. B* **86** 245303

[206] van Dam D, Abujetas D R, Paniagua-Dominguez R, Sanchez-Gil J A, Bakkers E P A M, Haverkort J E M and Gomez Rivas J 2015 *Nano Lett.* **15** 4557–4563

[207] Saxena D, Wang F, Gao Q, Mokkapati S, Tan H H and Jagadish C 2015 *Nano Lett.* **15** 5342–5348

[208] Sun L, Ren M L, Liu W and Agarwal R 2014 *Nano Lett.* **14** 6564–6571

[209] Valle A, Sarma J and Shore K 1995 *IEEE J. Quant. Electron.* **31** 1423–1431

[210] Buccafusca O, Chilla J L A, Rocca J J, Feld S, Wilmsen C, Morozov V and Leibenguth R 1996 *Appl. Phys. Lett.* **68** 590–592

[211] Claudon J, Bleuse J, Malik N S, Bazin M, Jaffrennou P, Gregersen N, Sauvan C, Lalanne P and Gerard J M 2010 *Nat. Photon.* **4** 174–177

[212] Yang P, Yan H, Mao S, Russo R, Johnson J, Saykally R, Morris N, Pham J, He R and Choi H J 2002 *Adv. Funct. Mater.* **12** 323–331

[213] Röder R, Ploss D, Kriesch A, Buschlinger R, Geburt S, Peschel U and Ronning C 2015 *J. Phys. D: Appl. Phys.* **48** 239501

[214] Geburt S, Röder R, Kaiser U, Chen L, Chu M H, Segura-Ruiz J, Martinez-Criado G, Heimbrodt W and Ronning C 2013 *Phys. Status Solidi RRL* **7** 886–889

[215] Michalsky T, Wille M, Dietrich C P, Röder R, Ronning C, Schmidt-Grund R and Grundmann M 2014 *Appl. Phys. Lett.* **105** 211106

[216] Liu C, Röder R, Zhang L, Ren Z, Chen H, Zhang Z, Ronning C and Gao P X 2014 *J. Mater. Chem. A* **2** 4157

[217] Reimer T, Paulowicz I, Röder R, Kaps S, Lupan O, Chemnitz S, Benecke W, Ronning C, Adelung R and Mishra Y K 2014 *ACS Appl. Mater. Interfaces* **6** 7806–7815

[218] Schmerbauch C, Gonzalez-Julian J, Röder R, Ronning C and Guillon O 2014 *J. Am. Ceram. Soc.* **97** 1728–1735

[219] Cammi D, Röder R and Ronning C 2014 *J. Phys. D: Appl. Phys.* **47** 394014

[220] Geburt S, Lorke M, da Rosa A L, Frauenheim T, Röder R, Voss T, Kaiser U, Heimbrodt W and Ronning C 2014 *Nano Lett.* **14** 4523–4528

[221] Huang L, Lin C C, Riediger M, Röder R, Tse P L, Ronning C and Lu J G 2015 *Nano Lett.* **15** 974–980

[222] Dargatz B, Gonzalez-Julian J, Bram M, Jakes P, Besmehn A, Schade L, Röder R, Ronning C and Guillon O 2016 *J. Eur. Ceram. Soc.* **36** 1207–1220

A List of Publications

Publications directly related to this thesis

1. Geburt S, Thielmann A, Röder R, Borschel C, McDonnell A, Kozlik M, Kühnel J, Sunter K A, Capasso F and Ronning C 2012 *Nanotechnology* **23** 365204

2. Röder R, Wille M, Geburt S, Rensberg J, Zhang M, Lu J G, Capasso F, Buschlinger R, Peschel U and Ronning C 2013 *Nano Lett.* **13** 3602–3606

3. Zhang M, Wille M, Röder R, Heedt S, Huang L, Zhu Z, Geburt S, Grützmacher D, Schäpers T, Ronning C and Lu J G 2014 *Nano Lett.* **14** 518–523

4. Röder R, Ploss D, Kriesch A, Buschlinger R, Geburt S, Peschel U and Ronning C 2014 *J. Phys. D: Appl. Phys.* **47** 394012

5. Röder R, Ploss D, Kriesch A, Buschlinger R, Geburt S, Peschel U and Ronning C 2015 *J. Phys. D: Appl. Phys.* **48** 239501

6. Tessarek C, Röder R, Michalsky T, Geburt S, Franke H, Schmidt-Grund R, Heilmann M, Hoffmann B, Ronning C, Grundmann M and Christiansen S 2014 *ACS Photonics* **1** 990–997

7. Sidiropoulos T P H, Röder R, Geburt S, Hess O, Maier S A, Ronning C and Oulton R F 2014 *Nat. Phys.* **10** 870–876

8. Röder R, Sidiropoulos T P H, Tessarek C, Christiansen S, Oulton R F and Ronning C 2015 *Nano Lett.* **15** 4637–4643

9. Röder R, Sidiropoulos T P H, Buschlinger R, Riediger M, Peschel U, Oulton R F and Ronning C 2016 *Nano Lett.* **16** 2878–2884

10. Wille M, Sturm C, Michalsky T, Röder R, Ronning C, Schmidt-Grund R and Grundmann M 2016 *Nanotechnology* **27** 225702

Further publications

1. Geburt S, Röder R, Kaiser U, Chen L, Chu M H, Segura-Ruiz J, Martinez-Criado G, Heimbrodt W and Ronning C 2013 *Phys. Status Solidi RRL* **7** 886–889

2. Michalsky T, Wille M, Dietrich C P, Röder R, Ronning C, Schmidt-Grund R and Grundmann M 2014 *Appl. Phys. Lett.* **105** 211106

3. Liu C, Röder R, Zhang L, Ren Z, Chen H, Zhang Z, Ronning C and Gao P X 2014 *J. Mater. Chem. A* **2** 4157

4. Reimer T, Paulowicz I, Röder R, Kaps S, Lupan O, Chemnitz S, Benecke W, Ronning C, Adelung R and Mishra Y K 2014 *ACS Appl. Mater. Interfaces* **6** 7806–7815

5. Schmerbauch C, Gonzalez-Julian J, Röder R, Ronning C and Guillon O 2014 *J. Am. Ceram. Soc.* **97** 1728–1735

6. Cammi D, Röder R and Ronning C 2014 *J. Phys. D: Appl. Phys.* **47** 394014

7. Geburt S, Lorke M, da Rosa A L, Frauenheim T, Röder R, Voss T, Kaiser U, Heimbrodt W and Ronning C 2014 *Nano Lett.* **14** 4523–4528

8. Huang L, Lin C C, Riediger M, Röder R, Tse P L, Ronning C and Lu J G 2015 *Nano Lett.* **15** 974–980

9. Dargatz B, Gonzalez-Julian J, Bram M, Jakes P, Besmehn A, Schade L, Röder R, Ronning C and Guillon O 2016 *J. Eur. Ceram. Soc.* **36** 1207–1220

B List of oral and poster presentations

1. Talk: *Polarization dependent CdS nanowire lasing*
   DPG Spring Meeting, Regensburg 2013

2. Poster: *Tailoring CdS nanowire lasing resonators*
   DPG Spring Meeting, Regensburg 2013

3. Talk: *Semiconductor nanowire photonics*
   International Max Planck Research School Physics of Light, Erlangen 2013

4. Poster: *Tailoring CdS photonic nanowire lasers*
   TUM Nanowire Workshop, München 2013

5. Talk: *Continuous wave green nanowire laser*
   MRS Fall Meeting, Boston 2013

6. Talk: *Semiconductor nanowire photonics*
   Laboratory for Nanoscale Optics - Loncar Lab, SEAS Harvard University, Cambridge 2014

7. Talk: *Investigation of CdS nanowire lasing emission*
   SPIE Optics + Photonics, San Diego 2014

8. Talk: *Temporal dynamics of nanowire based lasers*
   MRS Fall Meeting, Boston 2014

9. Poster: *Investigation of semiconductor nanowire lasing emission*
   MRS Fall Meeting, Boston 2014

10. Poster: *Ultrafast dynamics of lasing semiconductor nanowires*
    Nanowires Workshop, Barcelona 2015

11. Talk: *Mode switching in ZnO nanowire lasers*
    MRS Fall Meeting, Boston 2015

12. Poster: *Ultrafast dynamics of semiconductor nanowire lasers*
    MRS Fall Meeting, Boston 2015

C Curriculum Vitae

Persönliche Daten

Name	Robert Röder
Geburtsdatum	03.10.1986
Geburtsort	Zeitz

Ausbildung und wissenschaftlicher Werdegang

1993 - 1997	5. Grundschule in Zeitz
1997 - 1999	1. Sekundarschule in Zeitz
1999 - 2006	Geschwister-Scholl-Gymnasium Zeitz
Juni 2006	Abitur
2006 - 2007	Zivildienst im Klinikum Zeitz
2007 - 2010	Bachelorstudium Physik an der Friedrich-Schiller-Universität Jena
Sept. 2010	B.Sc. in Physik
2010 - 2012	Masterstudium Physik an der Friedrich-Schiller-Universität Jena
Okt. 2012	M.Sc. in Physik
2012 - 2016	Wissenschaftlicher Mitarbeiter an der Friedrich-Schiller-Universität Jena, AG Ronning

Jena, den 01.06.2016

(Robert Röder)

D Ehrenwörtliche Erklärung

Ich erkläre hiermit ehrenwörtlich, dass ich die vorliegende Arbeit selbständig, ohne unzulässige Hilfe Dritter und ohne Benutzung anderer als der angegebenen Hilfsmittel und Literatur angefertigt habe. Die aus anderen Quellen direkt oder indirekt übernommenen Daten und Konzepte sind unter Angabe der Quelle gekennzeichnet.

Bei der Auswahl und Auswertung folgenden Materials haben mir die nachstehend aufgeführten Personen in der jeweils beschriebenen Weise entgeltlich/unentgeltlich geholfen:

- Die Synthese der undotierten CdS Nanodrähte wurde zum Teil von Marcel Wille durchgeführt.
- Die CdS:Sn Nanostrukturen wurden von Mengyao Zhang in der Gruppe von Prof. Jia Grace Lu an der University of Southern California synthetisiert.
- ZnO Nanodrähte wurden zum Teil von Matthias Ogrisek, Max Riediger, Lukas Trefflich und Dr. Davide Cammi hergestellt.
- Die Herstellung der GaN Nanodrähte mittels MOVPE wurde von Dr. Christian Tessarek in der Gruppe von Silke Christiansen am MPI für die Physik des Lichts in Erlangen durchgeführt.
- Die SEM, SEM-EDX, TEM und XRD Untersuchungen an den CdS:Sn Nanostrukturen wurden wiederum von Mitgliedern der Gruppe von Prof. Jia Grace Lu durchgeführt.
- Die Kathodolumineszenz-Spektroskopie wurde teilweise von Dr. Sebastian Geburt durchgeführt.
- Die Makro- und Mikrophotolumineszenzmessungen an CdS:Sn Nanodrähten sowie die Experimente zum cw-Lasing wurden gemeinsam mit Marcel Wille durchgeführt. Die zeitaufgelösten Photolumineszenzmessungen wurden von Marcel Wille in der Gruppe von Prof. Marius Grundmann an der Universität Leipzig durchgeführt.
- Die Simulation der Ladungsträgerdichten in hochangeregten CdS Nanodrähten wurde in Zusammenarbeit mit Jura Rensberg entwickelt und implementiert.
- Die Messungen zur Laserdynamik von Nanodrähten mittels der Doppel-Pump-Technik wurden in Zusammenarbeit mit Dr. Themistoklis Sidiropoulos und Dr. Rupert Oulton am Imperial College in London durchgeführt und gemeinsam interpretiert. Die Silber-Substrate für die plasmonischen Nanodraht-Laser wurden ebenso von Dr. Themistoklis Sidiropoulos hergestellt.
- Die Simulation der Dispersionsrelationen in Kapitel 5 und des Intensitätsverlaufs unter Doppel-Pump-Anregung wurden von Dr. Themistoklis Sidiropoulos und Dr. Rupert Oulton durchgeführt und gemeinsam optimiert.
- Der Aufbau und die Erweiterung des Head-on-Setups erfolgte in Zusammenarbeit mit Daniel Ploss und Arian Kriesch in der Gruppe von Prof. Ulf Peschel an der Universität Erlangen. Die Messungen wurden gemeinsam mit Max Riediger durchgeführt.

- Die optischen Simulationen von Nanodrahtlasern (statisch und dynamisch) wurden von Robert Buschlinger in der Gruppe von Prof. Ulf Peschel an der Universität Jena durchgeführt. Die Absorption von Licht in CdS Nanodrähten wurde ebenso von Robert Buschlinger simuliert.

- Im Übrigen waren jeweils die Koautoren der angeführten Veröffentlichungen (s. Anhang List of Publications) an der Interpretation der Ergebnisse beteiligt.

Weitere Personen waren an der inhaltlich-materiellen Erstellung der vorliegenden Arbeit nicht beteiligt. Insbesondere habe ich hierfür nicht die entgeltliche Hilfe von Vermittlungs- bzw. Beratungsdiensten (Promotionsberater oder andere Personen) in Anspruch genommen. Niemand hat von mir unmittelbar oder mittelbar geldwerte Leistungen für die Arbeiten erhalten, die im Zusammenhang mit dem Inhalt der vorgelegten Dissertation stehen.
Die Arbeit wurde bisher weder im In- noch im Ausland in gleicher oder ähnlicher Form einer anderen Prüfungsbehörde vorgelegt. Die geltende Prüfungsordnung der Physikalisch-Astronomischen Fakultät ist mir bekannt.
Ich versichere ehrenwörtlich, dass ich nach bestem Wissen die reine Wahrheit gesagt und nichts verschwiegen habe.

Jena, den 01.06.2016

(Robert Röder)

Danksagung

Die nächsten Zeilen möchte ich darauf verwenden mich bei allen zu bedanken, die mich in den letzten Jahren (und v.a. während der Promotionsphase) wissenschatlich, experimentell, technisch und auch moralisch/emotional unterstützt haben. Meine letzten Jahre waren dabei natürlich sehr durch die Zeit im 'Roten Haus' und von allen 'Insassen' darin geprägt. Einen großen Dank möchte ich natürlich zuerst Carsten Ronning, dem 'Kopf' des Roten Hauses, aussprechen. Du hast mir vor etwa viereinhalb Jahren die Möglichkeit gegeben in deiner Arbeitsgruppe meine Masterarbeit anzufertigen. Seitdem hast du meinen wissenschaftlichen Werdegang stark beeinflusst. Schon damals hatte ich Dank der Arbeitsweise in deiner Gruppe viele Möglichkeiten die thematische und experimentelle Ausrichtung meiner Masterarbeit mitzugestalten und auch schon früh Experimente und Ideen in Kollaborationen zu verfolgen/dikutieren. Obwohl ich nur ein 'kleiner' Student (das ist hier nicht nur sprichwörtlich gemeint) war, habe ich den Vertrauensvorsprung und die damit verbundene Eigenständigkeit und Eigenverantwortung sehr zu schätzen gewusst. Demzufolge war es für mich eine konsequente und einfache Entscheidung nach der Masterarbeit für weitere $3-4$ Jahre in diesem Arbeitsumfeld zu bleiben und eine Promotion anzuschließen. Darüber hinaus bist du ein 'cooler' Chef, da du neben dem netten, offenen wissenschaftlichen Austausch auch privat sehr umgänglich und zugänglich bist.
Als ich die Promotion dann begann, trat ich (so etwas wie) die expermentelle und thematische Nachfolge von Sebastian Geburt an. Sebastian, dir gebührt ebenso ein großer Dank. Als Neu-Doktorand war es sehr angenehm ein Vorbild bzw. eine Richtmarke zu haben, an der ich meine Arbeitsweise ausrichten konnte. Dadurch hast du mich auch über die Masterarbeit hinaus geprägt, während der du mich betreut hast.
Die Arbeitsweise und den wissenschaftlichen Austausch in der Arbeitsgruppe und im gesamten roten Haus habe ich immer als sehr kollegial, unterstützend, kontruktiv und inspirierend empfunden und dadurch sehr genossen. Diese Arbeitsweise hat sich auch übertragen in die vielen Kollaborationen, an denen ich während der letzten Jahre teilnehmen durfte. At this point I'd like to thank Dr. Rupert Oulton and Dr. Themistoklis Sidiropoulos for the nice, exciting and fruitful collaboration over the last years. I enjoyed every of my research stays in London with you. You always hosted me well. I also thank you for the valuable discussions and your trust in our expertise/interpretation. This thesis would have to be very different without you and our collaboration. Thank you very much.
I also thank Prof. Jia Grace Lu and her team from the USC in Los Angeles. Liebe Grace, vielen Dank für die Bereitstellung der tollen Nanodrahtproben und die Möglichkeit daran zu forschen. Ich habe mich auch immer gefreut, wenn du uns in Jena besucht hast und wenn ich Weihnachten eine 'Christmas-Email' von dir auf deutsch erhalten habe. Ein großer Dank gilt auch Robert Buschlinger und Prof. Ulf Peschel. Eure Unterstützung von theoretischer Seite hat uns/mir oft geholfen, die experimentellen Ergebnisse einordnen und verstehen zu können. Daher freut es mich sehr, dass mich die Zusammenarbeit mit euch die ganze Promotion hinweg begleitet hat. Unsere Diskussionen waren immer sehr offen und aufschlussreich, so dass immer neue Ideen entstanden sind. Zu diesen Ideen gehörte auch der 'Head-on'-Aufbau, bei dessen Verwirklichung mich Daniel und Arian stark unterstützt haben. Vielen Dank.
Neben den Kollaborationen, deren Ergebnisse Eingang in diese Arbeit gefunden haben, gab es viele weitere Gruppen/Leute, bei denen ich mich bedanken möchte für die tolle

Zusammenarbeit. Dazu gehören v.a. die Mitgleider der Forschergruppe FOR1616. Ein großer Dank gebührt Tom, Sebastian, Frank, Christian (Danke for die GaN NWs), Jana, Claudia, Linus, Angelina, Martin und Michael.
Weiterhin will ich denen danken, deren Abschlussarbeiten ich betreuen durfte und die mir als gute Experimentatoren und Kollegen zur Seite standen. Lisa und Lukas möchte ich danken, dass ihr es euch irgendwie zugemutet habt bei mir die Masterarbeit anzufertigen. Wenn die wissenschaftliche Aufgaben/Fragestellung manchmal auch recht schwierig war, habt ihr doch meist im Stillen gelitten und wirklich tolle Arbeit geleistet. Auch wenn ihr es nicht "länger ertragen konntet" in unserer Arbeitsgruppe zu arbeiten, wünsche ich euch viel Glück. Ein großer Dank gilt Marcel Wille, der sich geopfert hat mein erster Masterand zu sein. Du hast eine super Arbeit geleistet. Daher freut es mich besonders, dass viele Ergebnisse in dieser Arbeit 'stecken', die wir zusammen erzielt haben. Es ist immer ein Vergnügen, wenn wir seitdem wieder intensiv zusammen arbeiten konnten. Ein großer Dank gilt auch Max Riediger. Deine stetige, konzentrierte und unaufgeregte (das ist positiv gemeint) Arbeitsweise war sehr wichtig für das Gelingen deiner Experimente, die ebenso in dieser Arbeit 'gelandet' sind. 'Last but not least', die drei armen Kerle, die noch aktuell mit mir zusammen arbeiten müssen. Ich danke euch Torsten, Walter und Max dafür, dass ihr mich durch eure tolle Arbeit, eure Fragen und Anregungen unterstützt. Darüber hinaus zeigt sich durch die Arbeit mit euch, dass auch nach so ein paar Jahren immer wieder neue Blickwinkel, Ideen und Inspirationen entstehen.
Weiterhin möchte ich denen danken, die Proben für die Experimente dieser Arbeit hergestellt haben und die noch nicht erwähnt wurden: Matthias, Davide, vielen Dank.
Ein Dankeschön möchte ich auch den Werkstattmitarbeitern aussprechen für die oftmals schnelle und unkomplizierte Arbeitsweise und Fabrikation von Bauteilen, Probenhalten jeglicher Art usw. Ich möchte auch den Technikern im roten Haus danken (Carmen, Patrick, Frank und Ulli) dafür, dass ihr immer versucht es mit unseren 'verrückten' Wünschen und Fragestellungen aufzunehmen.
Darüber hinaus danke ich den Kollegen (aktuelle und ehemalige) und 'Insassen' im roten Haus, die noch nicht genannt werden konnten. Ich danke besonders Raphael, Christian, Jana, Udo, Martin, Steffen, Davide, Christoph (heiß, heißer, Heisler), Jura, Sven, Philipp, Claudia. Es war immer toll mit euch zu arbeiten und Zeit zu verbringen, z.b. bei der Frühstücksrunde. Einen großen Dank möchte ich auch Anja aussprechen, da sie mir mir oft bei so manchen organisatorischen Fragen geholfen hat.
Die meiste Zeit verbringt man während der Promotion nicht (wie viel denken mögen) im Labor sondern im Büro. An dieser Stelle möchte ich klarstellen, dass ihr liebe 'Büro-Homies' aus 203 dafür verantwortlich seid, dass so eine Promotion doch deutlich länger dauert, als man am Anfang denkt. Vielen Dank dafür! Ich verspührte und verspühre noch immer Skrupel, wenn eine Email von euch ankommt. Denn darin befindet sich garantiert ein Link zu Youtube, NineGag, Spiegelonline...., der mich leidvolle Minuten an das Internet fesselt und somit von der Arbeit abhält. Ich möchte euch danken, HHM, AJ und Yaser für die tolle Zeit in 203. Ich sehe es mit schwerem Herzen, dass sich das Büro langsam 'zersetzt'. Lieber Henry, ich bedaure, dass wir nicht länger das Büro teilen, wünsche dir aber v.a. alles Gute an der EAH. Darüber hinaus möchte ich gern Alex von Müller und Emanuel als Ehrenmitglieder für die Crew 203 nominieren und ebenfalls danken.
Glücklicherweise gibt es neben der Arbeit auch noch ein Privatleben. Ich möchte meinen Freunden danken. Ich genieße es, mit euch Zeit zu verbringen, denn ihr schafft es, dass ich die Arbeit komplett ausblenden kann und mich den (noch) angenehmeren Seiten des Lebens widme. Liebe '3G-ler', ich danke euch für die tollen letzten Jahre, alle Konzerte,

Ausflüge, Feste, Kinoabende ... und viele 'freudvolle Stunden am Fass'. Weiterhin möchte ich meinen Freunden aus der 'alten Heimat' danken. Auch wenn wir uns leider nicht so oft sehen, ist es bei jedem Treffen so vertraut, als ob wir uns täglich sehen. Ich danke auch meiner Freundin Fanny und meinem langjährigen Mitbewohner und gutem Freund Christian.
Der wohl größte Dank gebührt meinen Eltern. Liebe Mutti, lieber Vati, ich danke euch sehr dafür, dass ihr mich immer unterstützt habt in allen Etappen meines Lebens. Danke, dass ihr mir das Studium ermöglicht habt. Auch wenn meine "Ausbildung" manchmal schier unendlich wirkte, habt ihr mir euer Vertrauen geschenkt und euch immer für meine Arbeit interessiert. Ihr habt mich immer ermuntert meine eigenen Entscheidungen zu treffen und ich konnte sicher sein, dass ihr mich bei der Erfüllung meiner Wünsche und Ziele unterstützt. Vielen Dank euch beiden! Außerdem möchte ich meinen Großeltern danken, v.a. meiner Oma Anita. Danke, dass du immer stolz auf mich bist.